ANALYTICAL AND COMPUTATIONAL STUDY OF TURBULENT-HOT JET IGNITION PROCESS IN METHANE-HYDROGEN-AIR MIXTURES

by

Mohammad Ebrahim Feyz

A Dissertation

Submitted to the Faculty of Purdue University

In Partial Fulfillment of the Requirements for the degree of

Doctor of Philosophy

School of Mechanical Engineering

West Lafayette, Indiana

December 2019

THE PURDUE UNIVERSITY GRADUATE SCHOOL
STATEMENT OF COMMITTEE APPROVAL

Dr. M. Razi Nalim[1] and Dr. Jay P. Gore[2], Co-Chairs

[1]Purdue School of Engineering and Technology, Indianapolis

[2]School of Mechanical Engineering

Dr. Sally P. Bane

School of Aeronautics and Astronautics

Dr. Carlos Larriba-Andaluz

Purdue School of Engineering and Technology, Indianapolis

Approved by:

Dr. M. Razi Nalim

To my parents- Mansoureh and Nasser for their unconditional love and support

and

To the eager souls who always seek the Truth.

ACKNOWLEDGMENTS

Throughout my doctoral career, I had the privilege to meet many distinguished individuals who have left a significant impression on me.

First and foremost, my deepest gratitude goes to my advisor, Professor Razi Nalim, for his beautiful insights and mentorship. I owe my enthusiasm in research and scientific work to his wisdom, guidance, and expertise.

Furthermore, I would like to extend my utmost respect and appreciation to my co-advisor, Professor Jay Gore, who helped me to better understand combustion physics through his vast knowledge and intuition.

Very special thanks goes to my committee members, Professor Sally Bane and Professor Carlos Larriba-Andaluz for their incredible support, encouragement and valuable suggestions. I am also grateful for the inspiring support of my former and present colleagues and friends Ali Tarraf, Arshad Zahangir Chowdhury and Veeraraghava Raju Hasti during my academic endeavors.

I would like to acknowledge the financial support of National Science Foundation under Grant No. CBET-1235696 awarded to IUPUI, and the Purdue School of Engineering & Technology which made my research possible.

TABLE OF CONTENTS

LIST OF TABLES

LIST OF FIGURES

PREFACE

Pressure-gain combustion in wave rotors offer the opportunity for substantial improvement in gas turbine efficiency and power, while controlling emissions with fuel flexibility, if provided rapid and reliable ignition of lean mixtures. In addition, tightening emission regulations and increasing availability of gas fuels for internal-combustion engines require more reliable ignition for ultra-lean operation to avoid high peak combustion temperature. Turbulent jet ignition (TJI) is able to address the ignition challenges of lean premixed combustion. Especially, the turbulent hot jet results in faster ignition penetration for wave rotor pressure-gain combustors that have high-frequency operation and fast-burn requirements. Controllability of TJI needs better understanding of the chemistry and fluid mechanics in the jet mixing region, particularly the estimation of ignition delay time and identifying the location of the ignition onset.

In the present work, numerical and analytical methods are employed to develop models capable of estimating the ignition characteristics that the turbulent hot jet exhibits as it is issued to a cold stoichiometric CH_4-H_2-Air mixture with varied fuel reactivity blends. Numerical models of the starting turbulent jet are developed by Reynolds-averaged and large-eddy simulation of Navier-Stokes and scalar transport equations in a high-resolution computational domain, with major focus on ignition of high-reactivity fuel blends in the jet near-field due to computational resource limitations. The chemical reactions are modeled using detailed chemistry by well-stirred and partially stirred reactor approaches. Numerical models describe the temporal evolution of jet mixture fraction, scalar dissipation rate, flow strain rate, and thermochemical quantities of the flow.

For faster estimation of ignition characteristics, analytical methods are developed to explicitly solve governing equations for the transient evolution of the near field and the leading vortex of the starting hot jet. First, the transient radial evolution of the turbulent shear-layer of a round transient jet is analytically investigated in the near-field of the nozzle, where the momentum potential core exists. The methods approximate the mixing and chemical processes in the jet shear and mixing layer. The momentum equation is integrated analytically, with a mixing-length turbulence model to represent the variation of effective viscosity due to the velocity gradients. The analytic predictions of the velocity field and mass entrainment rate of the jet are compared with numerical predictions and experimental findings. In addition, the transport equation of conserved scalars in the jet near-field is solved analytically for the history of the jet mixture fraction. This analytic

solution for temperature and species is used, together with available models for instantaneous chemical induction time, to create an analytic ignition model that provides the time and radial location of the ignition onset.

Lastly, the ignition mechanism within the vortex ring, which leads the starting turbulent jet, is modeled using prior understanding about the mixing characteristics of the vortex. This mechanism is more relevant to low-reactivity fuel blends. Due to the presence of strong mixing at the large-scale, the vortex ring is treated as a homogeneous batch-reactor, which contains certain levels of the jet mixture fraction. This assumption provides the initial composition and temperature of the reactor in which ignition ensues.

This article-dissertation is developed as a collection of 4 articles published in peer-reviewed journals, one submitted article, and additional unpublished work. The study is laid out in 6 chapters with the following contributions:

Chapter 1: This chapter numerically investigates the three-dimensional behavior of a transient hot jet as modeled using the Reynolds-averaged turbulence flow [1]. The study aims at providing an insight towards the role of mixing in the ignition progress and how the operating conditions such as fuel mixture and pre-chamber pressure ratio can influence the ignition success. An ignition prediction criterion is developed in this chapter, which helps to predict the ignition success under a broad range of operating conditions.

Chapter 2: In this chapter, the large-eddy simulation (LES) of hot jet ignition is reported in conjunction with detailed kinetics mechanism and adaptive-mesh refinement [2]. The correlation between local values of mixture fraction gradient and ignition is discussed. Furthermore, the role of methane-hydrogen ratio on the heat release pattern is studied for two specific mixtures.

Chapter 3: The LES of CH_4-H_2-Air ignition is extended in this chapter to account for multivariable evaluation of ignition [3]. Joint probability assessment of ignition explains the role of important scalars on the formation and growth of ignition. Also, the effect of CH_4-H_2 ratio on the spatial distribution of ignition is assessed and discussed.

Chapter 4: In this chapter, the rate of mass entrainment into the jet in the near-field region is studied [4]. Characterization of the mass entrainment illuminates the understanding of mixing behavior of the starting turbulent jets. Through an exact solution of the momentum equation, this chapter includes a model of the diffusive transport in a round transient jet at high Reynolds numbers.

Chapter 5: This chapter proposes a method to evaluate the mass/heat exchange between a transient-turbulent jet and a quiescent environment. To analyze the transport phenomena in the jet near-field, the transient diffusion equation in cylindrical coordinates is explicitly solved and its solution is compared with the empirical findings. The transport solution then enables an ignition model to describe the spatiotemporal characteristics of ignition in the near-field.

Chapter 6: The development of ignition within the vortex ring of the transient jet is investigated in this chapter. The initiation, growth, and departure of the vortex ring are studied using the available empirical correlations and the LES. Using a perfectly-stirred, zero-dimensional representation of the vortex, chemical kinetic calculations provide estimates of ignition delay for various fuel mixtures.

1. THREE-DIMENSIONAL SIMULATION OF TURBULENT HOT-JET IGNITION FOR AIR-CH_4-H_2 DEFLAGRATION IN A CONFINED VOLUME

Acknowledgment: This is a post-peer-review, pre-copyedit version of an article published in Flow, Turbulence and Combustion. The final authenticated version is available online at: https://doi.org/10.1007/s10494-018-9893-7

1.1 Abstract

This work investigates the essential aspects of the ignition process initiated by the injection of a hot starting jet into a constant volume containing air-CH_4-H_2 mixture. Driven by the pressure difference between a pre-chamber and a long narrow constant-volume-combustion (CVC) chamber, the developing jet or puff involves complex processes of turbulent jet penetration and evolution of multi-scale vortices in the shear layer, jet tip, and adjacent confined spaces. The CVC chamber contains stoichiometric mixtures of air with gaseous fuel initially at atmospheric conditions. Fuel reactivity is varied using two different CH4/H2 blends. Jet momentum is varied using different pre-chamber pressures at jet initiation. The jet initiation and the subsequent ignition events generate pressure waves that interact with the mixing region and the propagating flame, depositing baroclinic vorticity. Transient three-dimensional flow simulations with detailed chemical kinetics are used to model CVC mixture ignition. Pre-ignition gas properties are then examined to develop and verify criteria to predict ignition delay time using lower-cost non-reacting flow simulations for this particular case of study.

Keywords: Hot jet ignition, Constant volume combustor, Pre-chamber ignition

1.2 Introduction

Deflagration initiation by injection of hot gas into a fuel-air mixture is important in combustion engines, explosion protection and fire safety. Turbulent hot-jet ignition can be a reliable means of rapid ignition of fuel-lean gas in stratified internal combustion engines and in wave-rotor combustors (WRC) with high effectiveness [2, 5]. Ignition by a turbulent jet was investigated in the 1950's by Noble-prize-winner Nikolai Semenov [6] and was further established by Gussak et al., [7] and Wolanski [8] for IC engine applications, emphasizing the role of radicals

from a chemical perspective. Jet hydrodynamics was studied by Oppenheim [6] and co-workers elaborating the factors by which jet penetration and dispersion could be controlled. The penetrative hot jet which normally contains chemically active radicals can act as a distributed source of ignition. The temporal and spatial evolution of the transient jet involves complex features as the walls interact acoustically and aerodynamically with the developing jet [9].

Prior work in relatively unconfined mixtures included attempts to correlate the jet characteristics such as temperature, momentum and orifice diameter to ignition success. The location of ignition by an inert, laminar hot jet was described by a simplistic plug flow reactor model backed by empirical data [10]. As expected, the ignition takes place closer to the nozzle as the jet temperature increases and farther away as the jet velocity increases. However, if turbulence enhances mixing, the effect of jet velocity on ignition may be more nuanced. Ignition success involves a competition and a collusion between chemical time scale and the mixing time scale of jet entrainment, diffusive transport, and mixing at smaller scales. The overall thermal-chemical balance determines whether the exothermic reactions prevail and ignition takes place. Imbalanced transport of heat and reactants may quench ignition. As the jet contains active radicals that are a product of a primary combustion in the pre-chamber, an appropriate model would consider this in achieving cost-effective predictions of ignition.

The critical minimum radius for the jet (under which ignition is suppressed) is evaluated and prescribed to be necessarily larger than the deflagration thickness of the flame [11]. Subsequently, for a given velocity of injection the critical radius is found at stoichiometric mixture [12, 13]. The impact of jet momentum on turbulent jet ignition (TJI) has received various numerical investigations in literature. Increasing the jet Reynolds number may prolong ignition delay [13]. In a 2D simulation of TJI of H2-air, increasing the jet velocity and thus the turbulence intensity in the shear layer may suppress ignition due to excessive cooling [14]. By tracking the jet tip, ignition was sometimes observed at the jet crown where stream impingement strongly promotes mixing [14]. However, the ignition core may be transported towards the lateral face of the jet as the tip advances within the cold environment [15, 16]. Through a comparative assessment of literature, the authors of present work speculate about the effect of Damkohler number on the probability of ignition at the vortex or shear layer of trailing jet.

In contrast with typical IC engine geometry, the long and narrow CVC considered in the present work is typical of a wave-rotor combustion channel, with length/width aspect ratio of the

order of 10, and chamber width only about 5 times the jet nozzle diameter. Upon jet entrance, and more so after ignition, a series of pressure and expansion waves propagate in the CVC and interact with the jet and with the initiated flame through Richtmyer-Meshkov vorticity deposition, amplifying the local heat release rates [17]. The waves and the jet evolving within confining walls exhibit hydrodynamic behavior and form complex three-dimensional structures that can influence ignition. Prediction of ignition requires an accounting of jet or puff penetration and three-dimensional vortical structure evolution for the confined CVC geometry, with entrainment of fuel-air mixture. Prior numerical investigations in the literature of unconfined transient jets were often conducted using a 2D axisymmetric approach to save computational time. However, experimental observations show that even an unconfined turbulent hot jet has highly asymmetric behavior, with jet evolution and jet ignition being sensitive to small perturbation of symmetry. In a confined volume, flame propagation with wave interactions is also highly multi-dimensional. The present study employs transient 3D simulation to describe the underlying physics and chemistry of TJI in a confined volume containing CH4-H2 blend premixed with air. The study seeks criterion for ignition probability that can be used for the prediction of ignition formation.

1.3 Problem description and numerical methodology

One goal of the present study is to aid development of an experimental rig by the authors and co-workers, intended to replicate ignition in a WRC with ignition by transfer of hot gas between its channels. As shown in Figure 1-1, a cylindrical rotatable pre-chamber is used to generate a jet of hot combustion products that is precisely injected into a long rectangular CVC chamber via a converging nozzle, to create a traversing hot jet similar to that in a WRC. The pre-chamber has an internal volume of approximately 0.835 L. The CVC chamber is 40.64 cm long and has a square cross section with 3.98 cm sides. The connecting nozzle (not visible) has 6 mm exit diameter, 10° taper and 25mm length.

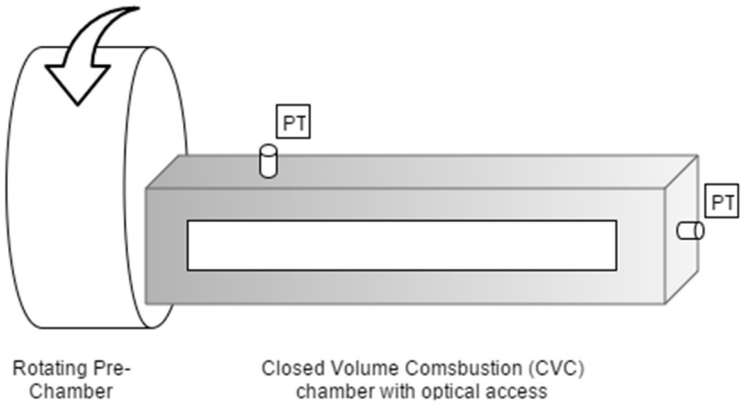

Figure 1-1: Schematic of the hot-jet ignition rig

In the experiment, the rotating pre-chamber contains fuel-air mixture and is ignited with a spark plug. The pressure of combustion eventually and predictably causes rupture of a carefully scored thin aluminum diaphragm separating the pre-chamber and CVC chamber, which also holds premixed air and fuel at slightly rich equivalence ratio. The diaphragm rupture is triggered to exactly precede traverse of one end of the CVC by the nozzle, allowing a high-speed jet of combustion products to be injected into the CVC. For the simplicity of the simulation, the pre-chamber is assumed to be filled with combustion products at equilibrium temperature and composition prior to the rupture moment. The current work focuses on the effect of two main operating conditions which are the pre-chamber pressure and the fuel reactivity in the CVC on the ignition properties and flame propagation. In the experiment, the pressure of the pre-chamber at the rupture moment can be controlled by the diaphragm scoring technique [18]. In the simulations, the pressure in pre-chamber is set as an initial condition. The fuel reactivity in the CVC is represented by different blend ratios of CH_4 and H_2.

In order to develop better insight into jet ignition and subsequent flame propagation, a set of simulations for stationary pre-chamber are conducted at which the injection pressure and fuel blends are varied, while the jet nozzle is fixed at the CVC axial centerline. The list of studied cases is provided in Table 1-1.

Table 1-1: Studied cases for stationary pre-chamber and CVC chamber

Case Number	Pre-chamber Pressure (bar)	CVC fuel blends (by volume)
1	2	Fuel-LR, 50:50 $CH_4 - H_2$
2		Fuel-HR, 30:70 $CH_4 - H_2$
3	4	Fuel-LR, 50:50 $CH_4 - H_2$
4		Fuel-HR, 30:70 $CH_4 - H_2$
5	6	Fuel-LR, 50:50 $CH_4 - H_2$
6		Fuel-HR, 30:70 $CH_4 - H_2$

For brevity, the higher reactive 30:70 CH_4-H_2 blend will be called `Fuel-HR' and the lower reactive 50:50 $CH_4$-$H_2$ blend is referred to as `Fuel-LR' in this study. The mass of each fuel blend is calculated so that the total chemical energy is almost equal in all the cases. The reactivity level of the blends is judged based on their ignition delay in a shock tube experiment [19]. Kinetic simulations done by the authors using Cantera® [20] show that on average Fuel-HR has shorter chemical autoignition delay by 76% comparing to the Fuel-LR within the temperature range of 1100-1900K at 1 bar.

Preliminary experiments suggest that slightly rich combustion in the pre-chamber provides the most rapid and consistent ignition, given ambient room conditions of pre-chamber initial mixture, for a wide range of CVC conditions [21, 22]. Therefore, the equilibrium temperature, pressure, and composition of the pre-chamber at equivalence ratio equal to 1.1 is calculated and applied to all the cases for initializing the simulation [22, 23]. The initial thermal and chemical properties of pre-chamber and CVC chamber are listed in Table 1-2.

Table 1-2: Initial equivalence ratio, temperature, and mass fraction

Thermodynamic properties	**Pre-chamber**	**CVC chamber Fuel-LR**	**CVC chamber Fuel-HR**
Equivalence ratio	1.1	1	1
Temperature(K)	2670	300	300
Pressure (atm)	2, 4 ,6	1	1
Y_{N2}	0.72364	0.72872	0.73211
Y_{O2}	0.0026	0.22144	0.22252
Y_{H2}	0.00137	0.00553	0.01023
Y_{CH4}	0	0.04431	0.03514
Y_{OH}	0.0038	0	0
Y_{O}	0.00026	0	0
Y_{H2O}	0.14883	0	0
Y_{H}	0.0000786	0	0
Y_{CO2}	0.08641	0	0
Y_{CO}	0.02991	0	0
Y_{NO}	0.0031	0	0

For the simulation of the reacting turbulent transient flow, the CONVERGE code is used [24]. Turbulence is modeled via k-ε RNG model, [25] and chemistry is modeled using the code's detailed kinetics solver, called SAGE. The reduced reaction mechanism DRM19 is used [26], which consists of 19 reactive species (plus N_2 and Ar) and 84 elementary chemical reactions, with associated thermochemical properties. In comparison with the more detailed GRI 3.0 mechanism for natural gas [27], the DRM19 mechanism showed 6-8 % deviation for ignition delay times and laminar flame speeds of mixtures at equivalence ratio of 0.2-2.0, initial pressure of 0.1-50 atm, and initial temperature of 1000-2500 K [28]. Even when employed beyond the expected temperature range of validity, GRI based mechanisms showed the best agreement with experimental measurements of jet ignition experiment [29-31]. However, the fact must be noticed

that unlike the standard ignition studies, the jet ignition produces fuel and oxidizer kernels that are highly contaminated by the active radicals generated in the pre-chamber. Therefore, the initiation elemental reaction rates are augmented which might extend the applicability of detailed mechanisms in terms of temperature. For more efficient computation, the SAGE solver uses multi-zone modeling, grouping cells in zones based on their thermodynamic state, with each zone treated as a closed-volume homogeneous reactor. In the current study, a three-variable multi-zone approach is employed which uses temperature, total equivalence ratio, and methane concentration to establish the zones with similar properties.

Employing adaptive mesh refinement (AMR), the cell size distribution is chosen to provide sufficient resolution for capturing the turbulent flame fronts and reasonable representation for pressure waves. Using a preliminary estimation of viable ignition kernel size based on William's ignition criterion [32] to be about 0.1 mm, the mesh refinement is adjusted to place 8 to 10 computational cells in ignition initiation regions to ensure adequate resolution for ignition detection and ability to resolve the flame thickness. A total cell count as high as 10 million was reached as the cell size was adaptively refined to uniformly resolve temperature and velocity gradients. Figure 1-2 shows the numerical domain and refined grid utilized for the simulations. In the current work, a spatial discretization scheme with 2^{nd} order accuracy and a fully implicit first-order accurate time-integration scheme are used to solve the governing conservation equations. A variable time scale algorithm is used, with time-step varied between 10^{-8} and 10^{-5} seconds. The transport governing equations are solved by the PISO method of Issa [33]. Based on velocity and local speed of sound, the time-step is maximized to ensure stability in each computational cycle. The computational facility used in this study is a 64-node sector of Indiana University's BIG RED II supercomputer.

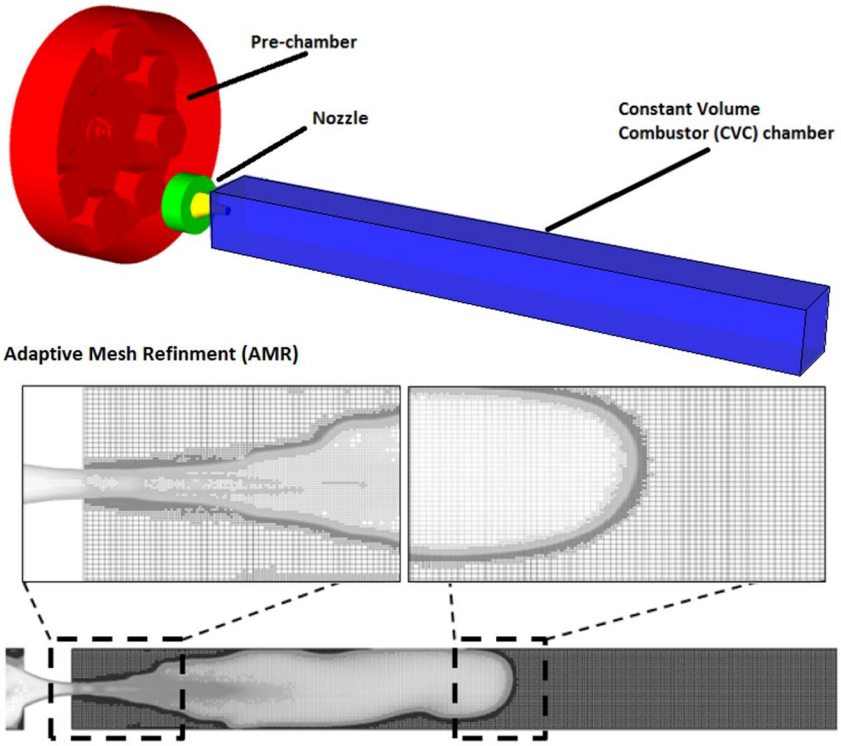

Figure 1-2: The 3D numerical domain and local mesh refinement employed for turbulent ignition and deflagration

1.4 Characteristics of ignition

1.4.1 Validation with PFR analysis

To validate aspects of the approach, representative numerical simulations are first compared with another recognized study. The ignition location obtained by the simulations are compared with the semi-empirical model developed by Fink and Vanpee [10] which employs plug-flow reactor (PFR) analysis to make a correlation between jet velocity, ignition distance, and rate constants of the global reaction rate. The simplistic model assumes that mixing of the hot jet and CVC mixture happens much faster than the chemical time scale and also that ignition occurs closer to the hot jet rather than the cold mixture with respect to the mixing shear layer. Therefore, the process is modeled as a PFR in which a portion of fuel and oxygen is diluted in a batch of active hot gas, and the chemical kinetic process begins. The mixture would ignite after undergoing conversion during a contact time, $\frac{z}{U_{cl}}$ which can be formulated as:

$$\frac{z}{U_{cl}} = \int_{Y_i^O}^{Y_i^F} (M_i \, \rho \, dY_i)/W_i \qquad \text{Eq. 1-1}$$

Where U_{cl} and z are jet velocity at the nozzle centerline and ignition distance from the nozzle, respectively. The reaction rate W_i used in Eq. 1-1, for the fuel is of the form:

$$W_f = A \, M_f \, e^{-\frac{E}{RT}} \left(\frac{P}{RT}\right)^{C+D} Y_f^C \, Y_O^D \qquad \text{Eq. 1-2}$$

where A and M_f are pre-exponential constant and fuel molecular weight, respectively. Substituting the rate reaction of Eq. 1-2 into the integral and applying the logarithm to both sides, the integral yields;

$$\log\left(\frac{U_{cl}}{z}\right) = -\frac{E}{RT} + \log\left(\frac{Y_F^C Y_O^D A}{Y_O - Y_F}\right) - (C + D - 1)\log(T/P) \qquad \text{Eq. 1-3}$$

T, P and R are jet temperature, CVC pressure and gas constant, respectively. E is the activation energy and C+D is total order of reaction. According to Eq. 1-3, for a given fuel mixture, the quantity $\log\left(\frac{U_{cl}}{z}\right) + (C + D - 1)\log(RT/P)$ vs. $\frac{1}{T}$ should generate a linear plot with a slope of $-\frac{E}{R}$. It is implied by Eq. 1-3 that if the jet temperature and fuel-air composition of the CVC are kept constant, the variation of ignition distance with respect to the jet velocity should adjust itself in a fashion that $\log\left(\frac{U_{cl}}{z}\right)$ remains nearly constant.

Table 1-3 displays the left-hand side value of Eq. 1-3, $\log\left(\frac{U_{cl}}{z}\right)$, for different jet momentum (pre-chamber pressures) along with the corresponding jet velocities and ignition distances. The jet velocity is read on the centerline one diameter downstream of the nozzle tip and the ignition distance is identified by the abrupt rise of OH concentration in the spatial field. For the present cases of study, E is assumed to be equal to 37.79 kcal/mol based on the study of Zhang et al. [19] that examined the ignition delay of H_2-CH_4 blends in the shock tube experiment. The order of global reaction with respect to the tri-component reactant is known to be 1.1 [10]. This value is developed by establishing a relation between rate of global reaction and laminar speed of the flamelets. As expected by Eq. 1-3, the value of $\log\left(\frac{U_{cl}}{z}\right)$ does not vary significantly by changing the pre-chamber pressure which controls the jet momentum. This behavior is consistent with the observations of Sangras et al. [34], which showed the self-preserving properties of developing turbulent jets in a still environment.

Table 1-3: Verifying the self-preserving development of the hot jet ignition

Jet Temperature:2670 K, CVC Fuel-HR

Pre-chamber pressure (bar)	**U (m/s)**	**z (cm)**	$\log\left(\frac{U_{cl}}{z}\right)$
2	700	8.4	3.92
4	860	13.1	3.81
6	1000	14.5	3.83

1.4.2 Comparison with literature

There are only a few experiments and numerical efforts reported on ignition by a hot jet in a confined volume that are closely similar to the present work. Two of the critical factors discussed in the literature which are known to strongly influence the jet ignition delay are orifice diameter and the fuel reactivity in the CVC. Mayinger et al. investigated the scalability of jet ignition devices by employing various orifice diameters and measuring the ignition delay [35]. It was shown that with orifice diameter of 6 mm, the reported ignition delay for propane-air mixture at the mixture equivalence ratio of 0.62 is below 2 ms. This result would agree with all of the findings of the present study that are done with a 6 mm nozzle size. In another similar study conducted by Ghorbani et al. [15] it is stated that for jet ignition of hydrogen-air mixture, the ignition delay varies in the range 0.1-0.4 ms, depending on the jet entrance temperature. In the present work, for the hydrogen-dominated mixtures (70%H_2-30%CH_4), the ignition delay is approximately 0.8 ms which reasonably agrees with Ghorbani's.

Preliminary experiments using the ignition rig modeled in Paik's study [21] examined the significance of jet momentum on the ignition delay of methane-hydrogen fuel blends. Figure 1-3 presents a comparison between the experimental and numerical measurements of ignition delay for similar fuel blends at standard condition. The trend of decreasing ignition delay with higher jet momentum is supported. The shorter predicted ignition delay likely stems from higher jet temperature comparing to the experiments. Based on ongoing (unpublished) infra-red imaging of the jet in the experimental rig, the jet temperature during discharge is lower than the pre-chamber temperature postulated in the present simulations, mainly due to unaccounted heat losses.

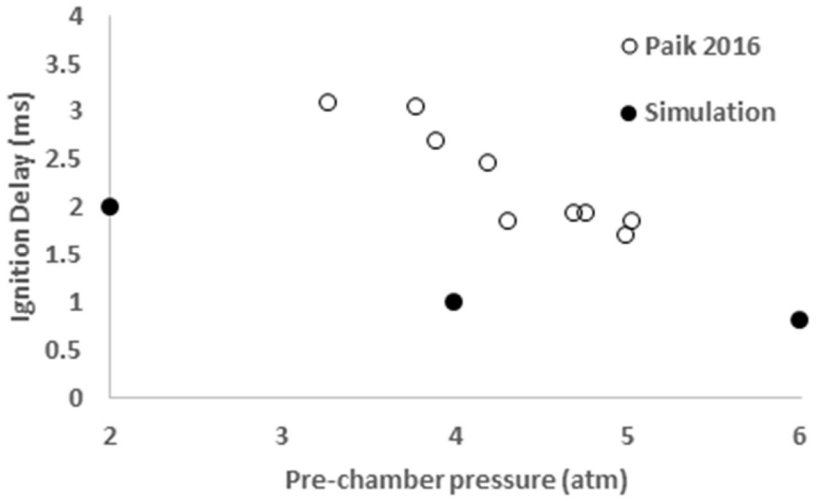

Figure 1-3: Minimum ignition delay measurements for 70%H2-30%CH4 fuel blend

1.4.3 Effects of pre-chamber pressure and CVC chamber fuel reactivity

For ignition by a jet of reactive hot gas, there is an important physical mixing process that occurs before chemical reactions can begin, yet the injected hot jet should ideally remain chemically active while the jet mixes with relatively cold reactive gas.

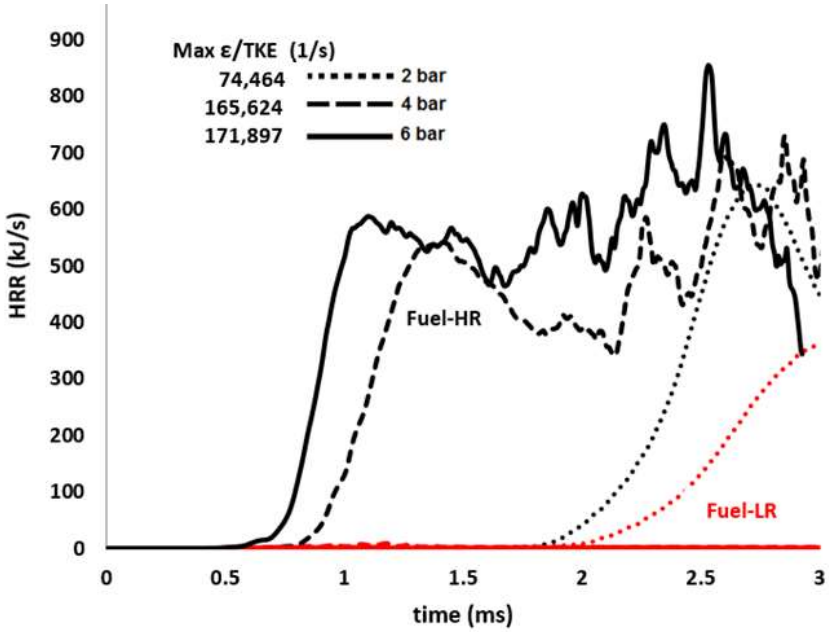

Figure 1-4: History of heat release rate with varied fuel reactivity and jet momentum

The ignition delay in a jet-ignited CVC can be defined as the time from the emerging of the initial hot jet to the appearance of rapid pressure-generating heat release. The authors observed that ignition often occurs where fuel, air, and injected hot gas are mixing in small distinct regions that are within the critical ignition kernel size and are experiencing temperature above auto ignition conditions for that particular composition.

The instantaneous heat release rate (HRR) accompanied with the local OH production in the CVC is used to indicate the ignition delay. The computed history of the reaction heat release rate (J/sec) in the CVC chamber is depicted in Figure 1-4. The ignition event can be recognized by the sudden rise of HRR curve.

For Fuel-HR, Figure 1-4 reveals the positive effect of increasing jet momentum on shortening the ignition delay. Also, all of the simulations for the Fuel-HR led to a successful ignition event whereas for Fuel-LR, the ignition only occurs for pre-chamber pressure of 2 bar, whereas for higher jet momentum, no significant reaction is initiated during the simulation time of 3 ms. The opposite effect of the jet momentum on the ignition delay for Fuel-HR compared to Fuel-LR is notable and needs to be addressed. As discussed earlier, the ignition success is decided by two processes acting in parallel: the hot jet providing the thermal energy and some radicals, and the heated reactant mixture undergoing initiation reactions leading up to ignition. If the chemical time scale (τ_{ch}) which is inversely related to fuel reactivity is longer than the mixing time scale (τ_{mix}), the batch of fuel-air containing hot gases might cool down due to excessive mixing with the cold environment before it can launch the ignition reactions.

The amount of turbulence induced by the high velocity jet plays a major role in mixing the two fluids. Turbulence is generated in the jet shear layer as long as the jet velocity remains high. Also, the gradual growth of the jet tip vortex (also known as the jet crown) has a considerable contribution to the turbulence generation. The rate of jet and ambient mixing can be directly related to the pre-chamber pressure as it influences the jet momentum and turbulence intensities. Thus, more entrainment of cold gases to the hot jet is expected as the jet momentum rises. To further emphasize the effects of turbulent mixing, the ratio of turbulence energy dissipation to the turbulent kinetic energy, (ε/TKE), which varies inversely with the turbulence timescales. The maximum value of ε/TKE attained during the simulation time is provided in Figure 1-4. The maximum ε/TKE ratio rises with jet momentum, increases mixing and shortens τ_{mix}.

The competition between the two time scales can be inferred from Figure 1-4. For the higher reactivity fuel, Fuel-HR, τ_{ch} is short enough to allow the mixing process to control the ignition progress. Therefore, as the jet momentum increases, ignition delay reduces due to the enhanced mixing and heat exchange between hot jet and cold ambient mixture. The overall trade-off between chemical and mixing time scale for the Fuel-HR shortens the ignition delay by increasing the jet momentum. In contrast, for the Fuel-LR, the chemical reactions are relatively slower and τ_{ch} seems to be controlling the ignition process. For higher values of jet momentum, the excessive mixing and jet quenching prevents ignition within the simulation time limit of 3 ms.

Another significant observation from Figure 1-4 is the fluctuations of the HHR after the ignition onset at 4 and 6 bar pre-chamber pressures. The fluctuations are seemingly accompanied by the pressure wave-flame interactions, which can locally alter the burning rate via multiple effects. These effects are beyond the scope of this work.

Figure 1-5 is a plot of the time history of temperature distribution on the midplane crossing the nozzle and CVC chamber for the Fuel-LR and Fuel-HR, respectively. The OH iso-curves are overlaid on the temperature plots emphasizing the ignition moment. It appears that ignition is successful when OH mass fraction exceeds a threshold of about 0.007. The ignition kernel is generally located at the jet tip vortex where high entrainment of reactants into the hot jet is expected. Subsequently, the reaction region spreads towards the lateral surfaces of the jet. In these cases of a centered stationary jet, the ignition kernel occurs near the centerline, but it appears that the growth of the kernel and subsequent combustion propagation is highly influenced by the narrow confinement in the CVC. Figure 5-top illustrates the ignition occurrence for the Fuel-LR under different jet momentum. As was addressed by the HRR in Figure 1-4 for the Fuel-LR, successful ignition happens only for the pre-chamber pressure at 2 bar around 2.2 ms while faster jets fail to ignite within the simulation time limit. It should be noted that the late ignition (later than 3 ms in the present study) may be considered unsuccessful in cyclic combustion devices with limited available time. When the ignition kernel fails to be formed at higher jet momentum, it is mainly due to the time scale argument made earlier. The Fuel-LR has a longer chemical time scale because of its lower hydrogen content. The hot jet at high jet momentum has a shorter mixing time scale. As discussed, higher jet momentum causes stronger turbulence and faster mixing with the cold environment. Thus, before the jet can ignite the Fuel-LR, it loses its thermal energy due to the excessive mixing rates.

As depicted in the Figure 1-5-bottom for the Fuel-HR, evidence of ignition at 2 bar pre-chamber pressure appears around 2ms after the jet discharge. This delay is significantly reduced as the jet momentum increases, so that at 6bar, the ignition kernel is formed roughly at 0.8 ms. The higher concentration of hydrogen in the Fuel-HR seemingly allows the reactions to progress much faster than for the Fuel-LR. Consequently, once the appropriate temperature is attained by the fuel mixture due to mixing with hot jet, ignition takes place. It is also worthwhile to notice the development of perturbations on the flame front as the combustion proceeds. These effects develop in the form of twisting and distorting of the flame front which can generally extend the effective reaction area. The detailed calculations of the flame surface show that in some instances, the flame area can stretch 30 times larger than the channel cross section.

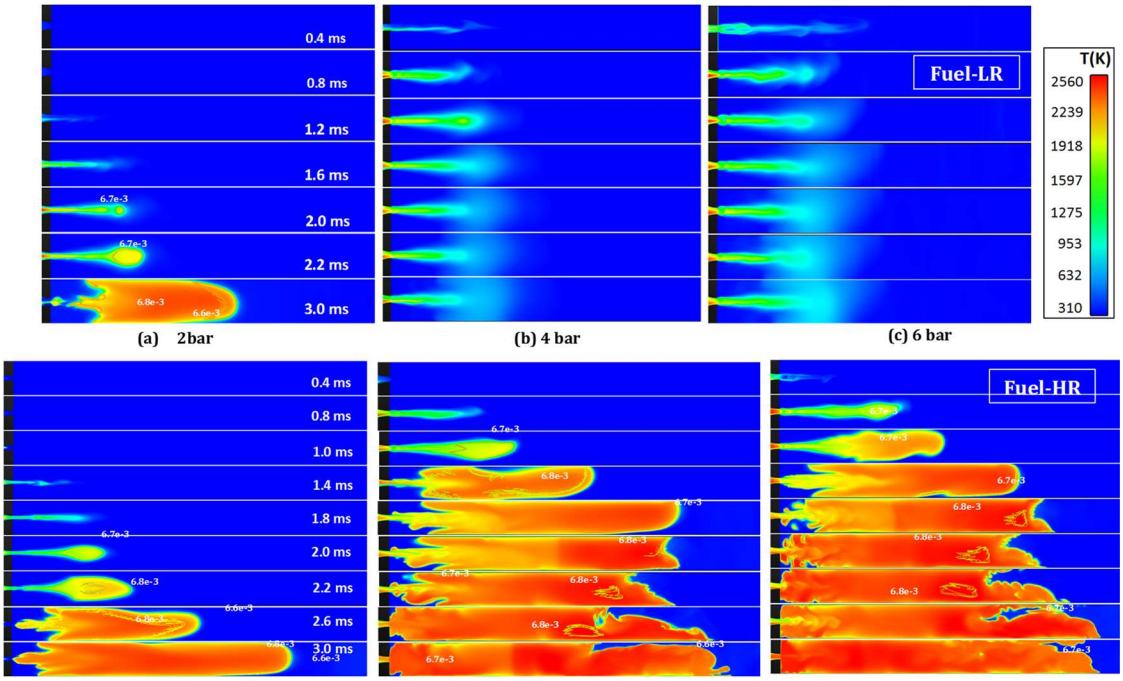

Figure 1-5: History of temperature overlaid by OH iso-curves in CVC chamber for Fuel-LR (top) and Fuel-HR (bottom) at the pre-chamber pressures of (a) 2 bar, (b) 4 bar and (c) 6 bar. Pictures are not to scale.

1.5 Ignition: a function of species concentration and temperature

A goal of the study is to predict the time and possibly the location of ignition at operating conditions that are not simulated in detail as reactive flows. For instance, if the jet has a traversing motion or the CVC mixture is at elevated temperature, are we able to predict the ignitability of the

mixture? Given the substantial cost of reactive flow simulations, is it possible to obtain sufficient guidance from non-reactive flow simulations of the mixing process?

Active radicals in the hot jet, such as CH_x and OH, mix with the reactants and have been shown to play a significant role in the ignition process [22]. Thus, global reaction models for autoignition of unreacted mixture cannot quantify reaction rates. A simpler ignition criterion could be based on the presence of a certain concentration of reactants and temperature. By examining the simulation results with a post-processor, it is possible to track flow particles based on their origin whether it the pre-chamber or CVC. The authors studied the simulation results of successful ignitions in 12 cases [21] and discovered that at the ignition kernel (a sphere with critical size) the temperature, mass fraction originating in hot jet gases, and mass fraction originating in cold reactants in the CVC should be within certain ranges. Collecting all the data from previous simulations and aiming to develop a baseline, a Boolean ignition indicator called IGN was defined which represents the thermochemical properties of the ignition points achieved in the successful ignition cases. The variables and their limits were chosen as follows, based on a trial-and-error process of identifying the time and locations of ignition in the above-described simulations:

"IGN" = (0.1<Pre-chamber mass fraction<0.2) and (0.55<CVC chamber mass fraction<0.6) and (Temperature>750 K)

When the ranges of all three variables are met simultaneously, cells are observed to have sustained reaction. It must be noted that the remainder of the mass in IGN criterion is constituted from the diluent which is used to purge the nozzle assembly. In the configurations otherwise, the mass fractions need to be normalized.

IGN as an indicator could reduce the necessity of using computationally costly chemistry models, allowing non-reacting flow mixing study to establish likelihood of ignition. In support of the recommended temperature interval, the Semenov approach of thermal ignition suggests that for methane-hydrogen blend with activation energy about 180 kJ/mol and the mixture initial temperature of 750K, only 25K of temperature rise is sufficient for ignition occurrence [36]. Also, due to importance of active radicals on ignition at near-atmospheric initial condition of CVC, IGN is designed to represent the composition of the pre-chamber [37].

In order to examine the viability of the IGN criterion, an attempt is made to predict the ignition time for a case where the hot jet has a traversing motion, which has different jet physics.

In a wave rotor combustor, for example, hot gas supplied by a pre-chamber or a prior-combusted chamber is transferred to a fresh-mixture chamber that is in motion relative to the transfer jet nozzle. Thus, depending on the rotational speed of the rotor, the CVC is experiencing a traversing jet along the end of the channel. Simulations of these cases were performed with and without inclusion of chemical reaction calculations, and ignition predictions from the two methods were compared. In the top plot of Figure 1-6 red markers represents IGN for the cells were the ignition criteria is met. It should be noted that the IGN is developed in the 'cold' flow simulation where the chemical reaction calculations are turned off. In the lower plots, the mid-plane temperature is shown for simulations with chemical reactions included, from which ignition can be directly predicted.

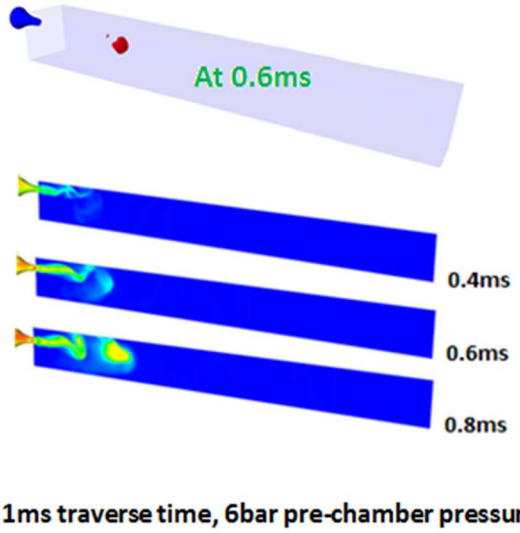

Figure 1-6: Comparison of IGN prediction of the ignition time and location (top) with the corresponding moment at the reacting flow simulation (bottom). Jet traversing speed 12.8 m/s, Pre-chamber pressure 6bar, Fuel-HR

As depicted in Figure 1-6(top), the full simulation predicts ignition at around 0.6 ms based on temperature field with chemical reaction included. Encouragingly, IGN predicts ignition at about the same time and location in the non-reacting flow simulations.

Table 1-4 is a comparison of the ignition time observed in combustion simulations along with the values predicted by IGN in the cold-flow simulations. The errors reported in Table 4 are inclusive of inherent uncertainties of IGN in predicting the actual ignition time as well as an additional 0.05 ms error contribution due to the time intervals at which the computational results are saved for postprocessing, due to storage limitations.

Another operating condition to be considered in applications of constant volume combustors is the CVC mixture temperature prior to jet injection. Combustion engines have varying levels of compression, and thus temperature of the mixture varies. In order to probe into the effect of elevated CVC temperature on combustion, a new set of simulations with and without chemical kinetic calculations were conducted in which the reliability of IGN in predicting the ignition time was examined. This comparison is also presented in Table 1-4, where Fuel-HR mixtures initially at 514 K are simulated. It is noted that the IGN variable substantially captures the strong downward trend in ignition delay time with increasing jet momentum.

Table 1-4: Accuracy of IGN ignition predictor with introduction of jet traverse (top) and elevated CVC temperature (bottom)

Traversing Jet speed (m/s) †	Reacting flow Ignition time (ms)	IGN Ignition time (ms)	absolute error (ms)
12.8	0.65	0.60	0.05
4.9	0.70	0.60	0.1
0.9	0.90	0.70	0.2

CVC initial temperature 514K‡		Reacting flow Ignition time (ms)	IGN Ignition time (ms)	absolute error (ms)
Pre-chamber pressure (bar)	2	1.70	1.75	0.05
	4	0.75	0.80	0.05
	6	0.70	0.60	0.2

†Pre-chamber pressure 6 bar, CVC temperature 300 K, Fuel-HR

‡ CVC elevated temperature 514 K, Fuel-HR

1.6 Conclusion

The ignition and deflagration of air-CH4-H2 mixtures with initial standard pressure and temperature in a confined volume is numerically simulated and different operating conditions are studied with 3D simulations. The jet composition and temperature corresponded to the adiabatic

equilibrium products of a slightly-rich fuel-air mixture. The following highlights were addressed in the present work:

- The pre-ignition development of the jet demonstrates self-preserving behavior as expected by the plug flow reactor model.
- The competition of the mixing and chemical time scales determines the success of ignition. Observations show the substantial decrease of the ignition delay with increasing the jet momentum for the hydrogen-dominated fuel blend, while its effect on the low-reactivity fuel blend is weakly in the opposite direction of quenching ignition.
- Experimental data for the same geometry and high-reactivity fuel blend as used in the simulations showed trend of ignition delay variation with jet momentum that was consistent with numerical model predictions, but with higher values that were expected due to suspected heat loss effects in the experiments that were not accounted in simulations.
- An ignition predictor variable (IGN) was developed and examined for estimation of ignition time and location while the cold flow was being simulated and no chemistry model is engaged. The IGN criterion is designed to benefit preliminary benchmarks for design of a CVC for combustion applications. IGN showed reliability for 3:7 and 1:1 methane-to-hydrogen ratios at near atmospheric pressures in comparison with chemical kinetic flow reactor calculations.
- The IGN criterion as established for non-traversing jet and for CVC mixture at room temperature was able to acceptably predict ignition delay for jets with traversing motion over a range of speeds, as well as for CVC mixtures with elevated initial temperature with a range of jet momentum, in comparison with chemical-kinetic flow reactor calculations.

- While the ignition is sensitive to the jet composition, IGN criterion presumes the jet composition to be the equilibrium products of a slightly rich-burn combustion at temperatures close to adiabatic flame.
- The IGN criteria used fixed values for three constituent variables across a significant variation in the physics-related variables of jet momentum, jet traverse speeds, and the chemistry-related variables of initial CVC mixture temperature and fuel reactivity.
- It is noted that the criteria might be only trusted for high aspect ratio and narrowly confined elongated combustors. Within the defined operating conditions, the IGN variable is shown to be able to predict the ignition time with precision ranging from 0.05-0.2 ms depending on the complexity of jet structure.

The study has been beneficial in suggesting a methodology for predicting ignition from lower-cost computations without chemistry calculations. The values of variables in the ignition criterion may be refined by further modeling and comparison with experiments, and by considering an expanded parameter space including varying the pre-chamber and CVC fuel/air ratio, and nozzle diameter.

1.7 Acknowledgements & ethics compliance

This work is based on the Purdue University MS thesis of M.N. Khan. This work was partially supported by the US National Science Foundation under Grant No. CBET-1235696. Author Nalim has received funding from Rolls-Royce Corporation for prior related work, holds US patents related to wave rotor combustion, and is a co-owner of Aerodyn Combustion LLC. The authors declare that they have no other conflicts of interest.

2. LARGE EDDY SIMULATION OF HOT JET IGNITION IN MODERATE AND HIGH-REACTIVITY MIXTURES

Acknowledgment: This is a post-peer-review, pre-copyedit version of an article published in Computers and Fluids. The final authenticated version is available online at: https://doi.org/10.1016/j.compfluid.2019.03.014

2.1 Abstract

Hot jet ignition technology is a promising improvement to conventional spark ignition for reducing emissions in premixed combustion engines as it can extend the lean-burn limits. In addition, the rapidity of the ignition via hot jet makes this technology appropriate for deflagrative pressure-gain combustors using a wave rotor, which have high-frequency operation and fast-burn requirements. In order to improve the controllability of the ignition process, the thermofluidic and chemical mechanisms by which the ignition is promoted need to be rigorously elaborated. In the present work, the chemical thermofluid dynamics of a transient turbulent hot jet in a reactive environment is studied via large eddy simulation (LES) with detailed kinetic chemistry. Computational model of the reacting and non-reacting jets are presented, analyzed and compared to the available experimental data. Various mesh sizes in conjunction with adaptive mesh refinement were tested to ensure the insensitivity of the solution to the grid. To quantify the effect of main chamber fuel reactivity on the ignition process, two different blends of methane-hydrogen under the same equivalence ratios are tested and the effective thermo-chemical mechanisms of ignition are investigated. It is understood that the ignition kernels emerge at the regions with minimal scalar dissipation rate, mainly at the trailing shear layer of the jet, and are partially transported to or formed at the head vortex. The temporal variation of the heat release rate and formaldehyde distribution at the fuel mixture with lower hydrogen content suggests that auto-ignition is responsible for the subsequent flame formation. However, for higher hydrogen content, it is observed that auto-ignition is not as prolonged beyond the initial kernels, while the propagating premixed flame that emanates from the shear layer mostly comprises the overall heat release.

Keywords: Hot jet ignition, LES, auto-ignition.

2.2 Introduction

Deflagration initiation by injection of hot gas into a fuel-air mixture is important in combustion engines, explosion protection and fire safety. Turbulent hot-jet ignition can be a reliable means of rapid ignition for lean-burn devices such as stratified IC engines and wave rotor combustors [38]. Ignition by a turbulent jet was mainly established in the 1950's by Noble-prize-winner Nikolai Semenov [6] and was further elaborated by Gussak et al., [39] and Oppenheim [8] for IC engine applications. The penetrative hot jet which contains chemically active radicals can act as a distributed source of ignition throughout the combustion chamber. The turbulent-hot jet ignition technology has been investigated in prototype combustion chambers [40-42], rapid compression machines [31, 43], and real-world internal combustion engines [44-46]. The hot turbulent jet is typically generated by burning a small fraction of stoichiometric or slightly-rich fuel/air mixture in a separate small volume – a pre-chamber. The higher pressure caused by combustion in the pre-chamber drives a mixture of burnt/partially-burnt/unburnt gases into the main chamber in the form of a hot and reactive turbulent jet [47]. The ignition in the main chamber is then attained as the result of thermal and chemical interaction of the turbulent hot jet with the fresh reactants contained in the main combustion chamber (large or small-scale mixing) [42]. The ignition often occurs at the locations of the mixing region where fuel, air, and injected hot gas are consistently present within the critical ignition kernel size and experience thermochemical conditions which support ignition [1]. A major advantage of jet ignition is the enabling of fast burn rates due to producing multiple, distributed ignition sites, which rapidly and pervasively consume the main charge [45]. Due to the rapidity of jet ignition and ability to accommodate relative motion between the pre-chamber and main chamber, this method is employed in development of wave-rotor pressure-gain combustors which need very short ignition delay and combustion duration [23, 38]. In this paper, we do not consider the effect of traversing motion of the jet as present in a wave rotor combustor .

The use of a small fuel-rich pre-chamber, ignited to produce hot gas jets offers a simplified and effective solution for lean-burn devices and requires minimum engine modifications comparing to plasma-assisted ignition [48], laser ignition [49], or artificially enhanced vortex generator [50].

Due to the significant difference in pressure between the pre-chamber and the main combustion chamber, the resulting transient turbulent jet exhibits complex spatial and temporal development. In the confined volume of the main chamber, the ignition process is even more complex as the walls interact acoustically and aerodynamically with the developing jet [1].

In recent years, high fidelity numerical simulations have been utilized to study the formation of ignition kernels and subsequent flame formation and propagation prompted by hot jet ignition [51-53]. These studies provided insight into the physics of the premixed flame propagation and auto-ignition occurring with respect to various scalar domains. Ghorbani et al. [54] conducted numerical simulation of hot turbulent jets ignition and found that the competition among time scales of chemical reaction, small scale mixing (turbulent diffusion) and large scale mixing (engulfment of the reactants by hot gas) determines the success of the overall ignition and the location of the ignition sites. Validi et al. [52] carried out a fundamental numerical study to understand the underlying physics of ignition via developed hot jets. They identified three main combustion zones, i.e. hot product jet, burned-mixed, and the flame zone. Qin et al. [51] investigated the transient mixing and ignition mechanism in pre/main chamber configuration using direct numerical simulation of the reacting flow. They identified important phases in ignition and flame propagation based on the trends of pressure, velocity and important species namely, OH, CH_2O and HO_2 at typical points in pre-chamber and main chamber. They realized that the jet contribution to ignition is via three major pathways, i.e. chemical, thermal and fuel enrichment effects. The unburnt gas reactivity inside the pre-chamber is addressed by the recent work of Wang et al. [55] who studied the effect of CO/H_2 ratio in the pre-chamber on flame formation and propagation in the main chamber. Design of robust igniters requires understanding of how the mixture fraction and scalar dissipation fields develop during hot jet ignition. In the present context, mixture fraction represents the fraction of nozzle-generated specie to the total mass of the gas. Scalar dissipation rate (SDR) quantifies the molecular mixing rate of the mixture fraction and is represented in the present study by the square of the gradient of mixture fraction. High SDR may result in extinction of the flame and do not favor local ignition growth [56, 57]. In the work of Soloupolus et al., [58], SDR of a non-reacting starting jet was studied and it was noted that the highest SDR values appear at the jet boundary. High-resolution LES of transient starting jets done by Inanc et al. [53] reaffirms the high presence of SDR in the mixing layer stationed at the interface of vortex and trailing shear zones of the jet, with the surrounding gas. The mixing region is the

most supportive zone that may provide proper thermochemical conditions for understanding of ignition occurrence. However, high levels of SDR are likely to emerge in the mixing region. This seemingly contradictory coexistence partly inspired the present study.

The reactivity of fuel-air mixture of the main chamber may alter with the composition of practical gaseous fuels such as natural gas, shale gas or syngas [59]. Moreover, the reactants in the main chamber may experience vast variations of reactivity due to the presence of the combustion residual mass or variation of initial temperature across the wide range of combustor applications. The effect of fuel reactivity on the dynamics of turbulent jet ignition has not been widely studied in literature. This also has motivated the current study, which aims to develop understanding of the hot jet ignition process at two distinct reactivity levels of the fuel in the main chamber. In order to simulate different fuel reactivity levels, CH_4-H_2 blend is adopted. This methodology has been used in experiments by Kojok [60] and Chowdhury [61], which are presently considered. The study seeks to describe the underlying physics of turbulent jet ignition in a confined volume containing stoichiometric CH_4-H_2 blends premixed with air, by employing a well-resolved transient 3D large-eddy simulation with detailed kinetics. The study sheds light on the volumetric ignition process, which can be used to predict the mechanisms of ignition development based on fuel reactivity. The insight developed by this study would be leveraged for the design of deflagrative pressure-gain combustors which must demonstrate high fuel flexibility and rapid combustion rate.

2.3 Numerical methodology

Numerical simulation of the reacting flow is conducted using LES of a suddenly-starting turbulent jet. The equations of transport are discretized and solved using the method of PISO proposed by Issa [33]. For the computations, Indiana University's supercomputer, BIGREDII provided a 100-node sector wherein each node contains two AMD Opteron 16-core x86_64 CPUs and 64 GB of memory. Figure 2-1 presents the memory allocation and grid cell distribution over the computational resources. The computational domain is typically filled with 70M cells with the total memory requirement of 2.75 TB and the walltime of 7000 CPU-hr.

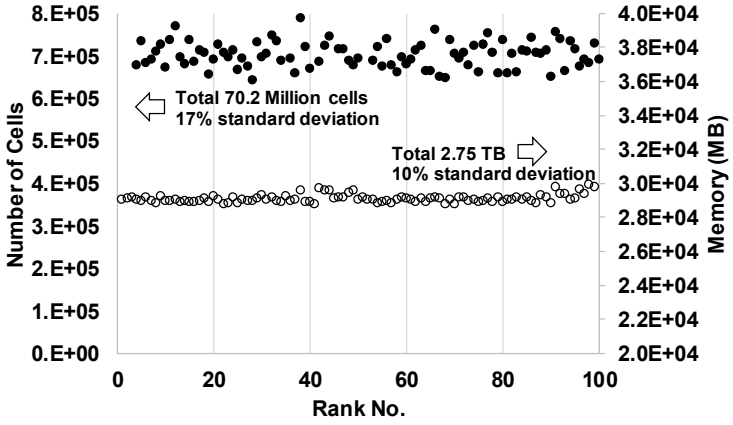

Figure 2-1: Distribution of computational cells and allocation of memory to the HPC ranks

In this work, the Favre-averaged compressible form of the Navier-Stokes equations are solved in LES [62],

$$\frac{\partial \bar{\rho}}{\partial t} + \frac{\partial \bar{\rho}\widetilde{u_j}}{\partial x_j} = 0, \qquad \text{Eq. 2-1}$$

$$\frac{\partial \bar{\rho}\,\tilde{u}_i}{\partial t} + \frac{\partial \bar{\rho}\tilde{u}_i\tilde{u}_j}{\partial x_j} = -\frac{\partial \bar{P}}{\partial x_i} + \frac{\partial \bar{\sigma}_{ij}}{\partial x_j} - \frac{\partial \tau_{ij}}{\partial x_j} \qquad \text{Eq. 2-2}$$

where u_i is velocity, ρ is density, P is pressure and σ_{ij} is the stress tensor defined as follows;

$$\sigma_{ij} = \mu\left(\frac{\partial \tilde{u}_i}{\partial x_j} + \frac{\partial \tilde{u}_j}{\partial x_i}\right) + \left(\mu' - \frac{2}{3}\mu\right)\left(\frac{\partial \tilde{u}_k}{\partial x_k}\delta_{ij}\right) \qquad \text{Eq. 2-3}$$

The effect of the small scales appears through a subgrid-scale (SGS) stress term,

$$\tau_{ij} = \bar{\rho}\left(\widetilde{u_i u_j} - \tilde{u}_i\tilde{u}_j\right). \qquad \text{Eq. 2-4}$$

The SGS term is modeled using the dynamic-structure LES [63, 64] model to approximate the stress tensor at the SGS level by adding a sub-grid kinetic energy equation,

$$\frac{\partial \bar{\rho}\,k}{\partial t} + \frac{\partial \bar{\rho}\tilde{u}_j k}{\partial x_j} = \frac{\partial}{\partial x_j}\left(\frac{\mu}{Pr_{SGS}}\frac{\partial k}{\partial x_j}\right) + \tau_{ij}\bar{S}_{ij} - \rho\epsilon\ , \qquad \text{Eq. 2-5}$$

where Pr_{SGS} is set to 1. The SGS kinetic energy and dissipation rate are given by the following equations,

$$k = \frac{1}{2}\left(\widetilde{u_i u_j} - \tilde{u}_i\tilde{u}_j\right), \qquad \text{Eq. 2-6}$$

$$\epsilon = C_e\frac{k^{1.5}}{\Delta}, \qquad \text{Eq. 2-7}$$

where C_e is equal to 1 and Δ is the local grid length scale. The SGS stress tensor (τ_{ij}) is thus modeled by

$$\tau_{ij} = 2k\bar{\rho}\frac{L_{ij}}{L_{kk}}, \qquad \text{Eq. 2-8}$$

In Eq. 2-8, L_{ij} is the Leonard stress tensor and is defined as $L_{ij} = \widehat{\tilde{u}_i}\widehat{\tilde{u}_j} - \widehat{\tilde{u}_i}\widehat{\tilde{u}_j}$. The "$\widehat{\ }$" symbol indicates the test-level filter which is larger than the sub-grid level and has the benefit of being resolved.

Unlike the momentum equation where the dynamic-structure model is used to avoid use of eddy viscosity approximation at sub-grid level, for the scalar transport equations an eddy viscosity concept is used. LES decomposition of scalar transport equations creates another unclosed term. As recommended in [65], to close the LES transport equation, a turbulent-diffusion model is used where the turbulent diffusivity is given by

$$D_t = \frac{C_k \Delta k^{0.5}}{Sc} \qquad \text{Eq. 2-9}$$

In the above equation, the model constant is set to 0.5 and the turbulent Schmidt number (*Sc*), set to 0.699 in the present simulations. The turbulent Schmidt number is calculated based on the average mass fraction of the species in the mixing zone. With the help of the scalar turbulent diffusion model, the Favre filtered species and energy conservation equations are established as follows.

Species conservation:

$$\frac{\partial \bar{\rho}\,\widetilde{Y_n}}{\partial t} + \frac{\partial \bar{\rho}\,\tilde{u}_j\,\widetilde{Y_n}}{\partial t} = \frac{\partial}{\partial x_j}\left(\bar{\rho}(D + D_t)\frac{\partial \widetilde{Y_n}}{\partial x_j}\right) + \bar{\dot{\omega}}_n\,, \quad n = 1,2,3,\ldots\ldots,m \qquad \text{Eq. 2-10}$$

Energy conservation:

$$\frac{\partial \bar{\rho}\,\tilde{e}}{\partial t} + \frac{\partial \bar{\rho}\,\tilde{u}_j\,\tilde{e}}{\partial t} = -\bar{P}\frac{\partial \tilde{u}_j}{\partial x_j} + \bar{\sigma}_{ij}\frac{\partial \tilde{u}_i}{\partial x_j} + \frac{\partial}{\partial x_j}\left(K_t\frac{\partial \tilde{T}}{\partial x_j}\right) + \frac{\partial}{\partial x_j}\left(\bar{\rho}(D + D_t)\sum_{n=1:m}\widetilde{h_m}\frac{\partial \widetilde{Y_m}}{\partial x_j}\right) + S^e \qquad \text{Eq. 2-11}$$

In the above equations, Y_n is the mass fraction of species *n*, ρ is density, *D* is molecular diffusivity, D_t is turbulent diffusivity, $\bar{\dot{\omega}}_n$ is the reaction source term, *e* is the specific internal energy. The turbulent conductivity in the energy equation is estimated as $K_t = C_p\frac{\mu_t}{Pr_t}$, where μ_t is the turbulent viscosity, Pr_t is the turbulent Prandtl number and C_p is specific heat. In the energy equation, the pressure work resulting from compression or expansion is given by the term $-\bar{P}\frac{\partial \tilde{u}_j}{\partial x_j}$,

viscous dissipation of kinetic energy is given by $\overline{\sigma_{ij}}\frac{\partial \widetilde{u_i}}{\partial x_j}$, and the energy transport due to species diffusion is given by the term $\frac{\partial}{\partial x_j}\left(\bar{\rho}(D+D_t)\sum_{n=1:m}\widetilde{h_m}\frac{\partial \widetilde{Y_m}}{\partial x_j}\right)$.

The computational-fluid-dynamics code CONVERGE [24] is used as solver for the simulation of the reacting turbulent transient flow. The chemical reactions are modeled using the code's detailed kinetics solver, called SAGE [66]. Given an accurate mechanism, SAGE can be used for modeling premixed and partially-premixed combustion regimes with the use of adaptive mesh refinement (AMR) to closely resolve gradients in volumetric reactions. On the basis of sufficient spatial resolution in the mixing region, the omission of a turbulence-chemistry interaction model may be justified, as also argued in many other studies [52, 67-69]. The detailed kinetic mechanism DRM19 is used [26], which consists of 19 reactive species (plus N_2 and Ar) and 84 elementary chemical reactions, with associated thermochemical properties. Comparing to the more detailed GRI 3.0 mechanism for methane [27], DRM19 shows 6-8% deviation for auto-ignition delay times and laminar flame speeds of mixtures at equivalence ratio of 0.2-2.0, initial pressure of 0.1-50 atm, and initial temperature of 1000-2500 K [28]. Even when utilized beyond the expected temperature range of validity, GRI-based mechanisms showed the best agreement with jet ignition experiments [29]. For more efficient computation, the SAGE solver uses multi-zone modeling, grouping cells in zones based on their thermodynamic state, with each zone treated as a closed-volume homogeneous reactor. In the current study, a three-variable multi-zone approach is employed which uses temperature, total equivalence ratio, and methane concentration to establish the zones with similar properties.

In the current work, a second-order accurate spatial discretization scheme is used to solve the governing conservation equations. The computational time step chosen to resolve the underlying physics varies between 10^{-8} to 10^{-7} seconds by employing a dynamic time scale algorithm that compares the flow and chemical time scales and selects the minimum. Numerical convergence is achieved by continuation of the iterative calculations within each time step in order to maintain the relative residual values of the momentum and energy/species conservation equations below 1%.

Numerical simulations are conducted using LES of a suddenly-starting turbulent jet at high Reynolds number of *Re*=113,000. The computational domain is adapted from the works of Kojok [60] and Chowdhury [61] in which a chamber, representative of a single channel of the wave rotor

combustor, is experimentally studied. Figure 2-2 shows the experimental rig employed with the details included in [60, 61]. Three PCB piezoelectric high-speed dynamic-pressure transducers, PT2, PT4 and PT3 are installed on the main chamber to register the pressure variations with 250 kHz sampling rate at near field, far field and end-wall cavity, respectively.

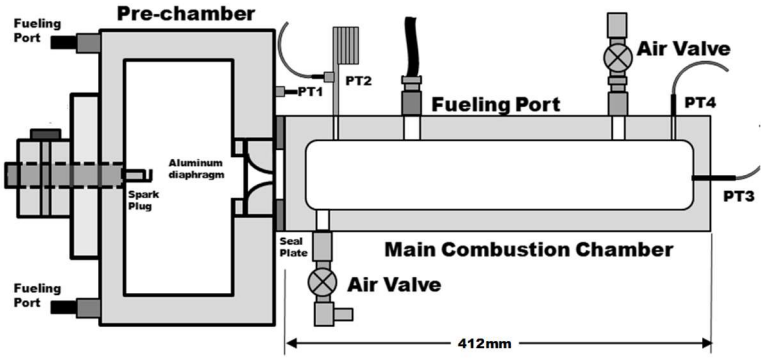

Figure 2-2: Schematic of the hot-jet ignition rig in the works of Kojok and Chowdhury.

The numerical domain opted for this study only encompasses the inner volume of the main chamber.

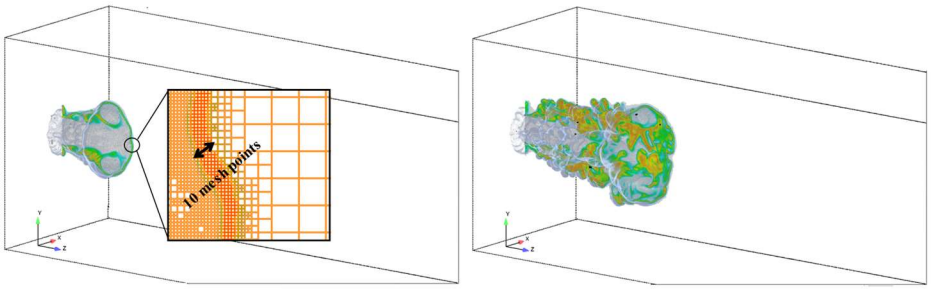

Figure 2-3: The numerical domain at t=0.15ms (left), and t=0.3ms (right) after start of injection. The iso-surface indicates the boundary of the jet with f=1% intersected by OH concentration plot. Adaptive mesh refinement is shown at the reaction zone.

In the numerical domain shown in Figure 2-3, an orifice with the inner diameter of D=6mm is stationed centrally on the left end-wall on a closed long squared-cuboid chamber. The side and length ratios of the constant-volume chamber are W/D=5 and L/D=50, respectively, with height and width equal. The chamber is initially filled with one of the two quiescent CH_4/H_2/air blends at standard pressure and elevated temperature T_0=500K prescribed in Table 1. A chemically reactive turbulent hot jet at T_j=2000K with top-hat velocity profile and the thermochemical composition described in Table 2-1 is suddenly issued through the orifice with turbulent fluctuation set at 2%

of the mean flow velocity. Based on the assumption that the jet is issued from a quiescent source through an orifice with relatively large diameter, the use of top-hat velocity profile with the prescribed turbulent fluctuation is justified. A block-structured base grid is used for the present LES, and in conjunction with AMR, the minimum cell size distribution provides neccessary resolution for capturing turbulent ignition fronts and adequate representation for pressure waves to model acoustic interactions. The interface between jet and surrounding gas is known to host the majority of ignition sites. AMR in the current study is intended to resolve this region adequately for capturing the ignition event.

Table 2-1: Thermo-physical composition of the hot jet and main chamber

Thermodynamic properties	Jet	CVC chamber 50:50% $CH_4 - H_2$	CVC chamber 30:70% $CH_4 - H_2$
Equivalence ratio	1.1 (equilibrium)	1	1
Temperature(K)	2000	500	500
Velocity/Pressure	360 m/s	1 atm	1 atm
Y_{N2}	0.72364	0.72872	0.73211
Y_{O2}	0.0026	0.22144	0.22252
Y_{H2}	0.00137	0.00553	0.01023
Y_{CH4}	0	0.04431	0.03514
Y_{OH}	0.0038	0	0
Y_{O}	0.00026	0	0
Y_{H2O}	0.14883	0	0
Y_{H}	0.0000786	0	0
Y_{CO2}	0.08641	0	0
Y_{CO}	0.02991	0	0
Y_{NO}	0.0031	0	0

Preliminary estimation of the critical ignition kernel size using William's ignition criterion [32] for the proposed fuel blend suggests a sphere of δ_f=0.1mm. Using three embedding levels of AMR, 8 to 10 computational cells are placed in the vulnerable ignition sites to ensure that the effect of turbulence on the kinetic rates at the flamelet size scale is recognized. The base-grid cell size of 0.5 mm is refined via AMR to generate cells size of 60 μm, with temperature differences within 2 K relative to the adjacent cells and velocity differences within 0.1% of the nozzle tip velocity. Similar cell size is employed in the work of Validi and Jaberi [52] and demonstrates good

resolution of turbulent flow structures. On the basis of scaling law, the present grid is able to resolve more than 85% of the turbulent kinetic energy according to a similar study by Nordin-Bates et al. [70]. The Kolmogrov length and time scale of the turbulent structure for similar prechamber-generated hot jet demonstrated by the DNS work of [51] and is shown to be 19 μm and 3.52×10^{-6} s, respectively.

The next section presents the grid sensitivity study and validity of the current work with respect to the flow and kinetics simulation.

2.4 Initial validation and verification

2.4.1 Non-reacting jet penetration

The mesh-independency of the solution is tested by assessing longitudinal development of the jet for various base-grid cell sizes. Figure 2-4 is a plot of the tip penetration of the non-reacting jet for three different base-grid cell sizes. It must be noted that the AMR embedding levels are kept consistent for all three base-grids. The jet growth rate is quite consistent among the three base-grids while the largest deviation of 3% is observed at 0.9 ms. Therefore, the base cell size of 0.5mm is selected for the present study.

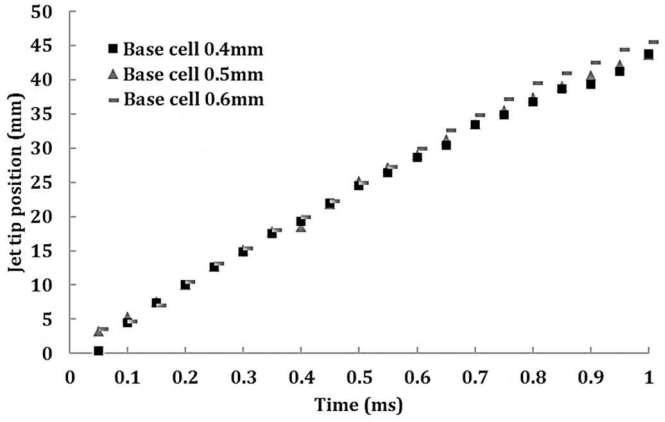

Figure 2-4: The non-reacting jet penetration distance with different base-grid resolution in the 3D LES (D=3mm, Re=19,000).

Kojok [60] used high-speed Schlieren imaging of a transparent acrylic channel to observe the radial and forward expansion of a non-reacting jet issued from a pre-chamber with stagnation temperature estimated at T_{stag}=1160 K. Figure 2-5 is a comparison of the non-reacting jet

penetration when issued from the pre-chamber at near-sonic speeds, between the current LES method and measurements by Kojok [60]. In the present LES, jet tip position on the centerline is designated by the location where the second derivative of the velocity magnitude is perturbed. The agreement between the non-reacting jet progress in the near and farfield is acceptable while the LES lacks accuracy possibly during the transitional stage from developing to the developed flowfield.

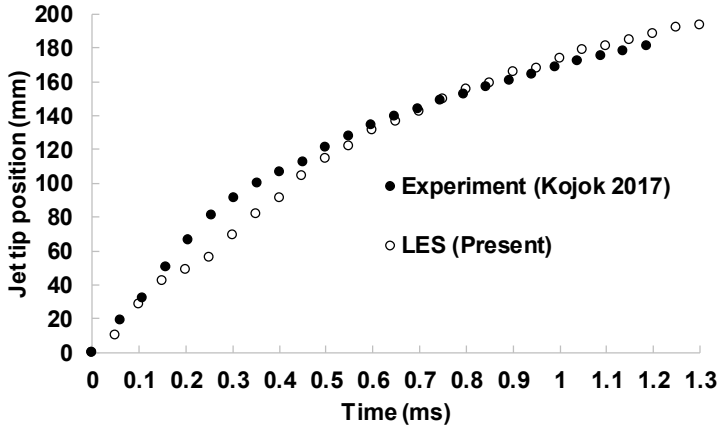

Figure 2-5: Comparison of the non-reacting jet tip penetration with the experimental work of Kojok (T_{stag} =1160K).

2.4.2 Kinetic mechanism and reacting-jet

Before investigating the chemically reacting jet, the validity of the detailed kinetic model employed in the current simulation (DRM19) is assessed against the shock-tube measurements of Zhang et al [19] by a zero-dimensional kinetic calculation using ChemkinPro [71]. The analysis is done on a mixture of CH_4, H_2, O_2, and Ar in an adiabatic constant-pressure reactor at the standard pressure. Methane–hydrogen blends in various molar ratios are studied reflecting the range of the fuel compositions used in the current LES. In Figure 2-6, the chemical ignition delay calculated by DRM19 is compared with the values measured in the shock-tube experiments. In general, the ignition delay at lower temperatures deviates from the shock tube experiments while the results converge at high temperatures. The ignition is more likely to emanate from the mixing region of the jet and ambient gas. The approximate temperature within the mixing region (T≈1250K) is highlighted in Figure 2-6 and the ignition delay determined by DRM19 shows promising prediction which proves the reliability of the employed chemistry kinetic model.

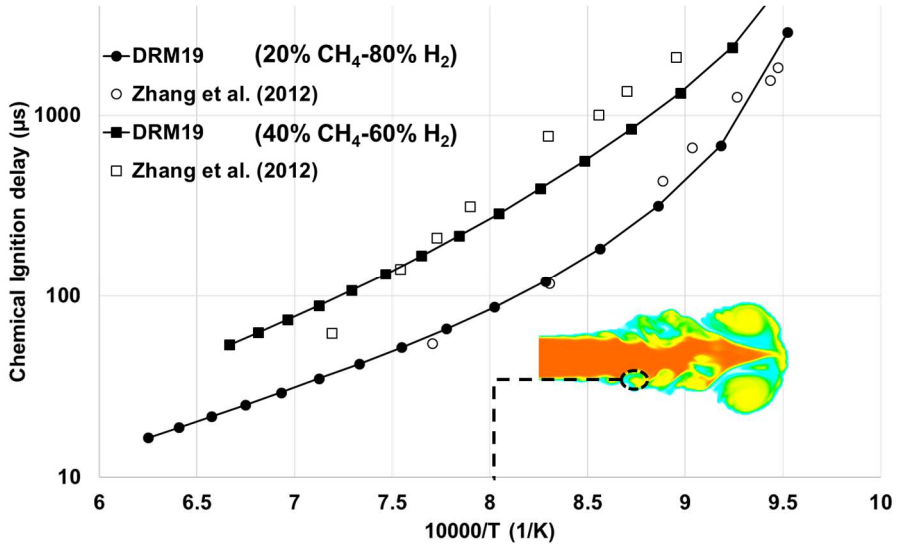

Figure 2-6: Zero-dimensional validation of the kinetic model for various CH4-H2 ratios (P=5 atm). Dashed line indicates the approximate temperature at the mixing region where ignition kernels typically emerge. Hollow markers: Shock-tube (Zhang et al.), and solid markers: DRM19.

In order to validate the current reacting LES, the hot jet ignition of 30-70% CH_4-H_2 is studied. In Figure 2-7, the experimental and simulated pressure histories registered by PT3 in the main chamber are shown, from the start of the hot jet injection. A sudden rise in pressure and a sudden emergence of hot zones in Schlieren images consistently indicate the moment of ignition due to the heat release in the confined volume. The simulation seems to capture the ignition moment with about 28% disagreement in delay time, which compared with the experimental measurement. This discrepancy may arise from disparities in the assumed nozzle jet temperature and turbulence profile imposed in LES, or inhomogeneity in the experimental main chamber mixture which is absent in LES. The events following ignition affect the pressure due to the formation and propagation of the flame front, acoustic wave phenomena in the chamber, and thermal losses from the main chamber. Since the primary focus of the current study is on the ignition event, the discrepancies in the post-ignition pressure history due to these effects are not addressed.

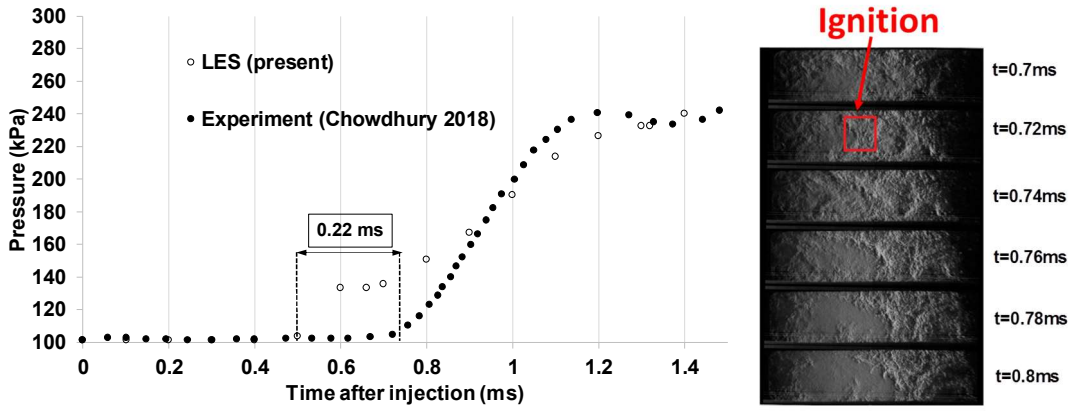

Figure 2-7: Main chamber pressure traces indicate a 0.22 ms difference in delay time between experiment and simulation. Experimental onset of ignition is also identifiable in Schlieren images. (30-70% CH_4-H_2)

2.5 Computed model features and discussion

Ignition by reactive hot jet involves significant physical mixing processes at small and large scales, each of which may create the possibility of ignition at various flow structures formed in the course of jet injection. The chemical reactions can commence in the presence of appropriate thermochemical composition and temperature as well as favorable scalar fields of mixture fraction, scalar dissipation rate and flow strain rate. In the present study, mixture fraction (f) is defined as the ratio of nozzle-originated species to the main chamber species, and square of the gradient of mixture fraction represents SDR. Also, a dimensionless time $\tau=t/10^{-4}$ is employed to describe the elapsed time after start of the jet injection. Figure 2-8 depicts the history of the jet evolution on the midplane crossing the nozzle and the main chamber. It is known that formaldehyde (CH_2O) is generally formed in lower flow residence time and is a reliable precursor to ignition, while OH distribution can reflect the high-temperature heat release [72, 73]. The visuals in Figure 2-8 show spatial distribution of mixture fraction overlaid by the iso-curves of formaldehyde ($Y_{CH2O}= 8.8\times10^{-4}$) as the indicator of the ignition formation, and squared gradient of mixture fraction, $(\nabla f)^2$. One goal of this study is to elaborate the time and possibly the location at which the ignition kernels originate. It can be observed from Figure 2-8 that the initial ignition kernels emerge from the mixing layer on the jet trailing length and are partially transported to, or generated at the growing head vortex ($2.5< \tau <3.5$). Comparison between the domains of mixture fraction and scalar dissipation rate suggests that the primary ignition sites are hosted by mixing regions with minimal

scalar dissipation rate. Suppression of ignition or quenching of the flamelets could be a consequence of high scalar dissipation rate which can disturb the balance between heat generation and dissipation in the mixing zone [74]. Similar observation have also been widely reported by reacting turbulent jet studies [56, 75].

The increasing population of formaldehyde iso-curves in the leading head vortex during τ=5.5-6.5 implies the progress of the volumetric heat-releasing reactions in a region with favorable thermochemical composition and sufficient residence time due to the flow circulation. The sudden transition of formaldehyde distribution between τ=6.5 to 7.5 may be attributed to the fact that the volumetric auto-ignition, which was initiated in the vortex, is now giving rise to the flame development and subsequent propagation of the flame front at the periphery of the jet. However, more detailed study on the energy budget of diffusive heat transport and heat generation must be applied in order to clearly identify the contribution of auto-ignition versus premixed flame propagation on the overall heat release development.

A comparison between ignition developments for the two fuel blends is provided in Figure 2-9. The plots show the distribution of temperature and hydroperoxyl (HO_2) concentration overlaid by iso-curves of formaldehyde ($Y_{CH2O}=8.8\times10^{-4}$) which indicates the ignition onset. Interesting features of the structure of the jet and flame include the development of various zones seen in Figure 2-9; i.e. hot jet (upstream of the flame), burned-mixed zone (Y_{CH2O} iso-curve), and flame front in the jet periphery (Y_{HO2} boundary). These zonal boundaries are relevant to the findings of Validi et al. [52]. Although in the work of Validi et al. the hot jet is stationed in a co-flow, the same active combustion zones are identifiable in the stable flame structure of the present study in the absence of a co-flow. The differences between the two fuel mixtures include faster advent of ignition precursor (formaldehyde) in the 30-70% fuel mixture with higher hydrogen content during $0.5<\tau<1.5$, compared to $1.5<\tau<2.5$ in the 50-50% fuel mixture with lower hydrogen content. The locality of the ignition initiation has similarities and differences between the two fuel types in terms of formation and transportation of the ignition kernels in the streamwise direction. It is noticeable that the population of $Y_{CH2O}=8.8\times10^{-4}$ is more abundant and distributed in 50-50% fuel blend throughout a region of moderate mixture fraction, whereas this iso-curve remains near the jet periphery for the 30-70% blend. Based on the spatial distribution of HO_2 and growth rate of the reaction zone, it is perceived that the fuel with higher hydrogen content experiences an earlier transition from ignition to flame propagation (τ~2.5 for 30-70% versus τ~6.5 for 50-50%). It

perhaps implies that the contribution of volumetric auto-ignition to the overall heat release is less significant for higher hydrogen content due to the shorter ignition delay.

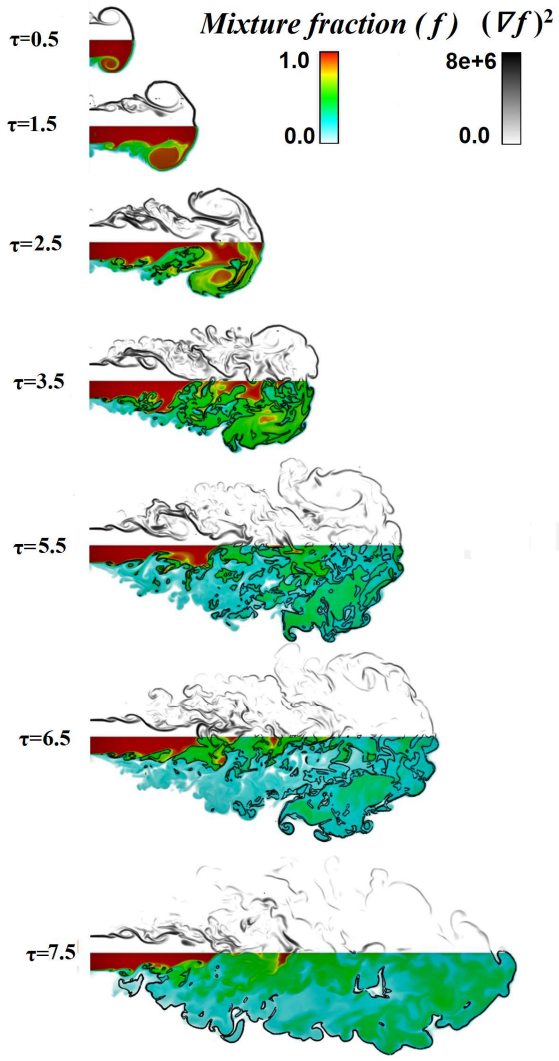

Figure 2-8: Square of the mixture fraction gradient (upper half) as an indicator for the scalar dissipation rate, and mixture fraction (lower half) during the transient jet injection. (50-50% CH_4-H_2) Black iso-curves indicate locations where $Y_{CH2O}=8.8\times10^{-3}$

The hypothesis of varying role of auto-ignition and premixed flame propagation to the overall heat liberation could be more elaborated by monitoring the heat release rate (HRR), and OH mass fraction over time. As seen in Figure 2-10, rate of heat release for 50-50% fuel mixture experiences an abrupt jump at about τ=6.5 where the majority of the individual kernels seem to merge and give rise to a sudden heat generation. A concurrent transition is observed in the

accumulation of OH in the 50-50% fuel blend. There are multiple ways this could be understood and perhaps all contribute. The kernels may appear to grow as more nearby regions achieve autoignition; the kernels may individually grow by local flame propagation; and the kernels may be transported towards each other or towards the same location.

Abrupt changes in HRR and OH are not distinctly observed in the ignition process of 30-70% fuel blend. The aforementioned trends of HRR are supportive of the idea that auto-ignition is more dominant in the fuel mixtures where mixing and chemical time scales are closer, i.e. 50-50% blend. While for the more reactive fuel, i.e. 30-70%, the majority of heat release is carried out by premixed flame propagation, after early achievement of localized autoignition.

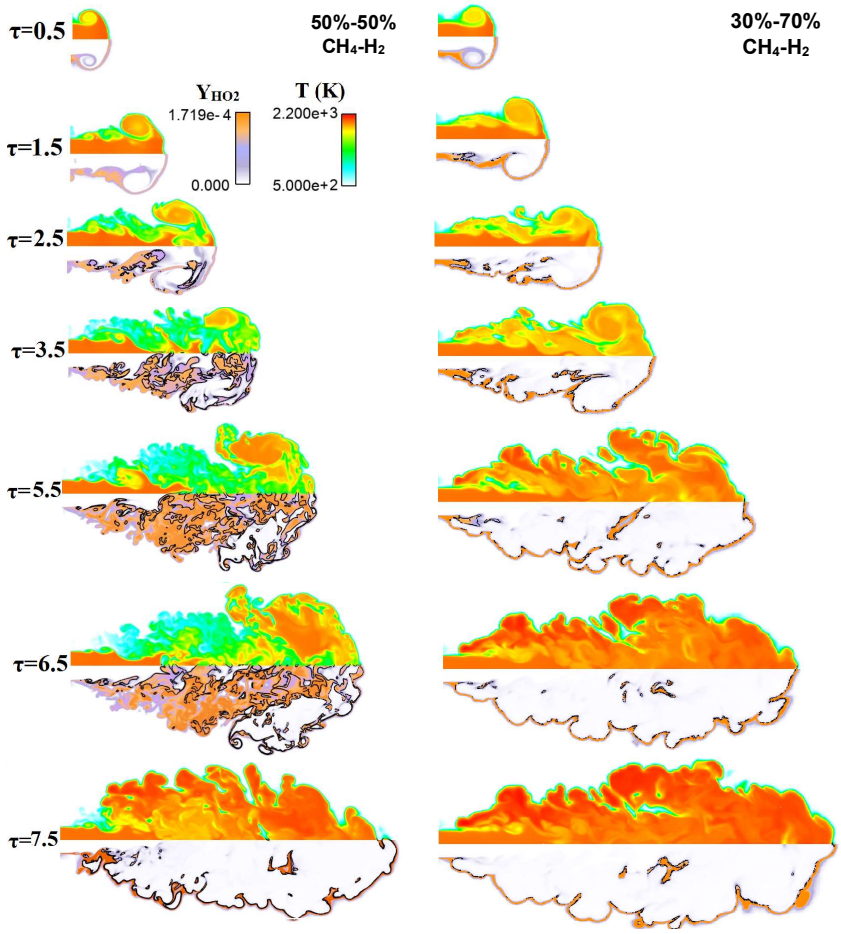

Figure 2-9: History of temperature (upper half) and HO_2 distribution (lower half). Black iso-curves superimposed on the lower half indicate locations where $Y_{CH2O}=8.8\times10^{-3}$

The time evolution of the chemical states of the jet particles can be studied by means of scatter plot presented in Figure 2-11. Here the progress variable (obtained from the partially-

premixed model) is used to demonstrate the changes of temperature and fuel fraction due to chemical reactions. Progress variable is 0.0 for an unburnt gas and 1.0 for the burnt state that is at equilibrium. Adapted from the work of Bray et al. [76], progress variable (c) is defined by linear expression in terms of the fuel mass fraction (Y_F),

$$c(\vec{x},t) = \frac{Y_{F0}(1-f(\vec{x},t))-Y_F(\vec{x},t)}{Y_{F0}(1-f(\vec{x},t))-Y_F^{Eq}[f(\vec{x},t)]} \quad \text{Eq. 2-12}$$

where Y_{F0} is the fuel mass fraction in the far-field, $f(\vec{x},t)$ is the mixture fraction at the arbitrary location ($\vec{x}$), and Y_F^{Eq} is the equilibrium fuel mass fraction at a given mixture fraction $f(\vec{x},t)$. Figure 2-11 shows the scatter plot of the ignition process for 50-50% fuel blend as the transition occurs from auto-ignition to flame formation. The scatter plots are extracted from the rectangular midplane and colored by the correlation Y_{OH}*Y_{CH2O} which may well represent the heat release rate due to the ignition [51]. As seen in Figure 2-11, majority of the ignition heat release occurs around c=0.8, which can be insightful in statistical studies where the ignition zone is targeted. This observation agrees with findings of Ghorbani et al. [54].

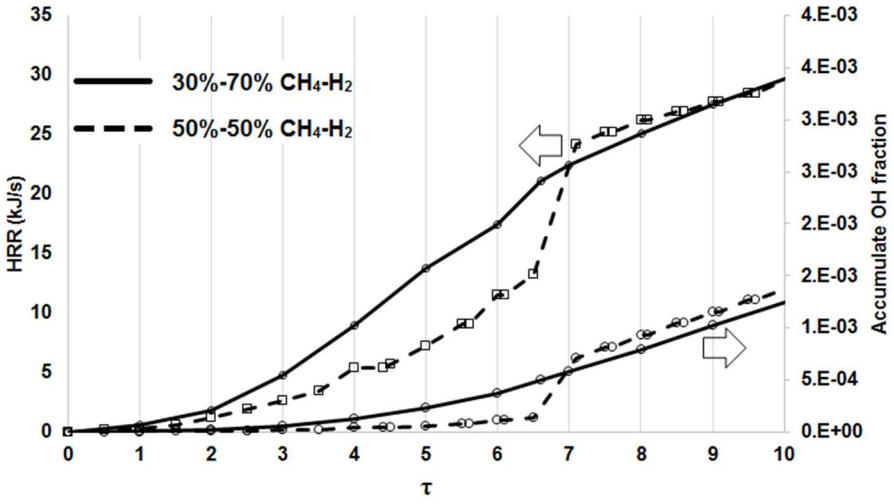

Figure 2-10: History of heat release rate and accumulative OH as a function of dimensionless time.

One may observe that at τ=6.5, the chemical state of the jet particles are relatively more scattered around the mean over the wide range of progress variable ($0.1 < c < 0.8$) which implies that the different degrees of the reaction are occurring in a various mixture fractions. However, at the next time instance (τ=7.5), the chemical state of the jet is more oriented around the mean as

the isolated auto-ignition kernels merge and give rise to the formation of the propagating premixed flame. Comprehensively, from this observation one can state that the fuel reactivity plays a significant role in the ignition dynamics in terms of contribution of auto-ignition to the overall heat release.

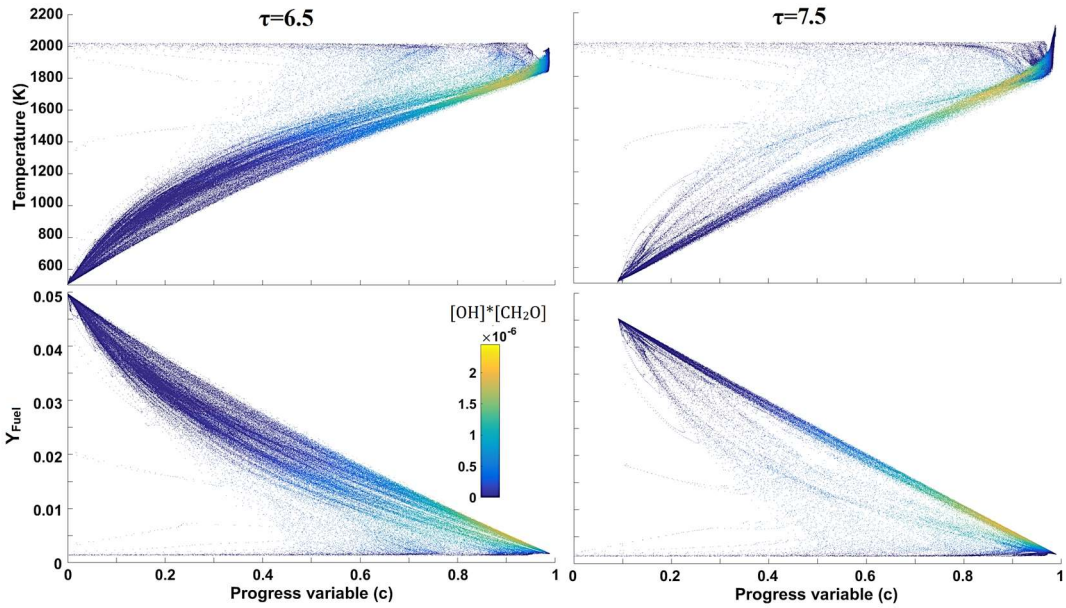

Figure 2-11: Scatter plots of the instantaneous temperature and fuel fraction at the main chamber versus the progress variable. (50-50% CH_4-H_2)

2.6 Conclusion

This work reports on LES investigation of the transient turbulent jet ignition occurring in a combustor with fixed volume filled with stoichiometric H_2-CH_4-Air mixture of two fuel blends. High-resolution, adaptively refined mesh in combination with detailed chemical kinetics allowed simulation of the thermofluidic and chemical processes involved in the emergence of ignition in small and large scales. Distribution of the intermediate species such as CH_2O and OH examined alongside with the mixture fraction and the square of its gradient indicates that the regions with minimal scalar dissipation rate are most susceptible to host the ignition. The sequential assessment of the scalar fields suggests the formation of ignition kernels within the trailing shear layer of the jet as well as the head vortex. While the ignition of fuel blend with lower reactivity may benefit from abundant mixing rate and residence time in the jet periphery, the fuel with higher reactivity showed reliance on small-scale diffusive mixing in order to achieve ignition. Moreover, there is

evidence of transportation of ignition sites, which are originally formed in the trailing shear layer, to the head vortex where the kernels agglomerate. As the trends of the heat release rate and accumulated OH concentration indicates, ignition starts faster for fuel with higher hydrogen content. However, the development of ignition sites is quite different between the two fuel blends. It is noteworthy that for 50-50% CH_4-H_2 blend, the isolated ignition kernels quickly grow and merge in a rapid heat releasing process between τ=6.5 to 7.5 and form the propagating premixed flame. Whereas, for 30-70% CH_4-H_2 blend, this transition from volumetric auto-ignition to propagating flame formation is barely noticeable.

Evaluating the scatter plot for the chemical state of the jet particles for 50-50% CH_4-H_2 blend at τ=6.5, affirms the wide dispersion of the scalars around the mean at a given progress variable. Therefore, it supports the idea that combination of isolated ignition kernels can eventually produce a rapid heat release followed by the formation of propagating premixed flame. Analysis that is more rigorous may be required to quantify the role of auto-ignition in terms of its energy budget of the total heat release. For the studied fuel blends, the value of the product Y_{OH}*Y_{CH2O} which is well correlated with ignition, is maximized at the progress variable c=0.8. This observation provides insights for future statistical analysis of the hot jet ignition in order to accurately predict the mixing regions that are prone to ignition.

2.7 Acknowledgment

We thank Mr. Ali Tarraf Kojok, who provided experimental data, and Mr. Arshad Zahangir Chowdhury, who provided insight and expertise that greatly assisted the research. This work was partially supported by the US National Science Foundation under Grant No. CBET-1235696, and by a fellowship from the Purdue School of Engineering & Technology.

3. SCALAR PREDICTORS OF PREMIXED GAS IGNITION BY A SUDDENLY-STARTING HOT JET

Acknowledgment: This is a post-peer-review, pre-copyedit version of an article published in International Journal of Hydrogen Energy. The final authenticated version is available online at: https://doi.org/10.1016/j.ijhydene.2019.07.066

3.1 Abstract

Hot-jet ignition is usually designed to reduce emissions in lean-burn combustion engines, and has potential in enabling novel pressure-gain combustion. Inspired by our experimental observations related to wave-rotor combustion chamber ignition, this work employs a numerical method to examine the sudden injection of a hot jet into a quiescent mixture of CH4-H2-air and the subsequent ignition. The goal is to provide the range of thermo-physical scalars that are supportive of successful ignition. The evolution of scalar fields is evaluated using large-eddy simulation (LES). The temporal evolution of mixture fraction, the squared gradient of mixture fraction (as indicative of scalar dissipation rate), strain rate, and intermediate species are investigated in order to find the appropriate physical conditions which support ignition. Independent distribution of stain rate and squared gradient of mixture fraction, especially in the leading head vortex, shows the necessity of correlated scalar analysis of the ignition process. Experimental and numerical methods are then employed to provide the qualitative and quantitative understanding of ignition process for fuels with two distinct hydrogen contents. Results show the meaningful difference in spatial distribution of local ignition as hydrogen content of the fuel increases.

Keywords: Transient jet, hot jet ignition, large eddy simulation.

3.2 Introduction

The initiation of combustion in premixed gas by injection of hot gas as means of ignition is important in various applications such as internal combustion (IC) engines, pressure-gain combustors, and explosion and fire safety. Turbulent jet ignition (TJI) has been employed by ultra-lean burn low-emission combustion engines as a reliable method of ignition [6, 77]. In IC engines,

the jet is issued into a main combustion chamber from a small adjacent pre-combustion chamber, which is typically fuel-rich and spark-ignited. In a wave-rotor pressure-gain combustor, the jet arises from a momentary connection of a chamber with unreacted-mixture to an identical chamber with combusted gas. High-temperature products of pre-chamber combustion are suddenly injected through a small orifice into the main chamber, which contains premixed reactants [47] and thus receives distributed sources of ignition. Depending on pre-chamber design and mixture, pressure history, and the method of connection, the jet may comprise fully or partially combusted species, and may be stationary or traversing. The combustion is initiated as a result of the mixing process in small and large scales with the enhancing effect of chemically-active radicals that reside in the emerging jet.

The suddenly-starting jet exhibits intricate spatial and temporal structures, which depend on the design. In IC engines, the permanent connection between the pre-chamber and main chamber will result in a more gradual start and varying jet composition. In a wave-rotor, the relative motion between the gas transfer passage and the combustion chambers result in a traversing jet that suddenly connects and then disconnects [23, 78]. This work considers only an instantaneously started jet that is stationary with respect to the main chamber. The leading head vortex and the trailing shear layer of the starting jet both participate in the mixing process through large engulfment and entrainment of the flow, and through turbulent diffusion [4]. Andriani et al. [79] and Kato et al. [80] showed that a starting jet has a higher mixing rate than steady jets due to the enhanced mixing by the leading vortex, while Shahsavan et al. [81] showed, using a mixture of noble gases and oxygen, that jet density greatly affects mixing development and subsequent ignition behavior. Due to the complexity of the underlying chemical and physical processes, prediction of TJI remains challenging. High-fidelity simulation and experimental studies have been conducted to understand the TJI mechanism for a successful ignition in the engine-relevant conditions [1, 8, 16, 43, 82, 83]. Several studies have examined the contribution of mixing and chemical timescales to the formation of ignition sites in the periphery of the turbulent jet [31, 84, 85]. A critical global Damköhler number of 140 for methane-air and 40 for hydrogen-air combustion was proposed by Biswas et al, [84] which is generally considered the limiting parameter that separated ignition and no-ignition zones. Validi et al. [52] carried out a fundamental numerical study of steady jet of hot gas interacting with a co-flow of lean premixed hydrogen-air. They spatially divided the reaction region into three main zones, namely hot product jet, burned-

mixed, and the flame zone, and examined the flame and turbulence structures of these zones. In the direct numerical simulation by Qin et al. [51], it was demonstrated that the jet contribution to ignition occurs via three major pathways, i.e. chemical, thermal and fuel enrichment which are all governed by the combustion properties in pre-chamber. Wang et al. [86] identified a critical Damkohler number to distinguish the three observed reaction regions of hydrogen-air mixture by transient hot jet ignition: namely, extinction region, just-igniting region, and combustion region.

The hydrodynamic behavior of transient jets in a reacting environment has been studied in the literature [25, 31, 87, 88]. However, the behavior of scalar fields in the development of hot jet ignition must also be investigated to enable the robust design of igniters. Soloupolus et al., [58] studied the scalar dissipation rate (SDR) of a non-reacting impulsively started gas jet, in which it was realized that high values of SDR are concentrated at the jet boundary. A highly resolved LES of a transient non-reacting jet was conducted by Inanc et al. [53], and mixture fraction and its dissipation rate were statistically examined. The computed dissipation rate exhibits a Gaussian probability distribution, consistent with the literature [89, 90]. The statistical behavior of SDR in the context of LES or DNS of turbulent combustion has been widely studied to develop robust combustion models [91, 92]. In the work of Arndt et al. [56], the transient injection of methane into a laminar hot vitiated co-flow and its subsequent ignition were studied to examine the role of temperature, mixture fraction and SDR. It was found that auto-ignition occurred after the jet evolves from transient into the steady state and the kernels are located at very lean mixture fractions with low SDR. Fischer et al. [85], numerically investigated the initiation of explosion in a propane-air mixture via injection of hot exhaust and found out that the highest rate of the progress variable occurs at the subsequent flame propagation and not by the mixing process. They indicated that the ignition near the tip of the jet results in a rapid jump in progress variable at jet-origin mixture fraction around 0.1. Ghorbani et al. [54] showed that ignition in the leading vortex of a hot jet takes place at relatively high mixture fractions and progress variable c=0.8, while the location of ignition in mixture fraction space approaches towards lower mixture fractions as the flame is developing. Experimental and numerical investigation of Xu et al. [93] demonstrated the various roles of transient jet vortex and shear layer in promoting the reaction due their differences in turbulence intensities.

For applications that require rapid burning rate of lean mixtures, such as low-emission internal combustion engines, the ignition success may depend on establishing appropriate scalar

statistics. In particular, for high-speed jets, the mixing and chemical time scales are often comparable. Therefore, the interaction between chemical time scales and micromixing (molecular mixing) as well as macromixing (turbulent entrainment) becomes critical for the overall ignition prediction. This has motivated the current study, which aims to develop understanding of the turbulent hot jet ignition process by examining the correlation between mixture fraction, squared gradient of mixture fraction and flow strain rate, as well as the temperature and chemical composition fields. The goal is to establish the range of scalar values by which local ignition is caused by a suddenly-started hot jet. Prompted by experimental observations, this study also seeks to computationally analyze the effect of fuel reactivity on the locality of ignition in CH_4-H_2-air mixtures at two distinct CH_4-H_2 blend ratios. The present investigation attempts to shed light on the temporal development of scalars leading to ignition, the results of which may be used to design the flowfield for lean-burn IC engines and for wave-rotor combustors.

3.3 Experimental and numerical methods

In the present investigation, hot jet ignition is studied using experimental and large-eddy simulation methods. The experimental measurements of TJI assists us to identify the global ignition timing and to set up the numerical simulations to utilize available computational resources effectively. The numerical modeling is employed to evaluate the scalar fields and thermochemical composition of the mixing zones upon ignition occurrence.

3.3.1 Experimental rig

The experimental rig is made up of two combustion chambers, a rotatable cylindrical pre-chamber with diameter of 165.5 mm and internal cavity volume of 0.68 liters and a long square cuboidal main combustion chamber of 36×47×355 mm^3 containing the main reactant mixture (Figure 3-1). The pre-chamber is made of stainless steel with a spark plug at the center. It is filled with a premixed fuel-air mixture at equivalence ratio of 1.1, and separated from the main chamber by a 0.003 inch 1010 aluminum diaphragm. Although the rig is designed for providing a traversing jet in the fashion of a wave-rotor combustor, through rotation of the pre-chamber, the present study is limited to the case of a stationary jet that is centered at the mid-point of one end wall of the main chamber, with a tight seal.

The spark-ignited pre-chamber mixture ruptures the diaphragm and drives a hot reactive jet into one end of the main chamber through a converging nozzle with 6mm exit diameter and 10˚ taper. Careful scoring promotes symmetric diaphragm rupture symmetric to ensure essentially axisymmetric flow-field of the hot reactive jet. The main chamber is mounted on an X-Y positioning table to control the alignment of the chamber with the issued jet. The effective ratio of internal cavity volume of the pre-chamber to the main combustion chamber is approximated to be 1.14, which results in maintaining a critical pressure difference across the nozzle during the course of combustion. The main combustion chamber has six ports for instrumentation and measurement. Three PCB piezoelectric high-speed dynamic pressure transducers, PT2, PT3, and PT4 are installed on the main chamber to record transient pressure variation inside the main chamber at jet near-field, jet far-field and at far end-wall, respectively. The pre-chamber pressure variation is recorded by the pressure transducer PT1. The pressure transducers sample at approximately 250 kHz. The other three ports in the main combustion chamber serve as fueling port and air inlet and outlets. MKS model PFC-60 mass flow controller, calibrated in-house, delivers fuel to the main combustion chamber through the fueling port. Zhang et al. [94] reported meaningful change in ignition chemistry as hydrogen content of the mixture exceeds 60%. Based on that observation, batches of 50%-50% methane-hydrogen and 30%-70% methane-hydrogen (volumetric) are prepared for this investigation. The fueling of pre-chamber is based on partial pressure calculation with 50%-50% methane-hydrogen fuel through the pipe and tube fittings and quick connects. A Z-type Schlieren arrangement with parabolic mirrors, point light source, knife edge, and a high-speed Phantom V9 high-speed camera captures Schlieren images at approximately 18,000 frames per second. The recorded Schlieren images are analyzed to estimate timings of rupture moment, moment of jet injection to the chamber, and onset of ignition. A National Instrument data acquisition system synchronizes the camera and the pressure transducers with the triggering of the spark plug inside the pre-chamber. Details regarding data acquisition and processsing are elaborated by Kojok [60, 61]. To ensure the repeatability of jet experiments, pressure traces of 9 stoichiometric mixtures ignited by hot jet are compared. The uncertainty in igntion delay time is estimated at about 15%, factoring in the effect of pre-chamber fueling, main chamber fueling, and diaphragm rupture moment.

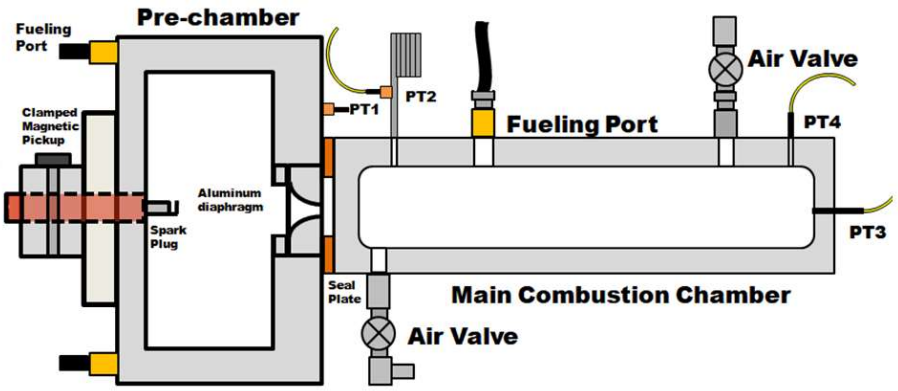

Figure 3-1: Schematic of the pre-chamber and main chamber integrated assembly.

3.3.2 Numerical domain and governing equations

Ignition of CH_4-H_2-air mixture by a hot starting-jet with the composition prescribed in Table 3-1 is numerically simulated using LES. Stoichiometric blends are numerically simulated due to their inherently short ignition delay which reduces computational time. The jet composition is assumed to be the equilibrium products of 50%-50% methane-hydrogen at equivalence ratio 1.1. The jet tip velocity is set based on high-speed imaging of the jet from experimental measurements. Due to the difficulty of accurate experimental measurement of the jet thermal and chemical properties, the jet temperature in the simulations is selected so that the global computed ignition moment matches approximately with the experimental observations. [2, 95].

Table 3-1: Thermo-physical composition of the hot jet and main chamber fuel mixture.

Thermodynamic properties	**Jet**	**Main chamber 50%:50% $CH_4 - H_2$**	**Main chamber 30%:70% $CH_4 - H_2$**
Equivalence ratio	1.1 (equilibrium)	1	1
Temperature(K)	2000	500	500
Velocity/Pressure	360 m/s	1 atm	1 atm
Y_{N2}	0.72364	0.72872	0.73211
Y_{O2}	0.0026	0.22144	0.22252
Y_{H2}	0.00137	0.00553	0.01023
Y_{CH4}	0	0.04431	0.03514
Y_{OH}	0.0038	0	0
Y_{O}	0.00026	0	0
Y_{H2O}	0.14883	0	0
Y_{H}	0.0000786	0	0
Y_{CO2}	0.08641	0	0
Y_{CO}	0.02991	0	0
Y_{NO}	0.0031	0	0

In the numerical domain (Figure 3-2) an orifice with the inner diameter of D=6mm is stationed centrally on the left end-wall on a closed long square-cuboid chamber from which the jet with Reynolds number of Re=113,000 (360 m/s) is suddenly issued.

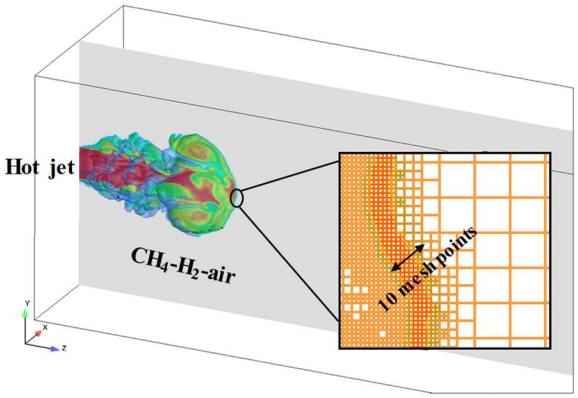

Figure 3-2: The numerical domain at t=0.25ms after start of injection. The colors indicate mixture fraction and the blue iso-surface is defined at mixture fraction 0.1. Adaptive mesh refinement is shown (shown in the box, 10 mesh points resolve the reaction zone colored by H atom mass fraction).

The side and length ratios of the constant-volume chamber with square cross section are W/D=5 and L/D=50, respectively. The boundary condition of the orifice has top-hat velocity profile with 2% turbulent fluctuation of the mean flow velocity that may represent the event of

diaphragm rupture in the experiment. A block-structured base grid with 0.5mm base cell sizes is used for the present LES. In conjunction with adaptive mesh refinement (AMR), the minimum cell size distribution of 60 μm (approximately 80M total cells) can sufficiently resolve the turbulent flame front and represent the pressure waves to model acoustic interactions with combustion [96]. In the work of Validi and Jaberi [52] similar cell size is employed and good resolution of the turbulent flame structures were obtained. On the basis of scaling law, the present grid is able to resolve more than 85% of the turbulent kinetic energy according to a similar study by Nordin-Bates et al. [70]. Figure 3-3 shows the measured energy spectra for the current starting jet, which indicates the satisfactory resolution of the turbulent kinetic energy beyond 85%. Based on DNS studies of similar jets [51, 97], Kolmogrov length and time scale of the turbulent structure to be 10 μm and 3.52×10^{-6} s, respectively. In addition to the above turbulent kinetic energy analysis, we also looked at the kernel size which is found to be 0.1 mm as per the William's criterion [32] and our present minimum cell size is 40% less than the kernel size.

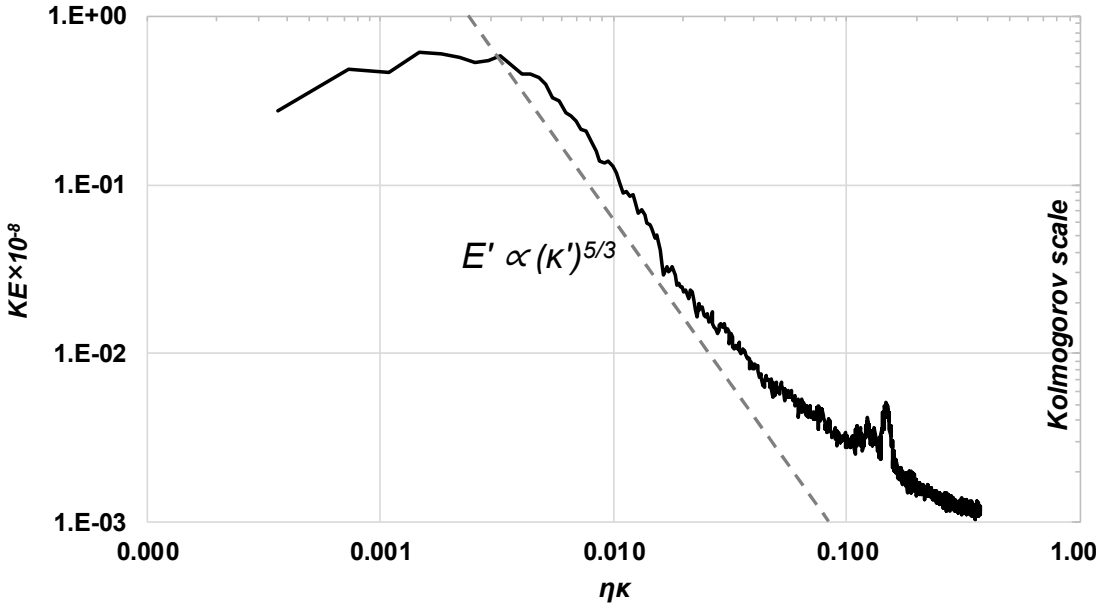

Figure 3-3: Normalized turbulent kinetic energy spectra measured at (x=0, y=3mm, z=6mm). At ηκ=1, the wavenumber is associated with the Kolmogorov scale. As a reference, the -5/3 decay line has been plotted in dashed grey line.

The computational fluid dynamics code CONVERGE version 2.4 [24] has been used for modeling of the reacting turbulent flow. Detailed kinetics of the reacting flow is modeled using the SAGE solver. With appropriate spatial resolution, SAGE does not limit the species to a low-dimensional manifold, allowing broader applicability to combustion regimes such as ignition and

extinction [66]. As most popular flamelet approaches are not capable of capturing volumetric ignition, the present work employs finite-rate chemistry with well stirred reactor model for combustion closure. If the grid resolution is sufficiently close to Kolmogorov scale (as reflected by turbulence energy spectra in Figure 3-3), finite-rate chemistry in the absence of any turbulence-chemistry interaction is considered an appropriate LES modelling assumption [98-101]. The reduced reaction mechanism DRM19 is used [26], comprising 19 reactive species (plus N_2 and Ar) and 84 elementary chemical reactions. The detailed kinetic employed shows 6-8% deviation for ignition delay times and laminar flame speeds of mixtures at equivalence ratio of 0.2-2.0, initial pressure of 0.1-50 atm, and initial temperature range of 1000-2500 K [27, 28]. Second-order schemes were used for spatial discretization associated with a dynamic timescale algorithm that sets time step varying between 10^{-8} to 10^{-7} seconds.

The transport equations are discretized and solved using PISO of Issa [33]. In this LES, the Favre-averaged form of the continuity and momentum equations are solved [62],

$$\frac{\partial \bar{\rho}}{\partial t} + \frac{\partial \bar{\rho}\tilde{u}_j}{\partial x_j} = 0, \qquad \text{Eq. 3-1}$$

$$\frac{\partial \bar{\rho}\,\tilde{u}_i}{\partial t} + \frac{\partial \bar{\rho}\tilde{u}_i\tilde{u}_j}{\partial x_j} = -\frac{\partial \bar{P}}{\partial x_i} + \frac{\partial \bar{\sigma}_{ij}}{\partial x_j} - \frac{\partial \tau_{ij}}{\partial x_j} \qquad \text{Eq. 3-2}$$

where u_i, ρ, P and σ_{ij} represent velocity, density, pressure, and the stress tensor, respectively. σ_{ij} is defined as follows;

$$\sigma_{ij} = \mu\left(\frac{\partial \tilde{u}_i}{\partial x_j} + \frac{\partial \tilde{u}_j}{\partial x_i}\right) + \left(\mu' - \frac{2}{3}\mu\right)\left(\frac{\partial \tilde{u}_k}{\partial x_k}\delta_{ij}\right) \qquad \text{Eq. 3-3}$$

The small-scale structures are accounted for via a subgrid-scale (SGS) stress term,

$$\tau_{ij} = \bar{\rho}\left(\widetilde{u_i u_j} - \tilde{u}_i\tilde{u}_j\right). \qquad \text{Eq. 3-4}$$

Due to the complication of unresolved velocity correlations, the SGS is calculated using the dynamic structure [63, 64] model to approximate stress tensor at the SGS level via a sub-grid kinetic energy equation,

$$\frac{\partial \bar{\rho}\,k}{\partial t} + \frac{\partial \bar{\rho}\tilde{u}_j k}{\partial x_j} = \frac{\partial}{\partial x_j}\left(\frac{\mu}{Pr_{SGS}}\frac{\partial k}{\partial x_j}\right) + \tau_{ij}\bar{S}_{ij} - \rho\epsilon\ , \qquad \text{Eq. 3-5}$$

The SGS stress tensor (τ_{ij}) is thus modeled by

$$\tau_{ij} = 2k\bar{\rho}\frac{L_{ij}}{L_{kk}}, \qquad \text{Eq. 3-6}$$

where the Leonard stress tensor is defined as $L_{ij} = \widehat{\tilde{u}_i}\widehat{\tilde{u}_j} - \widehat{\tilde{u}_i}\widehat{\tilde{u}_j}$, and "$\widehat{\ }$" symbol indicates the test-level filter which is being resolved. The Favre filtered species and energy conservation equations are established as follows:

Species conservation:

$$\frac{\partial \bar{\rho}\,\tilde{Y}_n}{\partial t} + \frac{\partial \bar{\rho}\,\tilde{u}_j\,\tilde{Y}_n}{\partial t} = \frac{\partial}{\partial x_j}\left(\bar{\rho}(D + D_t)\frac{\partial \tilde{Y}_n}{\partial x_j}\right) + \bar{\dot{\omega}}_n\,, \qquad n = 1,2,3,\ldots\ldots,m \qquad \text{Eq. 3-7}$$

Energy conservation:

$$\frac{\partial \bar{\rho}\,\tilde{e}}{\partial t} + \frac{\partial \bar{\rho}\,\tilde{u}_j\,\tilde{e}}{\partial t} = -\bar{P}\frac{\partial \tilde{u}_j}{\partial x_j} + \bar{\sigma}_{ij}\frac{\partial \tilde{u}_i}{\partial x_j} + \frac{\partial}{\partial x_j}\left(K_t\frac{\partial \tilde{T}}{\partial x_j}\right) + \frac{\partial}{\partial x_j}\left(\bar{\rho}(D + D_t)\sum_{n=1:m}\widetilde{h_m}\frac{\partial \widetilde{Y_m}}{\partial x_j}\right) + S^e \qquad \text{Eq. 3-8}$$

In Eq. 3-7 and Eq. 3-8 , Y_n is the mass fraction of species *n*, ρ is density, $\bar{\dot{\omega}}_n$ is the reaction source term, *e* is the specific internal energy, *D* is molecular diffusivity, and D_t is turbulent diffusivity. The eddy viscosity approximation at sub-grid level is employed for the scalar transport equations for which, D_t is given by Eq. 3-9 as recommended in [65]

$$D_t = \frac{C_k \Delta k^{0.5}}{Sc} \qquad \text{Eq. 3-9}$$

where the model constant is set to 0.5 and the turbulent Schmidt number, set to 0.699 in the present simulations. Schmidt number is estimated based on the prevalent mass average values of species in the reaction zone [102]. The turbulent conductivity in the energy equation is estimated as $K_t = c_p\frac{\mu_t}{Pr_t}$, where μ_t, Pr_t, and c_p is turbulent viscosity, turbulent Prandtl number, and specific heat, respectively.

Mesh independency of the solution is discussed in the work of Feyz et al. [95] by testing the effect of various base-grid cell sizes on the penetration length of the jet. Figure 3-4 presents the penetration length of the jet tip for a non-reacting jet issued from the pre-chamber and compares the LES with experimental observations. The jet tip position on the centerline is designated by the location where the second derivative of the velocity magnitude is perturbed. It may be noted that the current LES model captures the formation of the leading vortex, as well as small-scale structures and shear layer instabilities, which are related to the decay of the penetration rate. However, it must be considered that some assumed parameters, specifically the jet temperature

and velocity, may deviate from the experimental case due to the heat loss and pressure drop of the pre-chamber and nozzle.

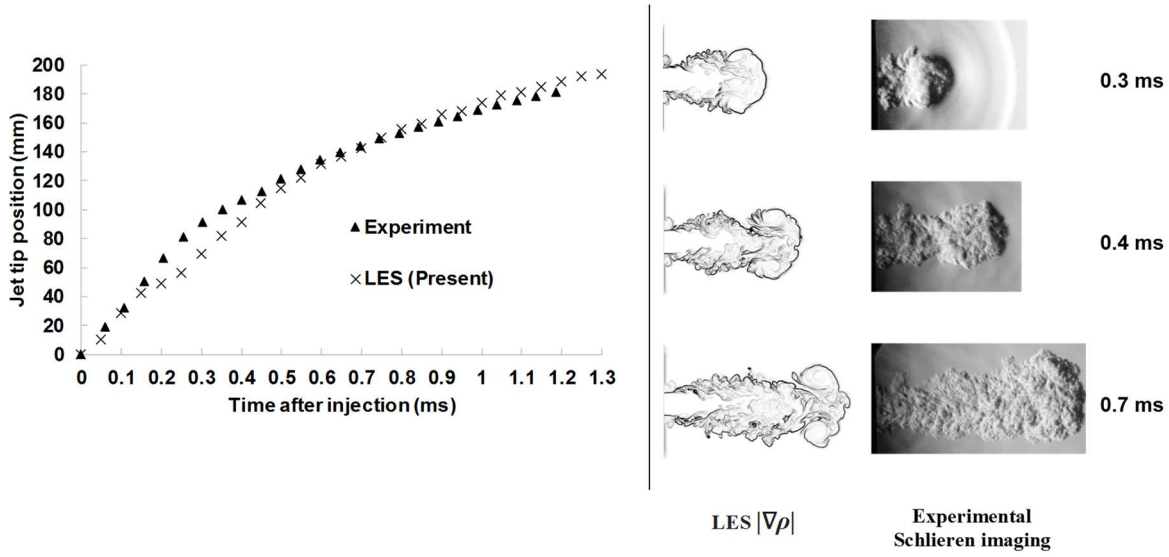

Figure 3-4: Comparison of the non-reacting jet tip penetration (left), and temporal evolution of the jet fluid (right) at Re=113,000.

Based on comparisons with relevant experimental cases in previous works of authors [2, 4], the presented numerical approach has been successful in predicting the spatial evolution of the jet and the pressure rise due to the heat release.

3.4 Analysis and discussion

3.4.1 Ignition kernel development

In jet ignition, high scalar gradients may coincide with high flow strain rates which may deter ignition. One of the objectives of the current work is to examine how the formation of ignition sites is correlated with the values of two scalars: square of mixture fraction gradient and strain rate magnitude. In the present study, mixture fraction (f) is defined to be the fraction of mass originating in the hot jet, thus being zero for far-field fresh reactants and unity at the jet orifice. The square of mixture fraction gradient, $(\nabla f)^2$, is used as an indicator for the scalar dissipation rate. Assessment of the strain distribution plays a key role in identifying the plausible location of ignition. The flow strain rate magnitude is defined as

$$s = \sqrt{\left(\frac{\partial v}{\partial x} + \frac{\partial u}{\partial y}\right)^2 + \left(\frac{\partial w}{\partial y} + \frac{\partial v}{\partial z}\right)^2 + \left(\frac{\partial u}{\partial z} + \frac{\partial w}{\partial x}\right)^2} \qquad \text{Eq. 3-10}$$

where u, v and w are respective velocities in three directions. In order to understand the dynamics of the mixing and ignition processes of the suddenly-starting hot injection into premixed reactants, the instantaneous evolution of temperature, mixture fraction and its squared gradient, and the flow strain rates are shown in Figure 3-5.

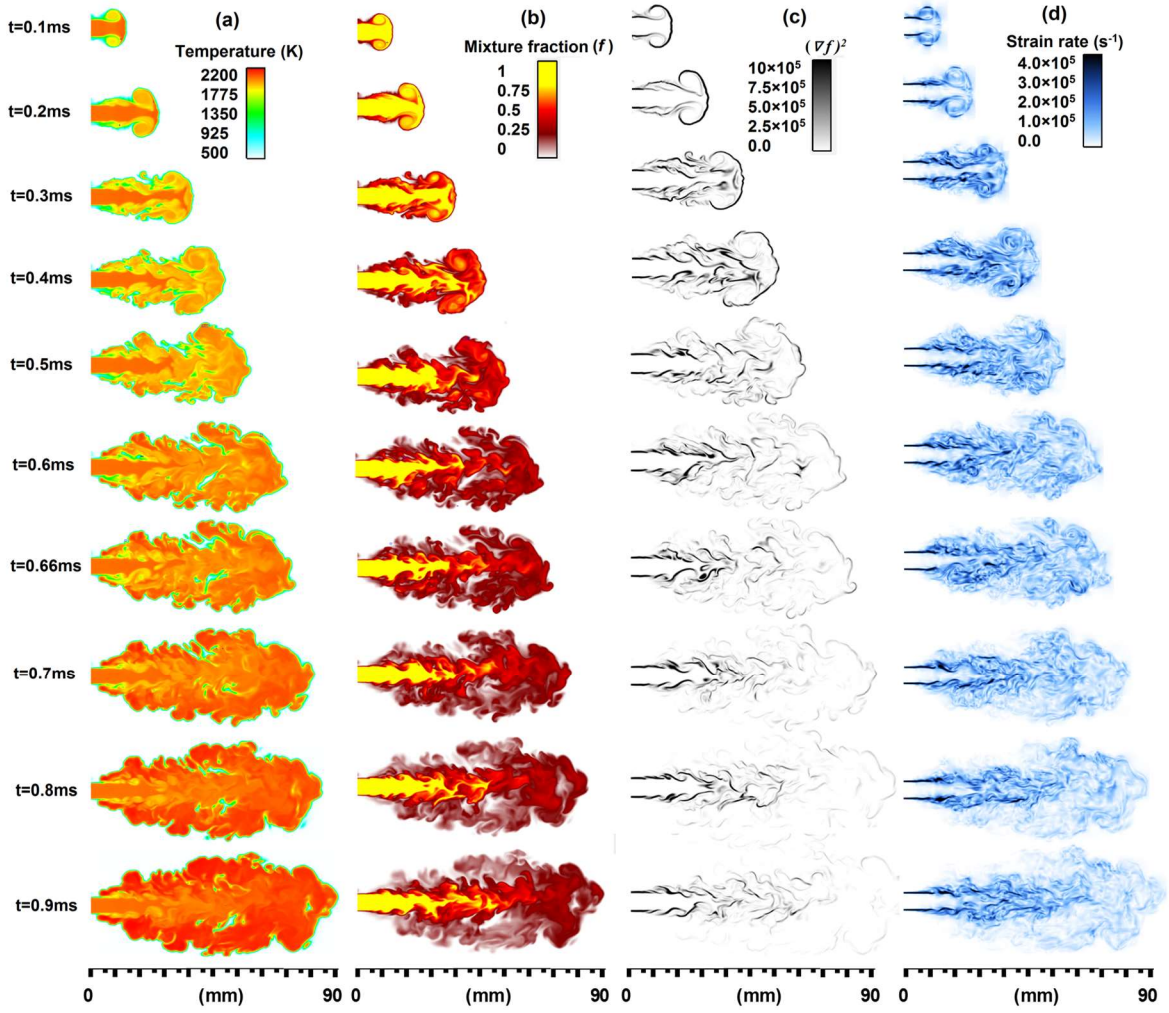

Figure 3-5: Time evolution of ignition for 30%CH_4-70%H_2 mixture in the central-plane. The plots show instantaneous field of temperature (a), mixture fraction (b), squared gradient of mixture fraction (c), and strain rate magnitude (d).

The hot jet emerges from the nozzle with high velocity and creates high strain rates in the leading vortex and trailing shear zone, due to the contact with the surrounding CH_4-H_2-air mixture. The mixture fraction field appears to indicate that effective mixing is mainly driven by large-scale

engulfment of the surrounding gas in the head vortex, and small-scale turbulent diffusion in the jet near-field. The temporal growth of the vortices along with fluctuations in vorticity cause significant mass entrainment around the periphery of the jet resulting in the formation of the local ignition kernels. The population of high-intensity strain rate and $(\nabla f)^2$ fields seem to match over the shear layer fraction of the jet. However, as the velocity and diffusion timescales are not comparable in the leading head vortex, these two domains present dissimilarities in distribution. Consequently, the quantitative study of strain rate and scalar dissipation rate on formation and extinction of ignition kernels are both needed.

Aggregation of local ignition leads to widespread and concurrent local ignition at about t=0.3ms, (referred below as "global ignition") when the temperature of the mixing region starts to increase well beyond the unburned mixture temperature. The variation of mixture fraction derivative suggests that the regions that experience lowest shear are more susceptible to ignition. This effect is observable in Figure 3-6 where the distribution of $Y_{OH}*Y_{CH2O}$ and $(\nabla f)^2$ are plotted. The correlation of OH and CH_2O concentration is known to represent the heat release of initiating reactions and therefore can be indicative of ignition [51]. The rise of instantaneous $(\nabla f)^2$ implies an imbalance between the local heat loss due to thermal diffusion and the rate of heat production due to chemical reactions which can result in ignition quenching [74]. The high values of heat release are generally observed from Figure 3-6 where the high and low values of $(\nabla f)^2$ are at large variance. This observation is consistent with the evidence from the literature [56, 57]. Figure 3-6 also highlights the departure of ignition parcels that are initially generated via auto-ignition and may propagate the reaction zone outside of the mixing region.

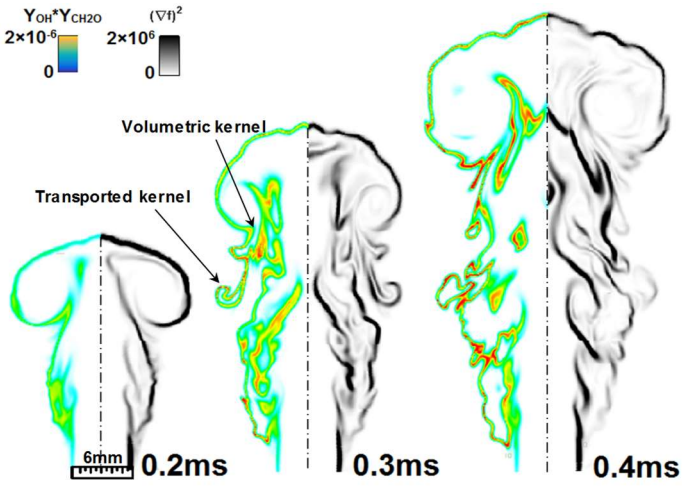

Figure 3-6: Mirrored plot of species and $(\nabla f)^2$ fields shows the high correlation between SDR and ignition (30%CH_4-70%H_2 mixture).

In addition to the diffusive role of SDR in formation and extinction of ignition kernels, it is known that flow strain also affects the formation and propagation of the ignition through kernel-turbulence interactions [73]. If the strain is large, the turbulent eddies can split the ignition zone and cause local extinction once the kernels reduce below the critical size. In particular, development of viscous instabilities in the jet near-field possibly causes the substantial fluctuations of strain rate in this area. [103]. Such fluctuations are observed in Figure 3-7, where the high intensity of strain rate (s≈4×10^5 1/s) results in momentary extinction of the reaction zone, while the subsequent re-ignition occurs as the high strain rate disappears.

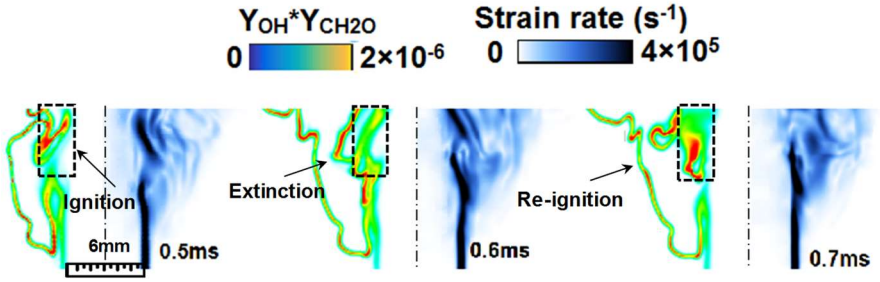

Figure 3-7: Mirrored plot of species and strain rate during the development of extinction and re-ignition (30%CH_4-70%H_2 mixture).

The occurrence of fast chemical reactions in the mixing zone is fundamental to the ignition process. Within acceptable range of temperature and chemical composition, parcels of the jet undergo the fast-rate chemical reactions. Scatter plots of the distribution of gas thermochemical

state in mixture fraction space are presented in Figure 3-8. Mapping the thermochemical properties on the mixture fraction space helps to generalize the arguments regarding ignition development, beyond the specific parameters of the computed case. Formaldehyde (CH_2O) is generally formed earlier in the ignition process followed by OH formation which signals the heat release [72, 104]. In Figure 3-8, the local onset of ignition can be identified by the peak of CH_2O at t=0.1ms in the hotter side of the mixing region where f>0.5. This observation is consistent with the asymptotic study of Law et al. [105] in which ignition is spatially more prone to the hot boundary of the mixing region for reaction orders higher than unity. Substantial OH is formed during the global ignition (t=0.3ms) around f=0.45, while the high-temperature population is also shifting to the same mixture fraction. An increase in temperature at f=0.45 by approximately 200 K is shown at t=0.3ms compared to the prior realization at t=0.1ms. After the global ignition, CH_2O and HO_2 persist in mixture fraction space partially due to the turbulent diffusion and the possible presence of cool-flame regions (T<900K) [106, 107]. It is a common observation that the maxima of all the variables diffuses into lower mixture fractions as premixed flame develops and propagates at later times.

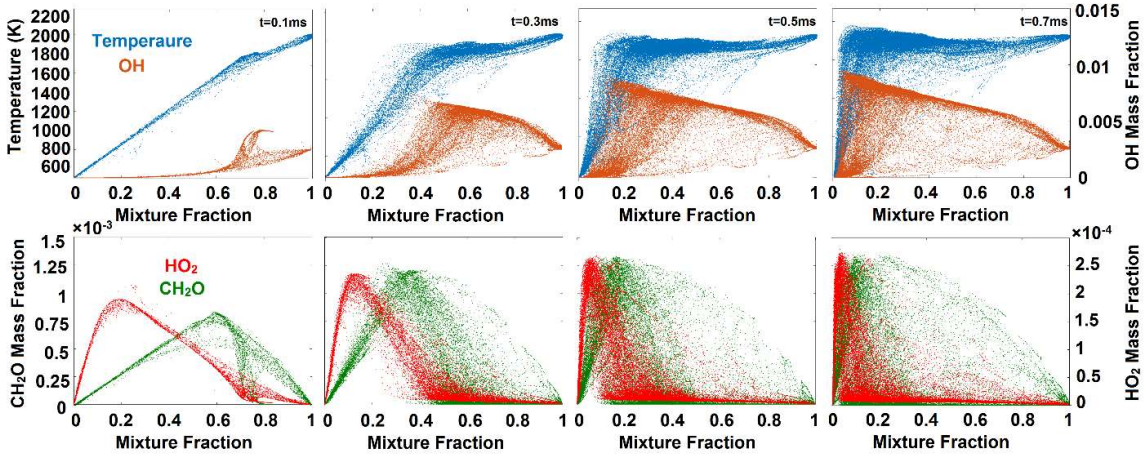

Figure 3-8: Time evolution of temperature, OH, CH_2O and HO_2 mass fraction in mixture fraction (f) space (30%CH_4-70%H_2 mixture).

3.4.2 Statistical evaluation of the ignition characteristics

To obtain further information on the role of scalar dissipation rate, strain rate magnitude and local mixture fraction on ignition success, the statistical behavior of auto-ignition kernels are

studied. Following the Engine Combustion Network recommendations [108] and ignition criteria used by jet ignition studies [109, 110], local ignition is reasonably established when the OH mass fraction of an element exceeds 14% of the quasi-steady state value of the flame ($Y_{OH} > 0.0042$). The elements that exhibit ignition according to this criterion are extracted from the mid-plane shown in Figure 3-2. To assess the correlated effect of scalars, a joint probability density function (PDF) of scalars in the temporal range of global ignition is computed and shown in Figure 3-9. Since the jet fluid is not present over the entire field of study, only the elements that inhabit $0.01< f <0.99$ space are considered. The center of the islands in Figure 3-9 indicates the highest local ignition probability over the studied range of variable.

In early stages of injection (t=0.2ms), it can be seen that the likelihood of local ignition formation emerges at higher mixture fractions f=0.7. However, the peak probability migrates towards lower mixture fractions as the global ignition is attained at t=0.3ms. The ignition success exhibits high probability in the neighborhood of 10^5 s^{-1} and $(\nabla f)^2$=0. As also shown in Figure 3-5, these are often the characteristics of flow structure at inner zone of the leading vortex and small eddies developed on the trailing shear layer. For example, the regions that exhibit $s <<10^5$ s^{-1} often reside on the jet core or far-field where the fuel and oxidizer are unlikely to reach the hot gas. Also, for higher strain rate magnitudes ($s >>10^5$ s^{-1}), the potential ignition sites are rapidly disrupted and quenched [57, 111]. Similarly, the flow structures that experience great values of $(\nabla f)^2$ often quench due to excessive cooling.

One distinct feature of ignition statistics observed in Figure 3-9 is that at the moment of global ignition (t=0.3ms), a larger range of strain rate and $(\nabla f)^2$ become involved in the initiation reactions, compared to the pre-ignition and post-ignition instants. This highlights the presence of a volumetric auto-ignition that emerges in various degrees from a broad mixing region. However, after t=0.3ms, it is apparent that the reaction region reduces with time in $(\nabla f)^2$ and strain rate domains as some of the initial ignition sites cannot survive the high scalar intensities.

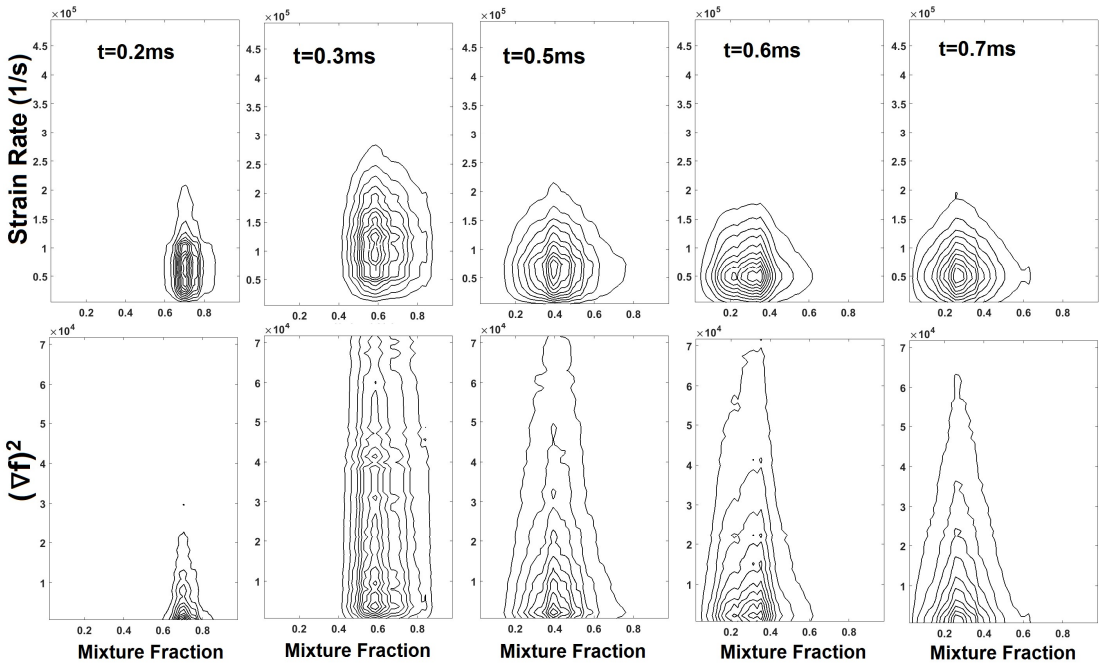

Figure 3-9: Temporal evolution of joint PDFs of $(\nabla f)^2$, strain rate and mixture fraction at the locations on the mid-plane where OH exceeds 14% of quasi-steady state value of the flame (30%CH_4-70%H_2 mixture).

3.4.3 Relation between hydrogen content and locality of the ignition onset

Addition of hydrogen to the fuel stream of IC engines has shown to have improvements on emission reduction due to extending the allowable range of EGR as well as combustion efficiency [112]. As decarbonization of the transportation and power generation sectors becomes inevitable, it becomes important to understand the sensitivity of ignition to hydrogen content. Figure 3-10 compares the experimental values of pressure registered by two pressure transducers PT2 and PT3 in the main chamber as two distinct CH_4-H_2 blends are ignited. The moment of diaphragm rupture and the start of injection (SOI), could be tracked by PT2 in the jet near-field, and the moment of ignition could be identified by the first significant jump of PT3 values. The significant difference between ignition delays of the two mixtures will be later viewed form the transport and chemical perspectives.

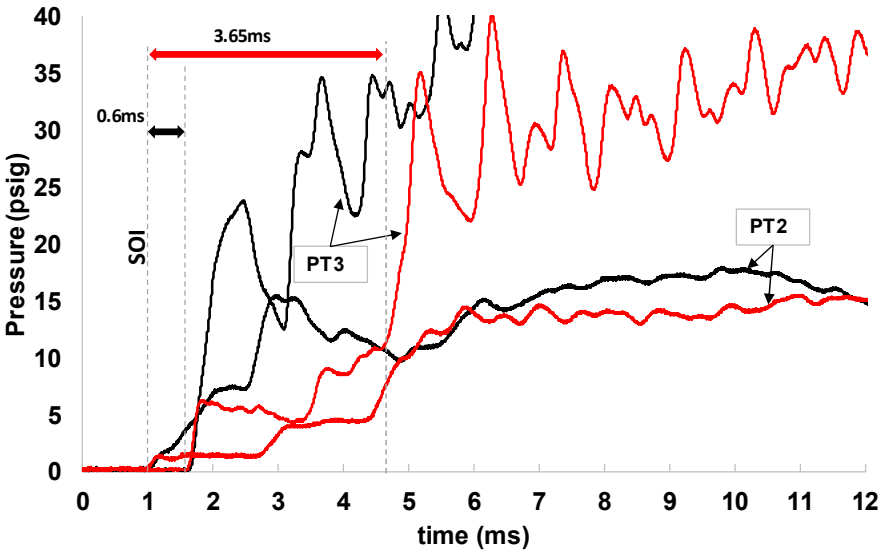

Figure 3-10: Experimental pressure profiles for stoichiometric CH_4-H_2-Air ignition in the near and far-field. Pressure profiles in main chamber for 30%CH_4-70%H_2 (black line), and 50%CH_4-50%H_2 (red line). Ignition delay time is shown for each individual mixture.

Figure 3-11 illustrates the spatial characteristics of hot jet ignition event for 30%-70% and 50%-50% methane-hydrogen ratios. The ignition location could have implications in terms of enclosure and jet design to ensure proper development of ignition. Figure 3-11 shows the high-speed Schlieren imaging of the hot jet issued into two different mixtures of CH_4-H_2-air. The frontiers of ignition are visually detectable from Schlieren images by a trained human investigator or potentially by an image-processing algorithm (not yet developed). The region that is involved in ignition suddenly appears to diminish in grainy black/white contrasts due to small-scale vortex structures with high thermal and density gradients. Instead it adopts a smoother gray color. This is due to sudden thermal expansion of gas by combustion heat release, resulting in much lower density in the region, and disappearance of high-density gas and corresponding gradients. In addition, the ignition timing is derived from pressure traces to confirm the timing of the formation of an ignition front Figure 3-10). For the 30%CH_4-70%H_2 mixture, the ignition frontier, which is indicated by the dashed line in Figure 3-11, appears on the periphery of the jet with the radial range of $r_{ignition}$≈13mm where the mixture fraction is relatively low. Nevertheless, it can be seen that for the 50%CH_4-50%H_2, the ignition occurs closer to the jet core ($r_{ignition}$≈7mm) where a substantial mixing is attained after background gas is entrained to the jet via large-scale engulfment. It is speculated that the ignition process for the fuel with 70% H_2 is likely to be governed by the diffusive transport, while for 50% H_2 large-scale mixing is consequential transport mechanism.

Based on the pressure and visual observations, the reactivity of the fuel is seen to affect the level of mixing required for ignition success, and thus the ignition delay times. This observation is supported by the findings of Zhang et al. [94], in which they classified the ignition characteristics of the hydrogen-methane mixtures into three ignition regimes based on hydrogen contents. Chemistry of mixtures used in the current study is governed by the combined chemistry of methane and hydrogen dominating ignition (CCMHDI) regime. According to Zhang et al., as the hydrogen content of the mixture exceeds 60%, the inhibition of H radicals by CH_4 is significantly restricted, which improves the rate of reaction and shortens ignition delay.

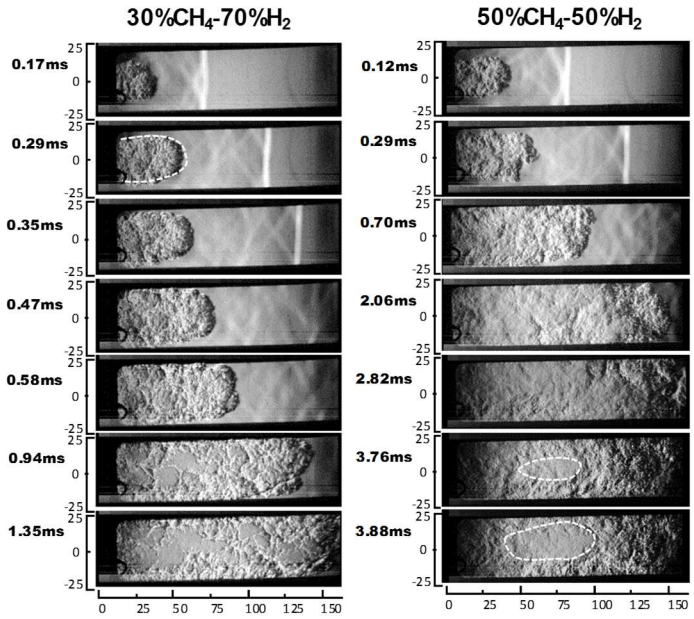

Figure 3-11: Schlieren imaging of ignition formation for different fuel blends. The white dashed line indicates the observable ignition zone (units in mm). 30%CH_4-70%H_2: $r_{ignition}$≈13mm, and for 50-50 blend $r_{ignition}$≈7mm

The experimental observations on the impact of hydrogen content in ignition dynamics motivated further computational analysis in order to better understanding the underlying physics. In Figure 3-12, ignition development predictions are presented for the two CH_4-H_2 fuel blends by plotting the LES-computed distribution of the species-mass-fraction product Y_{H2}*Y_{CH2O} as an indicator of heat release. Besides the quicker advent of heat release in 30%-70% blend, it is observed that heat release occurs mostly in the jet shear layer for this fuel mixture. In contrast, for 50%-50% fuel mixture with slower chemical timescale, the regions of heat release are more present

in the head vortex and inner regions of the jet where higher rates of mixing occurs. This is consistent with experimental observations for the two different mixtures.

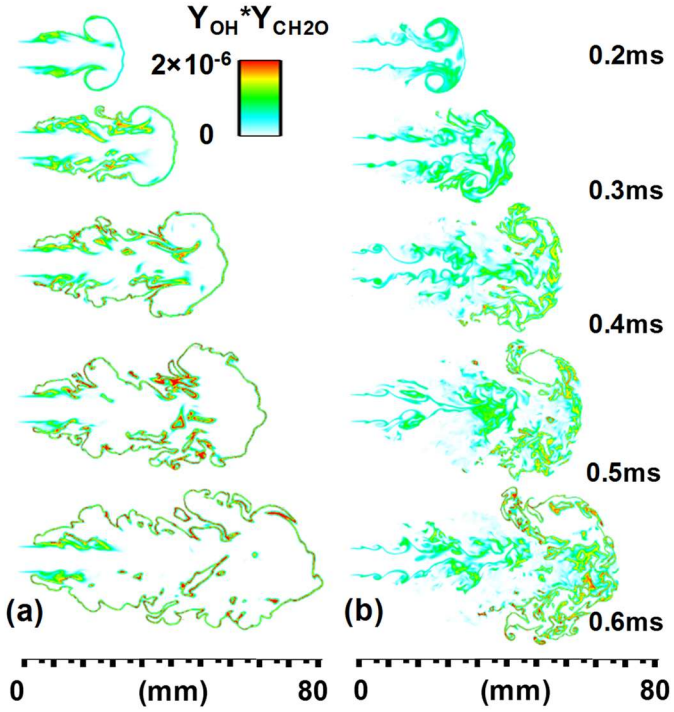

Figure 3-12: Heat release indicated by Y_{OH} *Y_{CH2O} shows the development of initiation reactions for two fuel blends, a) for 30%CH_4-70%H_2 and, b) 50%CH_4-50%H_2.

In order to understand the role of fuel reactivity on the locality of ignition, probability density functions (PDFs) of OH mass fraction are computed at several positions. For the 30%CH_4-70%H_2 mixture, Figure 3-13(a) is a plot of the PDFs for different radial locations where the data for each radius is collected on a line stationed on the mid-plane of the numerical domain. Figure 3-13(b) is a plot of the PDFs for different axial locations where the data for each axial location is collected on a line stationed on the mid-plane of the numerical domain. Local ignition appears to begin in the range r/D=1.3-1.4, where the PDF of OH is highest. It appears from Figure 3-13(b) that the ignition is more likely to occur in the near-field z/D=1. Comparison of the OH mass fraction PDFs for a fuel with lower reactivity (50%CH_4-50%H_2) in Figure 3-14 shows that ignition is more expected to emanate from the regions nearer to the jet axis with r/D=0.7-0.8. The longitudinal position of the high-probability ignition is also shifted further from the nozzle and is

located at *z/D*=4-4.5. These results are in agreement with the observations from Schlieren imaging about ignition location as a function of fuel reactivity.

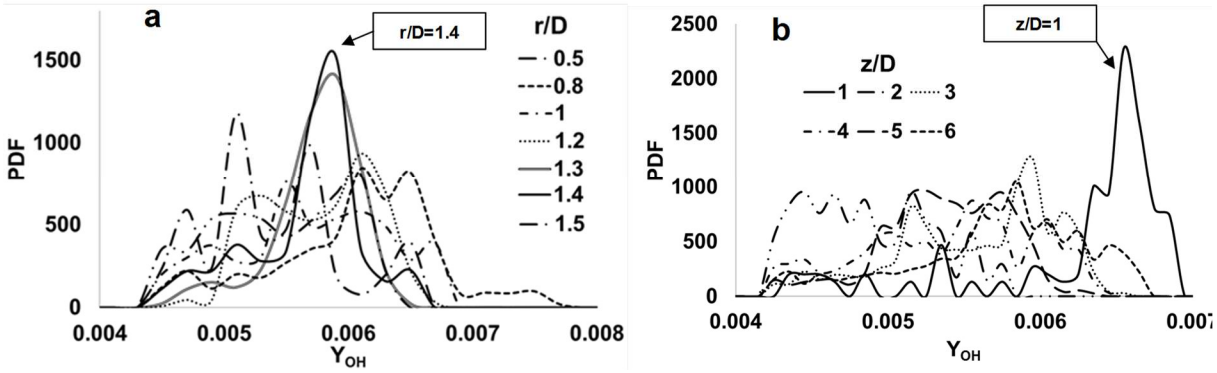

Figure 3-13: Probability density functions (PDFs) of OH mass fraction for 30%CH_4-70%H_2 ignition (a) for different radial locations, and (b) for different axial locations at t=0.3ms after injection.

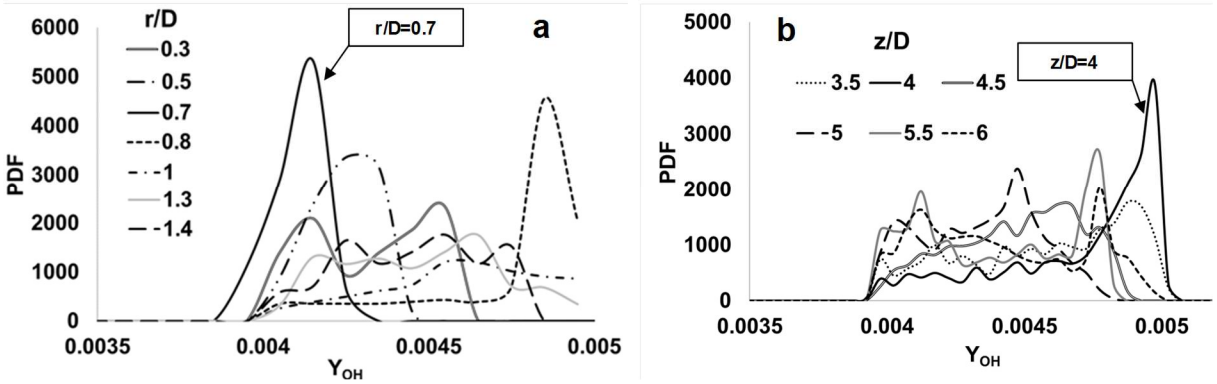

Figure 3-14: Probability density functions (PDFs) of OH mass fraction for 50%CH_4-50%H_2 ignition (a) for different radial locations, and (b) for different axial locations at t=0.3ms after injection.

3.5 Conclusion

In this numerical study of ignition by a transient hot jet, the effect of scalar fields on development of local ignition sites is investigated. The objective is to investigate the range of scalar and thermochemical properties that are supportive of ignition. Experimental high-speed Schlieren imaging and high-frequency pressure measurements are used to observe the locations and timing of ignition. Large eddy simulation with detailed chemical kinetics is used to predict the jet development and ignition, revealing the distribution of mixture fraction, squared gradient of

mixture fraction (representing scalar dissipation rate), flow strain rate, and temperature and chemical composition in the mixing zones.

The key findings of the current work are presented as follows:

- The fields of strain rate, s, and squared gradient of mixture fraction $(\nabla f)^2$ concurrently exhibit high intensities over the shear layer part of the jet. In contrast, within the leading head vortex the diffusive and advective processes scale differently, with the periphery of the jet generally exhibiting high values of $(\nabla f)^2$ while the vortex core exhibits high flow strain rate. It is observed that heat release occurs where $(\nabla f)^2$ exhibits large variance, specifically where eddies roll up. In the shear layer, where flow strain rate (s) is large, the momentary extinction of ignition kernels occur at $s \approx 4\times10^5$ s^{-1}, while the subsequent re-ignition takes place as the strain rate diminishes.
- The distribution of OH and CH_2O in the mixture fraction space indicates that ignition emanates from the regions closer to the hot boundary with $f>0.5$ and gradually migrates away from the jet as the flame develops and propagates. Examination of the joint PDF of the instantaneous scalars indicates pervasive involvement of flow structures in the auto-ignition process at early stages of mixing. However, a substantial fraction of reaction sites later disappear as the ignition kernels experience unfavorable scalar values that may quench or deter ignition. The ignition shows the highest probability at the regions where $s \approx 10^5$ s^{-1} and $(\nabla f)^2=0$.
- The relationship between hydrogen content of the fuel and ignition location and delay time was established using high-speed imaging from experiment and species distribution derived from LES. Both experimental visualization and LES modeling show that for fuel mixture of 30%CH_4-70%H_2, ignition occurs at the jet periphery and relatively close to the nozzle with moderate mixing levels, while for the fuel mixture of 50%CH_4-50%H_2 ignition originates from the core and head vortex parts of the jet and further from the nozzle, where substantial mixing has been attained. The important differences in ignition time delay and location for the two mixtures are believed to be caused by transport properties of hydrogen and chemical dynamics of the chain reactions that inhibit H radicals.

4. MODELING AND ANALYTICAL SOLUTION OF THE NEAR-FIELD ENTRAINMENT IN SUDDENLY-STARTED TURBULENT JETS

Acknowledgment: This is a post-peer-review, pre-copyedit version of an article published in AIAA Journal. The final authenticated version is available online at: https://doi.org/10.2514/1.J057612

4.1 Abstract

The development of the shear-layer flowfield of a round suddenly-starting turbulent jet is analytically investigated within the near-field region of the jet, where the velocity potential core decays. The results of the model are verified and expanded by performing large-eddy simulation of the suddenly-started jet. Unlike quasi-steady approaches, the present work aims at solving the momentum conservation while preserving the time-dependent term. The governing equation is integrated with a mixing-length model to account for the turbulent mixing in the shear layer. The solution is asymptotically applicable to the shear layer of the circular jet and excludes the head vortex mixing. A reasoned calibration of the model parameters for moderate Reynolds numbers results in acceptable agreement for the streamwise entrainment both with experimental data and with large-eddy simulations. The validity limit of the present model is examined by outlining the characteristic length of the velocity potential core as well as the restricting effects of the jet dynamics on the founding assumptions of the model. The study will be instrumental in developing a hot-jet ignition model where the rate of mass entrainment into the jet influences the prediction of ignition based on the temperature and species distribution.

4.2 Nomenclature

b = mixing thickness

U = injection velocity

u = axial velocity

v = transverse velocity

ρ = density

t = time

r = radial coordinate

x = axial coordinate

P = pressure

μ = dynamic viscosity

ε = kinematic viscosity

η = similarity variable

B = mixing thickness constant

α = mixing length constant

f = similarity function

$\dot{M}$ = mass flow rate

Ω = turbulent diffusion constant

z = jet tip position

W = width

D = jet diameter

σ = normal stress

V = volume

τ = non-dimensional time

Γ = circulation

ψ = entrainment ratio

Subscripts

∞ = far-field

0 = nozzle

½ = half-velocity thickness

T = turbulent

in = inner region ($r<r_0$)

out = outer region ($r>r_0$)

e = entrainment

s = surrounding

c = centerline

d = initial velocity difference

4.3 Introduction

The study of transient turbulent jets is relevant to several applications including direct-injection internal-combustion engines, diffusion flames, mixers and spraying devices [113, 114]. Our work is driven by the significance of transient jet studies in hot-jet ignition methods for wave-rotor combustors and other combustion engines [23, 38]. The requirement for fast and effective ignition, especially in combustion devices operating under ultra-lean conditions, urges the utilization of turbulent hot-jet ignition (TJI) [1, 5] in which a transient jet of hot reactive gas is issued to the main chamber and ignites reactants therein a mixing process. In practice, due to the significant difference in pressure between the pre-chamber and the main chamber, the incoming turbulent jet demonstrates complicated features of instabilities and vortex evolution within the shear layer. The complex effect of pressure ratio on the jet dynamics known as shock–shear layer–vortex interaction is discussed by Fernandez et al. [103]. Although the present work does not include chemical reaction in the starting jets, the rate at which momentum is transported from the suddenly-started jet to the quiescent environment is studied in order to develop an understanding on the mass entrainment process.

While there has been substantial investigation of spatially-developed, steady turbulent jets [115], there is relatively little work on transient turbulent jets, including starting jets and brief puffs. In a typical description of the starting turbulent jet, three main regions can be recognized as one observes the field downstream from the orifice: the developing, developed and head vortex region.

Developing or near-field region refers to a phase of jet development where the effects of the jet source still exists. These effects are in particular the laminar-to-turbulent transition of the shear layer (major source of noise generation) and the decay of the velocity potential core. The developing process is known to occur at the following sequence: within one diameter downstream of the orifice [116], the high-speed jet flow forms a laminar shear layer which will quickly transition to the turbulent state. The shear layer grows very rapidly, forming vortices that carry out the turbulent mixing between the jet and the ambient fluid [113]. Studies of starting jets showed the self-preserving behavior of turbulent free jets in the region far from the jet source where disturbance from the developing region disappears in the still fluid [34, 116, 117]. It is understood that at distances equivalent to 10-100 nozzle diameters downstream of the orifice [34], the jet evolves as the self-similar streamwise vorticies. Experimental investigations of starting jets at the far-field suggest similarity, with the standard mass entrainment constant converging to a fixed value [34, 118]. Prior analytical approaches to support the self-preserving behavior of starting jets are based on a quasi-steady interpretation of the momentum solution for jets [25, 119]. While a quasi-steady model for the far-field jet evolution may be reasonable, it fails to predict the near-field behavior of the jet due to underestimation of the shear layer acceleration [120]. The work of Hill et al. [118] on the mass entrainment mechanisms in the near-field region shows growing of entrainment ratio which asymptotically converges to self-preserving values mainly due to the existence of the velocity potential core. Meanwhile, the momentum potential core gradually shrinks and releases momentum to the mixing region, accelerating the ambient fluid, consistent with the classic representation of the free jet.

The subject of turbulent jets with time-varying sources has been addressed through exact or approximate solutions of the momentum equation [88, 121, 122]. The mathematical study of transient jets and puffs presents challenges due to the ever-changing domain of the velocity field. A pioneer in studying turbulent transient boundary layers is Prandtl [123], who addressed the problem of "smoothing out of velocity discontinuity" in a 2D domain, where two parallel streams with different velocities are issued at t=0. Due to the turbulent diffusion of momentum, the velocity profile gradually becomes smooth.

In the present work, a similar effort is made to apply the smoothing method to the transient solution of the near-field round turbulent jet that is suddenly started. Paik [18] and Kojok [124] conducted experimental studies of the hot jet that emerges from a pressurized pre-chamber into a

main chamber as the diaphragm separating pre-chamber from the main chamber abruptly ruptures. In the current study, this process is replicated by initially assigning a finite velocity to the jet at the nozzle and preserving the injection velocity throughout the study. The term "suddenly-started" in this study refers to the aforementioned injection regime. The model incorporates turbulence using the simplified Prandtl mixing length hypothesis to the extent of mixing thickness. Once calibrated with real jet information, the solution is capable of describing the axial velocity distribution of the near-field jet with respect to time. At the prescribed Re range, the model can yield the varying rate of mass entrainment that reflects the non-preserving values reported in the developing jet studies [125, 126]. The study also encompasses the large eddy simulation (LES) of iso-thermal suddenly-started jets at moderate Reynolds numbers, in an attempt to identify the limitations of the proposed explicit analytical solution for the momentum equation

4.4 Analytical and computational formulation

The transient round free jet near the issuing orifice can be generalized as a co-flow problem in which the central flow is issued into a slower-flowing annular environment. At the time $t=0$, the two streams are issued with velocity U_0 and U_∞, where U_∞ is zero in the present study. As the streams travel alongside each other with negligible transverse velocity, the shear-layer mixing smooths outs the velocity profile (Figure 4-1). The analogy between transient co-flow and the near-field free jet can be applied up to the point where the momentum diffusion thickness reaches to the centerline ($b=r_0$).

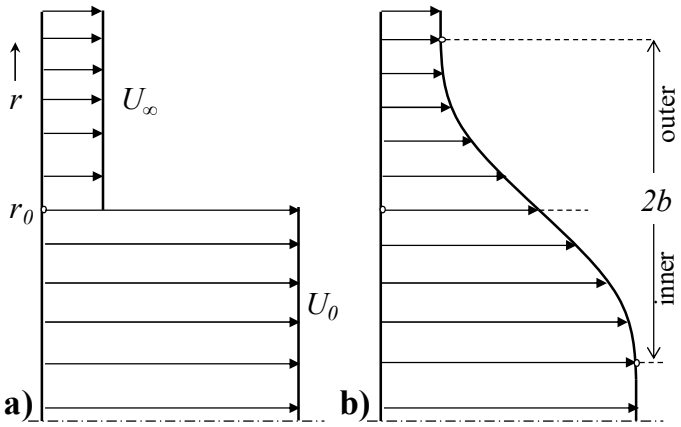

Figure 4-1: Development of the round free jet velocity boundary layer; a) Initial profile at t=0, b) velocity profile at a later instant.

4.4.1 Momentum equation

The present study focuses on free jets at moderate and high Reynolds numbers (*Re*=5,000−20,000) with turbulent mixing-length model imposed, and the solution of the momentum equation could be sought within the extent of predominant velocity gradients. The mass and axial momentum conservation equations in the 2D-axisymmetric coordinates are,

$$\frac{\partial \rho}{\partial t} + \frac{1}{r}\frac{\partial}{\partial r}(r\rho v) + \frac{\partial}{\partial x}(\rho u) = 0\,, \qquad \text{Eq. 4-1}$$

$$\rho\left(\frac{\partial u}{\partial t} + u\frac{\partial u}{\partial x} + v\frac{\partial u}{\partial r}\right) = -\frac{dP}{dx} + \frac{1}{r}\frac{\partial}{\partial r}\left(r\mu_T\frac{\partial u}{\partial r}\right) + \mu_T\frac{\partial^2 u}{\partial x^2}\,. \qquad \text{Eq. 4-2}$$

where ρ, P, u and v represent the gas density, pressure and velocity in axial and radial directions, respectively. Consistent with the co-flow analogy and for moderate jet velocity, the following assumptions are made: (*i*) The gas is incompressible, (*ii*) the jet stream is not confined hence the pressure gradient is negligible, (*iii*) at the regions near the orifice, transverse velocity is negligible and, (*iv*) the centerline velocity is constant within the velocity potential core. The assumptions (*i*) and (*iii*) in combination with Eq. 4-1 implies that the axial velocity gradient is insignificant. Although some studies suggest the importance of the axial decay of the advective and diffusive terms in turbulent jet emergence [127], the computational studies made by the authors support negligibility of advection and diffusion terms within the extent of the velocity potential core.

In Eq. 4-2, μ_T is the turbulent dynamic viscosity. In the free jet, diffusion of momentum occurs simply due to shear stress with minor flow deflection. The turbulent viscosity is thus modeled using the Prandtl mixing theory where $\varepsilon_T = \frac{\mu_T}{\rho}$ can be modeled using Eq. 4-3 where l represents the empirical mixing length.

$$\varepsilon_T = l^2 \left|\frac{\partial u}{\partial r}\right|, \qquad \text{Eq. 4-3}$$

Implementing the assumptions (*i*) to (*iv*) leads to the reduced form of the axial momentum equation,

$$\frac{\partial u(r,t)}{\partial t} = \frac{1}{r}\frac{\partial}{\partial r}\left(r\varepsilon_T \frac{\partial u(r,t)}{\partial r}\right), \qquad \text{Eq. 4-4}$$

where ε_T can be modeled using Eq. 4-3.

As already shown in Figure 4-1, the boundary across which the velocity varies discontinuously is transitional and the smoothing process occurs via turbulent mixing within the mixing thickness. Eq. 4-4 does not depend on the axial coordinates; thus, it can represent the velocity evolution at any given axial section for which the initial mixing thickness was zero. This circumstance might resemble the jet tip in the absence of leading vortex. Based on the similarity of the velocity profile in various axial distances, the partial differential Eq. 4-4 can be transformed to an ordinary differential equation using the similarity variable $\eta=r/Bt$ which lumps the two independent variables of time and radial coordinates, where B is a constant. In the scale analysis of turbulent free jets, the mixing thickness b shown in Figure 4-1 varies linearly with time [123] showing that $b=Bt$. When addressing the problems of turbulent jets and wakes, it is usually assumed that the mixing thickness, b, is also proportional to the mixing length, l in Eq. 4-3 [123]. In this way, we are led to the useful result that the mixing length is also a linear function of time i.e. $l=\alpha t$ where α is an empirical constant. The proportionality of mixing length and mixing thickness allows us to group the time and space coordinates appeared in Eq. 4-4 into the similarity variable η.

Now that the similarity variable is established, the velocity function, $u(r,t)$, is re-written in terms of the similarity function $f(\eta)$, where $0 \leq f \leq 1$:

$$u(r,t) = U_0 - U_d\, f(\eta) \qquad \text{Eq. 4-5}$$

In Eq. 4-5, $U_d = U_0 - U_\infty$ where U_0 and U_∞ are the jet exit velocity and ambient fluid velocity, respectively. The temporal and spatial derivatives of the velocity in the new coordinates are

$$\frac{\partial u}{\partial t} = f'\frac{\eta}{t}U_d \quad ; \quad \frac{\partial u}{\partial r} = -f'\frac{\eta}{r}U_d \quad ; \quad \frac{\partial^2 u}{\partial r^2} = -\frac{\eta}{r^2}(f''U_d\eta + f'U_d) .$$

By plugging the derivatives and new definition of velocity into Eq. 4-4 and some rearrangements, the following ordinary differential equation for axial momentum is obtained

$$f''\eta + 2f' - \frac{B^3}{\alpha^2 U_d}\eta = 0 \ , \qquad \text{Eq. 4-6}$$

The overall solution for the second order ODE (Eq. 4-6), which constitutes from the homogeneous and nonhomogeneous solutions, is proposed as

$$f = \frac{-C_1}{\eta} + \frac{B^3}{12\alpha^2 U_d}\,\eta^3 + C_2 \ , \qquad \text{Eq. 4-7}$$

where C_1 and C_2 are the solution constants.

The region which is addressed by the solution is within the extent of momentum diffusion thickness ($r_0 - b < r < r_0 + b$ in Figure 4-1). The problem boundaries require the velocity equal to U_0 and U_∞ at $r = r_0 - b$ and $r = r_0 + b$, respectively. In addition, the velocity gradient at the aforementioned boundaries is specified to be zero. Given that the two co-flow streams meet at the nozzle radius r_0, the variable η_0 is defined as $\eta_0 = r_0/Bt$ for $t > 0$. Even though the axial coordinate is not incorporated in development of the Eq. 7, dependency of the solution to the axial coordinate is implicitly determined by the fact that the boundary conditions ($\eta = \eta_0 - 1$ and $\eta = \eta_0 + 1$) are constantly varying with time. Translation of the physical boundary conditions to the η space implies the following boundary conditions

$$f = f' = 0 \ at \ \eta = \eta_0 - 1 \quad ; \quad f = 1, f' = 0 \ at \ \eta = \eta_0 + 1 .$$

Since Eq. 7 has two constants, it will not accommodate all the four boundary conditions in one solution. Hence, two sets of solutions (inner and outer shown in Figure 4-1) would be constructed each addressing one side of the shear interface ($r = r_0$). The two solutions then are matched at the interface with the aid of a piece-wise polynomial patch.

Inner solutions would be plausible for $\eta_0 - 1 < \eta < \eta_0$ where the constants of Eq. 4-7 are defined as

$$C_{1,in} = -\frac{B^3}{4\alpha^2 U_d}(\eta_0 - 1)^4 \quad ; \quad C_{2,in} = \frac{C_{1,in}}{(\eta_0 - 1)} - \frac{B^3}{12\alpha^2 U_d}(\eta_0 - 1)^3 \ ,$$

and the outer solution addresses the region $\eta_0 < \eta < \eta_0+1$ which yield to the following constants

$$C_{1,out} = -\frac{B^3}{4\alpha^2 U_d}(\eta_0 + 1)^4 \ ; \quad C_{2,out} = 1 + \frac{C_{1,out}}{(\eta_0 + 1)} - \frac{B^3}{12\alpha^2 U_d}(\eta_0 + 1)^3 \ .$$

In order to maintain the continuity of the function *f* and its first derivative at the matching point, η_0, a cubic polynomial function is employed to patch the inner and outer solution within the 5% of the overall jet thickness. If preferred, a closer match with experimental data may be obtained by matching only continuity of the function itself.

4.4.2 Shear layer mass entrainment

Developing the velocity profile done by Eq. 4-5 and Eq. 4-7 helps to characterize the rate of mass entrainment that occurs by the acceleration of surrounding fluid due to the jet impulse. At a given axial position, the jet mass flow rate as a function of time is:

$$\dot{M}(t) = 2\pi \int_{r=0}^{\infty} \overline{\rho u}\, r\, dr,$$

where u is introduced by the velocity definition in Eq. 4-5 and thus, the integral must be reconstructed in terms of the similarity variable η. The jet mass flow rate in the transformed space is

$$\dot{M}(t) = 2\pi\rho(Bt)^2 \begin{pmatrix} \frac{U_0}{2}(\eta_0 + 1)^2 - U_d\left[-C_{1,in}\eta + \frac{\Omega_{in}}{15}\eta^5 + \frac{C_{2,in}}{2}\eta^2\right]_{\eta_0-1}^{\eta_0} \\ -U_d\left[-C_{1,out}\eta + \frac{\Omega_{out}}{15}\eta^5 + \frac{C_{2,out}}{2}\eta^2\right]_{\eta_0}^{\eta_0+1} \end{pmatrix}, \qquad \text{Eq. 4-8}$$

where $\Omega = \frac{B^3}{4\alpha^2 U_d}$ is the turbulent diffusion constant that is independently assigned to inner and outer regions and $\eta_0 = r_0/Bt$. Derivation of jet flow rate assists with characterization of mass entrainment rate as $\dot{M}_e = \dot{M} - \dot{M}_0$ where $\dot{M}_0$ accounts for the injected mass flow rate. Parameter ψ represents the normalized entrainment ratio which can also account for the difference of density between the jet and ambient fluid [118]. Entrainment ratio is defined as

$$\psi = (\dot{M}_e/\dot{M}_o)(\rho_o/\rho_s)^{\frac{1}{2}}, \qquad \text{Eq. 4-9}$$

where ρ_o and ρ_s represent the fluid density at the orifice and sufficiently far from the orifice, respectively.

The solutions obtained from Eq. 4-6 address the inner and outer regions independently which allows the model to accommodate different turbulent properties (Ω) for each region. The velocity profiles provided by Eq. 4-7 are compared against the experimental results of Obot et al. [128] which addresses the near-field evolution of the velocity field over the decaying phase of velocity potential core. Whereas the present model assumed a top-hat velocity profile of the jet, it is likely that the experiment of Obot et al. would have a fully-developed velocity profile at the nozzle due to the nozzle length. Figure 4-2 shows the normalized axial velocity distribution in various development stages in the near field and compares the values with experimental data. Throughout this study, variable z describes the tip position of the jet as a function of time ($z=U_0 t$).

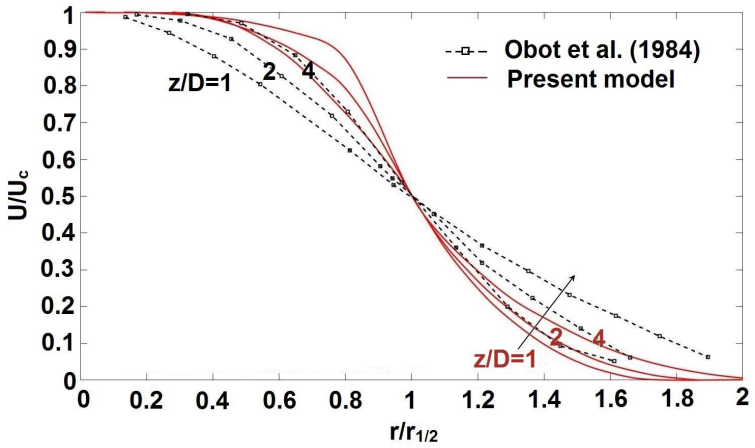

Figure 4-2 : Comparison of the radial distribution of axial velocity normalized by half-velocity width (r1/2) for Re=12800 at various jet tip positions. Turbulent diffusion coefficients ($\Omega_{in} = 0.360s^{-1}; \Omega_{out} = 0.102s^{-1}$)

The calculated velocity profile has a remarkable feature; it does not asymptotically exceed the velocity in the jet or far-field. As observed in Figure 4-2, the momentum diffusion thickness stretches on the both sides of the shear interface in proportion to the designated turbulent diffusion factor Ω. Through the appropriate calibration of the model, it is observed that the inner region demonstrates stronger turbulent diffusivity (Ω_{in}/Ω_{out}=3.52) which may relate to the high flow disturbance generated at the nozzle. Additionally, the study of Bogey and Bailly [129] and current LES asserts the higher turbulence intensity and kinetic energy in the regions close to the centerline compared to the transverse far-field.

4.4.3 Large eddy simulation of suddenly-started jet

In order to further expand the applicability of the developed entrainment model, a series of numerical simulations are conducted using large-eddy simulation of a suddenly-started turbulent jet at moderate Reynolds numbers (5,000<*Re*<20,000). The computational domain is partially adapted from the works of Paik and Kojok [18, 124]. The domain consists of a D=3mm circular orifice connected to a rectangular enclosure with side and length ratios of W/d=8 and L/d=30, respectively. A starting jet of air is suddenly issued from the nozzle with standard temperature and pressure conditions and at uniform velocity with 2% turbulent fluctuation of the mean flow velocity. A block-structured base grid is employed for the LES reported, and in combination with adaptive mesh refinement (AMR) [130], the cell size distribution is chosen to provide sufficient resolution for turbulent boundary layer and sharp representation for pressure waves. The base-grid cell size of 0.5 mm is refined via AMR to generate cells size of 60 μm at the cells with velocity above 0.1% of the nozzle tip velocity. A similar cell size is also practiced in the work of Validi and Jaberi [52] and demonstrates good resolution of turbulent flow structures. Based on the scaling law, the targeted grid refinement criteria is able to resolve more than 85% of the turbulent kinetic energy according to a similar study by Nordin-Bates et al. [70]. Direct numerical studies of prechamber-generated hot jets of similar design determined the Kolmogrov length and time scales as 19 μm and 3.52×10^{-6} s, respectively [51]. Mesh independence was established by testing various base-grid cell sizes, with tracking of jet tip penetration. In Figure 4-3, it can be seen that the jet development is quite consistent among the three meshes, with a largest deviation at 0.9 ms of no more than 3%. Thus, base cell size of 0.5mm is opted for the current study. The numerical convergence is attained via continuation of the iterative calculations in order to maintain the relative residual values of the mass and momentum conservation equations below 1%.

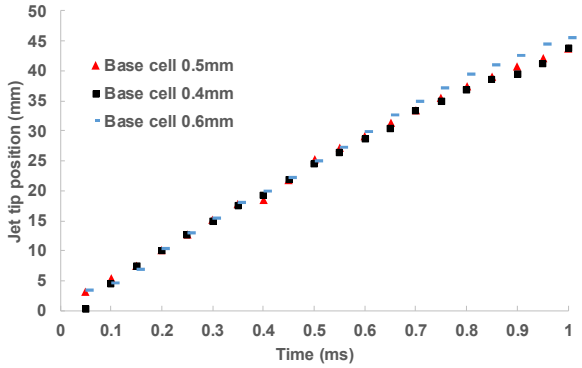

Figure 4-3: The jet penetration time development with different base-grid resolutions in the 3D LES (D=3mm, Re=19,000).

Figure 4-4 presents a comparison of jet tip progress when issued from the pre-chamber at near-sonic speeds, between the LES method that is currently used and an experiment that utilized equipment described in Kojok [124]. In the study of Kojok, jet is issued from the pre-chamber to a transparent main chamber where the jet is visually accessible via Schlieren method. The agreement of the jet progress between the near and farfield is acceptable while the LES lacks accuracy during the transitional stage from developing to the developed flowfield.

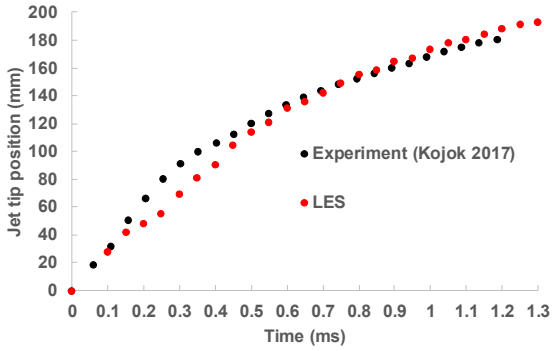

Figure 4-4: Comparison of the non-reacting jet tip penetration with the experimental work of Kojok (T_{stag} =1160K, Re=132,000).

In the current work, a spatial discretization of second order and implicit first-order accurate time-integration scheme are used to solve the governing conservation equations. A variable-time-scale algorithm is used, with time-step varying between 10^{-8} and 10^{-7} seconds.

The Favre-averaged compressible form of the Navier-Stokes equations are solved in LES [62],

$$\frac{\partial \bar{\rho}}{\partial t} + \frac{\partial \bar{\rho}\widetilde{u_j}}{\partial x_j} = 0, \qquad \text{Eq. 4-10}$$

$$\frac{\partial \bar{\rho}\,\widetilde{u_i}}{\partial t} + \frac{\partial \bar{\rho}\widetilde{u_i}\widetilde{u_j}}{\partial x_j} = -\frac{\partial \bar{P}}{\partial x_i} + \frac{\partial \overline{\sigma_{ij}}}{\partial x_j} - \frac{\partial \tau_{ij}}{\partial x_j}. \qquad \text{Eq. 4-11}$$

The effect of the small scales appears through a subgrid-scale (SGS) stress term,

$$\tau_{ij} = \bar{\rho}\left(\widetilde{u_i u_j} - \widetilde{u_i}\widetilde{u_j}\right). \qquad \text{Eq. 4-12}$$

It is difficult to evaluate the SGS directly and therefore it must be modeled. The present study employs Dynamic Structure LES [63] model to approximate SGS stress tensor by adding a sub-grid kinetic energy equation,

$$\frac{\partial \bar{\rho}\,k}{\partial t} + \frac{\partial \bar{\rho}\widetilde{u_j}k}{\partial x_j} = \frac{\partial}{\partial x_j}\left(\frac{\mu}{Pr_{sgs}}\frac{\partial k}{\partial x_j}\right) + \tau_{ij}\overline{S_{ij}} - \rho\epsilon\ , \qquad \text{Eq. 4-13}$$

where Pr_{sgs} is set to 1. The SGS kinetic energy and dissipation rate are given by Eq. 4-14 and Eq. 4-15, respectively,

$$k = \frac{1}{2}\left(\widetilde{u_i u_j} - \widetilde{u_i}\widetilde{u_j}\right), \qquad \text{Eq. 4-14}$$

$$\epsilon = C_e\frac{k^{1.5}}{\Delta}, \qquad \text{Eq. 4-15}$$

where C_e=1 and Δ is the local grid length scale. The SGS stress tensor (τ_{ij}) is now modeled by

$$\tau_{ij} = 2k\bar{\rho}\frac{L_{ij}}{L_{kk}}, \qquad \text{Eq. 4-16}$$

where L_{ij} is the Leonard stress tensor and is defined as $L_{ij} = \widehat{\widetilde{u_i}\widetilde{u_j}} - \widehat{\widetilde{u_i}}\widehat{\widetilde{u_j}}$. The "$\widehat{\ }$" indicates the test-level filter that is larger than the sub-grid level and has the advantage of being resolved.

In Figure 4-5, to validate the present numerical setup, LES of a fully-developed jet is carefully compared against the experimental data of Obot et al. [128] at similar Reynolds number and density ratios. Additionally, the self-preserving jet model developed by Hussein et al. [131], which describes the centerline velocity decay, is used to test the validity of the present LES. The model proposed by Hussein et al. suggests the variations of centerline velocity for self-preserving part of the jet by the following equation

$$\frac{U_0}{U_c} = \frac{1}{B_u}\left[\frac{x}{D} - \frac{x_0}{D}\right], \qquad \text{Eq. 4-17}$$

where x represents the axial coordinate, x_0 is the virtual origin which coincides with the nozzle tip and B_u is the decay constant equal to 5.6.

The centerline velocity provided by present LES in Figure 4-5, is the resultant of Favre-averaging of instantaneous axial velocity over 3ms which is about 25 times the integral time scale (t_0=0.12ms). Despite the difference between the values at far-field at Re=13000, the model and experimental data values show satisfactory agreement with the LES results over the self-preserving course of the jet. The present LES and the model of Hussein et al. both employ the top-hat velocity profile at the nozzle which makes the velocity comparison between two more favorable. The far-field deviation of LES and empirical data might be due to the acoustic interactions of the jet and reflective walls which is not present in the self-preserving hypothesis or the experiment.

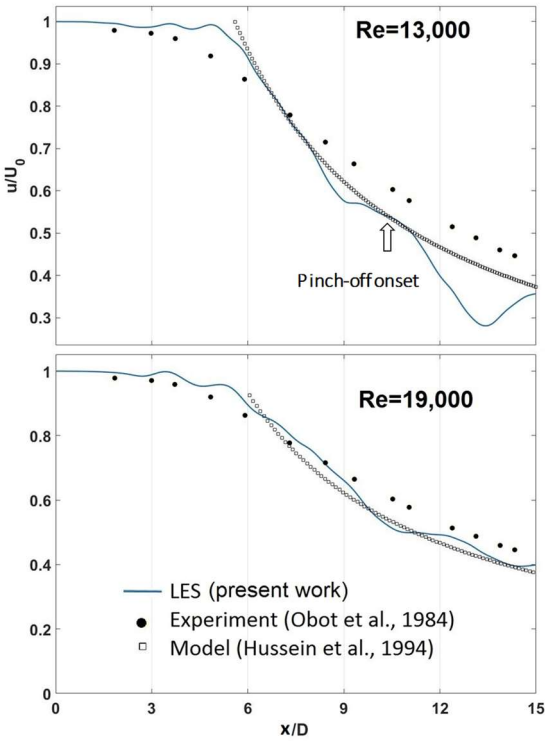

Figure 4-5: Centerline velocity decay− Validation of LES with experimental data and analytical model.

Further comparison of the radial distribution of axial velocity is conducted between the present LES and the experimental modeling of Bremhorst and Hollis [132] (Figure 4-6). The top-

hat profile at x/d=5 is less consistent with the hotwire measurements while the x/d of 7 and 10 present better agreement with the universal trends suggested by Bremhorst [132].

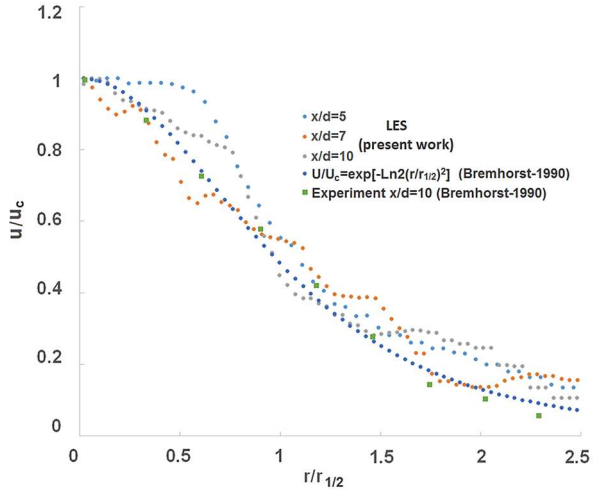

Figure 4-6: Mean axial velocity profile− Validation of LES (Re=5000) with experimental and modeling data.

4.5 Model calculations and discussion

4.5.1 Near-field entrainment characteristics

The growth of mass flow rate at consecutive cross-sections of the jet is a measure of jet entrainment, which is essential to understanding the heat and mass interactions of the jet with its environment. Hill [118] performed a survey on the measurements of the profiles in the region immediately downstream of the nozzle and calculated jet mass flow rates. Within this region, the velocity profile changes from that of the entering jet to that of fully developed flow. Despite the quantitative differences between the reported results from Hill [118] in terms of the normalized entrainment rate, each of these realizations showed that the mass flow rate of a jet increases nonlinearly in the near-field region before it reaches to the constant value at the fully-developed region.

The expression provided in Eq. 4-8 and Eq. 4-9 for the axial mass entrainment rate is valid for the near-field region where the potential core exists. Figure 4-7 gathers the data of a group of available studies on steady and transient free jets that report the near-field mass entrainment of

turbulent free jets with moderate Reynolds numbers. Parameter ψ of Eq. 4-9 represents the normalized entrainment ratio.

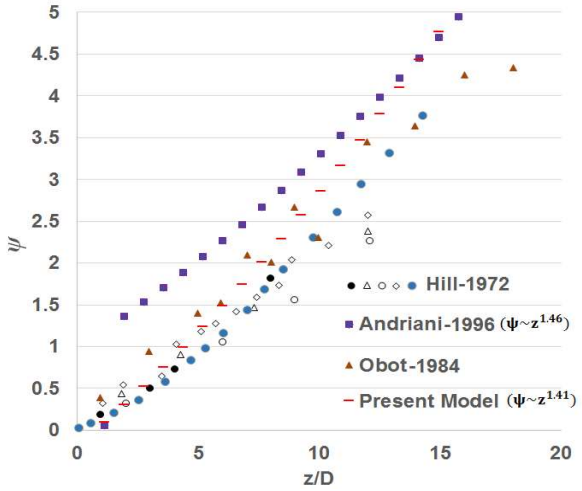

Figure 4-7: Variation of entrained ratio with axial distance in the initial region (10,000 <Re<100,000) [79, 118, 128]

The turbulent diffusion coefficients for the model obtained by the work of Obot et al. (Figure 4-2) are employed in Eq. 4-8 and the results are shown in Eq. 4-7 in terms of the normalized entrainment ratio. While the study of Andriani [79] on unsteady gaseous jets shows the relationship of entrainment ratio to jet tip position as $\psi = \psi\ (z^{1.46})$, the present model predicts $\psi = \psi\ (z^{1.41})$, closer to the experimental data. The pioneering work of Abraham [119] on the mass entrainment of starting jets suggests a linear dependence between the entrainment rate and the jet tip distance from the nozzle over the entire course of injection. Although this characteristic of the model makes reasonable agreement with the whole embodiment of the jet, it lacks accuracy for the near-field region as the model is based on quasi-steady approach.

4.5.2 Temporal dynamics of the mass entrainment rate

The mass entrainment ratio (ψ), as a function of non-dimensional time $\tau = t/t_0$ is plotted in Figure 4-8-a where t_0 is 0.12ms for this study. The LES data for mass entrainment is obtained via measuring the growth rate of plume. The plume is identified in a region wherein the nozzle-originated scalar concentration is between 5 to 100%. The changing rate of the plume volume generated by this criterion is then used to characterize the rate of mass entrainment from the surrounding environment. Since the model introduced in Eq. 4-8 does not account for the

entrainment via head vortex structure, in the LES analysis we exclude the mass entrainment associated with the vortex head by assuming a prescribed function for vortex head volume with respect to time as $V_{vortex} = 6 \times 10^{-4} t$ [133].

When using the turbulent diffusion coefficients found for the two studied Reynolds numbers, good agreement is noted during initial jet entry between the predicted values from Eq. 4-8 and the entrainment ratios computed by LES. However, at later times, the LES-computed entrainment falls away from the analytical trend. Visualization of the jet dynamics reveals that at about τ=6 the head vortex ring detaches from the trailing jet and propagates ahead. This separation process is known as 'pinch-off' and occurs as the vorticity transport to the vortex head is discontinued due to the shear layer instabilities [103]. A well-known metric to characterize the occurrence of pinch-off is the abrupt variation of the cumulative flow circulation in the semi-plane that contains the jet axis due to the circulation saturation of the vortex head. The details of this technique are elaborated in the work of Pawlawk et al. [134]. The development of Kelvin-Helmholtz instabilities on the shear layer that gives rise to the pinch-off is illustrated in Figure 4-8-b. It is observed that when pinch-off occurs, the centerline axial velocity is disturbed by the departure of the head vortex. Thus, the analytical model's key assumption of constant centerline velocity is violated, and the model no longer predicts entrainment well.

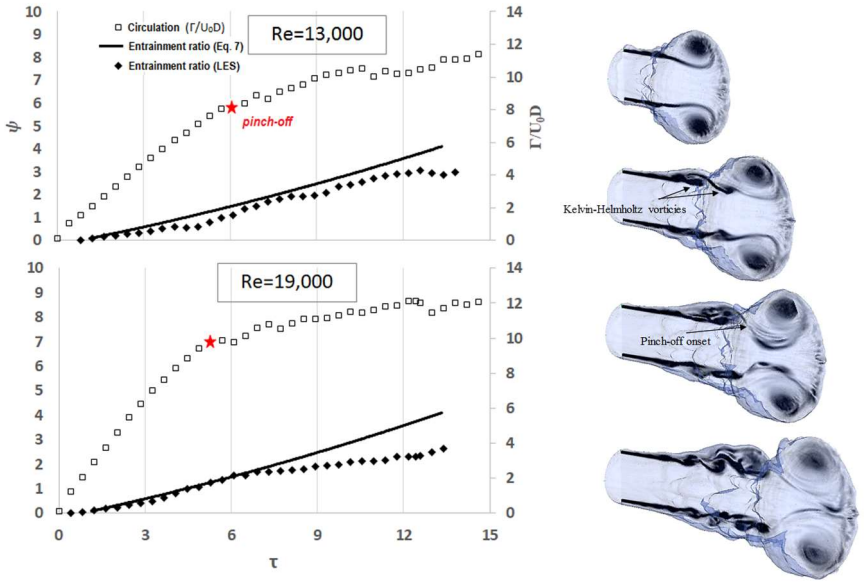

Figure 4-8: (a) Modeled and computational values of entrainment ratio and, (b) the development of the Kelvin– Helmholtz vortices at Re=19000. The vorticity magnitude is shown in black and white contours. Jet boundaries indicated by light shading.

4.5.3 Spatial applicability of the model

In the derivation of Eq. 4-8, the explicit solution for the axial momentum equation was sought with the prescribed velocity on the centerline, which implies the applicability of the solution only within the length of the velocity potential core. In the initial phase of the starting jet, the velocity potential core extends from the nozzle tip to the point where emergence of the head vortex perturbs the jet exit velocity, but the core shrinks as the shear layer widens. The potential core termination is identifiable where the velocity gradient on the axis fluctuates abruptly. Figure 4-9-a shows the temporal evolution of the axial velocity gradient as the suddenly-started jet advances.

For Re=5000, Figure 4-9-a shows the accumulation of velocity gradient maxima at $z/D\approx8$ which shows the extent to which the potential core can stretch. With the increase of Re to 6300 and then 19800, the termination location of the potential core shifts towards $z/D\approx5$, progressively. Figure 4-9-b depicts the instantaneous dynamics of the jet in terms of the vorticity at a constant Reynolds number. Vorticity formed at the near-field shear layer due to the Kelvin-Helmholtz instabilities diffuse bilaterally and reaches the centerline to disrupt the potential core. For the isothermal jet of practice at the studied flow conditions, the characteristic distance of $0<z/D<5$ for moderate Reynolds numbers and $0<z/D<8$ for high Reynolds numbers is recommended as the span for which Eq. 4-8 is applicable.

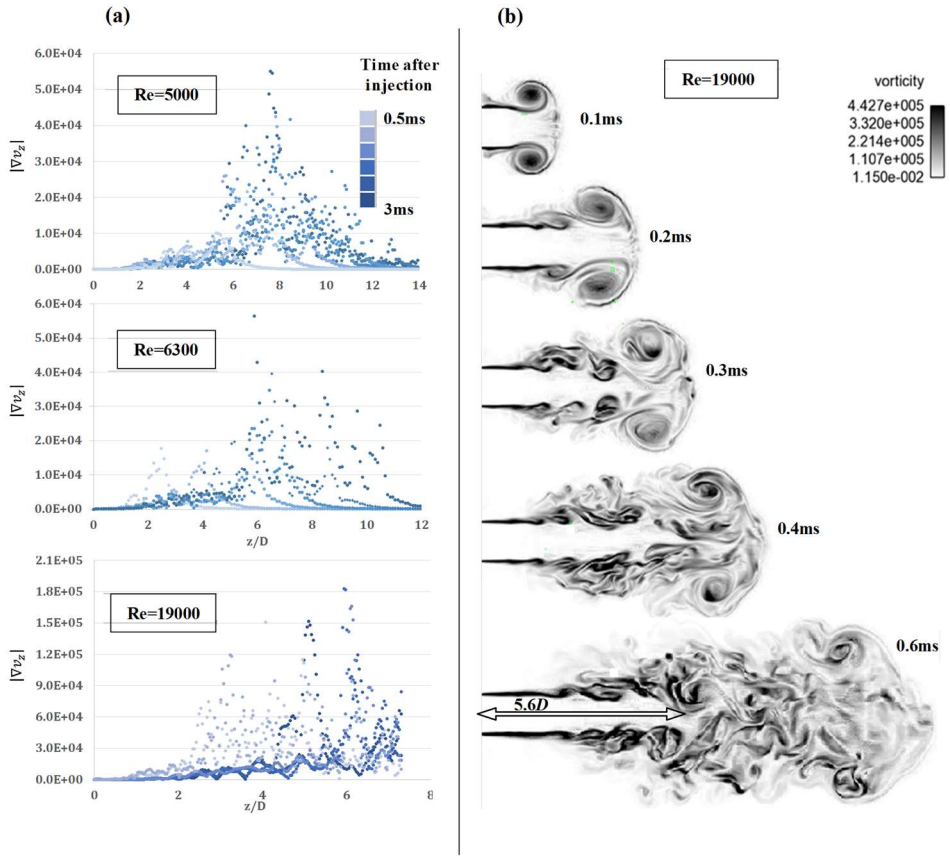

Figure 4-9: (a) Development and termination of the velocity potential core measured by velocity gradients, and (b) vorticity plot at Re=19,000

4.6 Conclusion

In this work, the exact solution for the momentum equation was sought to address the evolution of the velocity field of a turbulent suddenly-started round jet in the region near the orifice where the velocity potential core is still extant. The near-field behavior of the turbulent jet permits the co-flow analogy and the assumption of negligible transverse velocity. Two sets of solutions (inner and outer) were produced to separately treat the diffusion of the turbulent mixing layer on both sides of the shear interface. The inner and outer empirical parameters for the model at Re=12800 were determined to be $\Omega_{in} = 0.360\ s^{-1}$ and $\Omega_{out} = 0.102\ s^{-1}$. Employing the designated turbulent diffusion parameters, the model demonstrated satisfactory agreement in predicting the near-field velocity profile during the developing stage of the momentum potential core. The model also established analytical means to predict the rate of mass entrainment as a

function of time and jet radius, until the head vortex pinch-off occurs. Comparison of the non-dimensional entrainment ratio,ψ, shows the dependence of this value to the jet tip position in the form of $\psi = \psi(z^{1.41})$. Large eddy simulation of the transient turbulent jet is also conducted to examine the deviation of predicted values of entrainment ratio from the values of well-resolved turbulent jet. The analytical model no longer applies after the pinch-off process disturbs the centerline velocity. It is suggested that for moderate Reynolds numbers between 5000 and 19800, the spatial range of model validity is z/D=5 and z/D=8, respectively, where the potential core is not yet perturbed by the induced instabilities of the shear layer.

4.7 Funding sources

This work was partially supported by the US National Science Foundation under Grant No. CBET-1235696, and partially supported by Indiana University – Purdue University Indianapolis.

5. ANALYTICAL AND NUMERICAL STUDY OF NEAR-FIELD IGNITION OF H_2/AIR BY INJECTION OF HOT GAS

5.1 Abstract

Ignition initiation by a turbulent hot jet involves complex transport and chemical processes with disparate and sensitive time scales. Its understanding is important for improved ignition in advanced and novel combustion engines and in ignition avoidance for explosion safety measures. This study is aimed at the modeling of turbulent jet ignition for mixtures with fast chemistry relative to the large-scale mixing time scales. The evolution of jet mixture fraction in the near-field shear layer of a suddenly-starting turbulent jet is analytically modeled and calibrated by large-eddy simulation of the reacting fluid. When integrated with a correlation for instantaneous chemical induction time, the model estimates the radial location and the timing of ignition as the jet travels in the streamwise direction. The calculation of chemical induction time includes accounting for the role of the scalar dissipation rate in the suppression of ignition. A comparison of ignition delay for various injection temperatures and ambient fuel-air ratios shows strong dependence of ignition penetration rate on equivalence ratio and weak dependence on the injection temperature. Finally, the limitations of the present model are investigated by assessing the regions of mixing layer where strong diffusive transport collocates with the high production rate of active radicals.

5.2 Introduction

Deflagration initiation by injection of turbulent hot gas into a mixture of fuel and air enables lower emissions and higher efficiency without knock in internal combustion (IC) engines [45], and rapid ignition in wave rotor combustors [38]. Understanding of such turbulent jet ignition (TJI) is also important for explosion protection and fire safety when an escaping jet of reactants is inadvertently released into an oxidizing environment. For example, there have been many incidents of spontaneous leakage from high-pressure hydrogen tanks and subsequent ignition [135]. In ultra-lean, low-NOx operation of IC engines, the hot turbulent jet is employed as an alternative to direct-spark ignition for better ignition controllability and mitigation of cycle-to-cycle variability [42, 136]. The hot gas jet is typically generated by burning fuel/air mixture in a separate small pre-chamber forming high-pressure products, which in turn penetrate into and ignite the

main chamber [47]. Understanding the rapid mixing between the hot jet and surrounding reactant gases is crucial to predicting ignition. Ignition is the result of partial mixing of the hot jet and cold reactants creating regions where the thermochemical composition and temperature in the mixing layer is supportive of fast kinetic rates [3]. In a starting turbulent jet, mixing occurs in the jet near-field by the turbulent diffusion of energy/mass in shear layer [137]. As vorticity accumulates in the shear layer, Kelvin-Helmholtz instabilities rapidly grow in the shear layer enhancing the small-to-medium-scale diffusion mixing [138]. The leading vortex ring of the jet experiences much larger scale mixing due to the engulfment of surrounding gases in the large toroidal recirculation zone [53, 133].

One of the critical factors for TJI effectiveness is the magnitude of the chemical time scale relative to the mixing time scale, which may be expressed as a Damkohler number, if the controlling convective or diffusive transport time is identified as the mixing time scale. Biswas et al. [84] showed that TJI generally occur in the thin reaction zone for both methane-air and hydrogen-air ignitions. Their study declares a limiting Damkohler number for ignition below which no ignition ensued.

Feyz et al. [2] suggest that for high-reactivity fuels in the main chamber that exhibit short chemical time scales, ignition heat release occurs through a flame propagation mechanism, highlighting the further role of turbulent diffusivity in the ignition process [2]. For fuels with relatively fast chemistry, the ignition occurs within the jet near-field and quickly extends to the frontal area of the jet where turbulent mixing at large scales governs the ignition [139]. Fink and Vanpee [10] discuss the role of fuel type on the axial distribution of the ignition, and Feyz et al. [3] discuss the effect of fuel reactivity on the radial ignition distribution. The subject of ignition in the jet near-field is most relevant for fuels with a short chemistry time scale, for instance, hydrogen. In such cases, the chemical and turbulent diffusion time scales may be comparable.

Many studies have addressed hydrogen ignition in a main combustion chamber by pre-chamber generated hot gas [14-16, 54, 86, 140-142]. Ghorbani et al. [15] considered the nozzle diameter effects on the ignition delay through its impact on the shear-generated turbulence in the jet near-field and on heat dissipation. In a comprehensive numerical study of Carpio et al. [11], the role of main-chamber equivalence ratio and the jet velocity on the critical ignition radius is studied in an axisymmetric domain. They highlighted the role of flow residence time, i.e. the ratio of jet penetration length to the jet velocity, on the balance between chain-branching to chain-terminating

reactions, which is imperative to ignition success. From the observations of Ghorbani et al. [15] on H radical distribution, and the results of Carpio et al. [11] on the relationship between residence time and ignition success, it appears that ignition fails unless there is sufficient production of active radicals in the shear mixing layer. Multiple studies [11, 13, 15] on the jet ignition of hydrogen emphasize the importance of understanding the short-time scale transport process in the shear layer for better ignition predictability.

The mathematical solution of the governing equations for the reacting mixing layer enables a better understanding of the near-field ignition phenomenon. In a fundamental study of reacting mixing layer, Law et al. [105] analytically studied the ignition process in a laminar, steady-state premixed reactant stream which flows in parallel with a hot gas stream. They showed that the ignition is minimally dependent on the velocity of cold stream, which allows the use of iso-velocity assumption. This work also suggested that the ignition initiation occurs from the reactant-poor but hotter end of the mixing zone. A comprehensive study of ignition and deflagration of diffusion flames using the asymptotic analysis of unsteady reacting counter-flows has been done by Linan and Crespo [143]. Their work is of significant importance to TJI study as they showed that the ignition occurrence depends on *i)* the difference between initial temperature of two streams, and *ii)* the magnitude to which the highest initial temperature differs from adiabatic flame temperature.

Feyz et.al [2] reported that ignition kernels that are originally formed in the near-field shear layer can be transported to the downstream and induce ignition in the leading section of the jet. These kernels may be quenched due to heat loss or lead to sustained ignition in the vortex ring of the starting jet.

The present study combines analytical and numerical approaches to study the ignition development in the near-field of a suddenly-started turbulent hot jet. An analytical approximation of the transport process based on a transient one-dimensional jet model in conjunction with an Arrhenius-type chemical induction model are employed to characterize the timing and radial location of ignition in the growing shear layer. Large-eddy simulation of the starting TJI is also utilized for analytical model calibration and defining the applicability range of the model. This investigation is motivated by the significance of shear-layer transport phenomenon in ignition process of fuels with very fast chemistry.

5.3 Methods

5.3.1 Boundary layer solution

The diffusive transport process at the jet near-field as shown in Figure 5-1 is characterized in this section, using both Eulerian and Lagrangian viewpoints. The aim is to predict the radial diffusion within a circular plane that contains a group of jet fluid parcels which are initially issued with a known composition and high temperature. The jet parcels leave the nozzle at the time origin and are assumed to move in the streamwise direction with the jet initial velocity. As the parcels advance, the diffusive exchange of energy and mass with cold reactants occur radially and form a mixing boundary layer that can potentially host ignition. The growth rate of the mixing layer thickness is controlled by the turbulent diffusivity. Although the diffusion coefficient may be spatially varying in real practice, in this study the effective diffusion coefficient is treated as constant for mathematical simplicity. In order to identify the local ignition, the analytical solution of the transport equation is then integrated with a proposed global expression to obtain chemical induction time.

Assuming the analogy between heat and mass transport prior to ignition, the conservation of species and energy for the non-reacting flow (no chemical source term) is given by Eq. 5-1,

$$\rho \frac{\partial \alpha}{\partial t} + \rho u . \nabla \alpha = \nabla . (\rho D \nabla \alpha) \qquad \text{Eq. 5-1}$$

where D is a constant diffusivity, and u is the velocity vector. Assuming Lewis number of unity ($\frac{k}{\rho c_p} = 1$), α in Eq. 5-1 is a generalized scalar stands for jet mixture fraction (f) and normalized temperature $\frac{T-T_\infty}{T_0-T_\infty}$, where T_0 is the injection temperature and T_∞ is the far-field temperature. In this study, the jet mixture fraction is defined as the fraction of the nozzle-originated fluid in the total fluid. The following assumptions are made: (*i*) The gas is incompressible, (*ii*) the transverse velocity is negligible in the jet near-field, and (*iii*) the gradient of scalars in streamwise direction is negligible. The mass continuity equation allows ρ to appear before the derivatives in the left-hand side of Eq. 5-1. Assuming the constant value of ρD, the density can be canceled out from both sides of the equation.

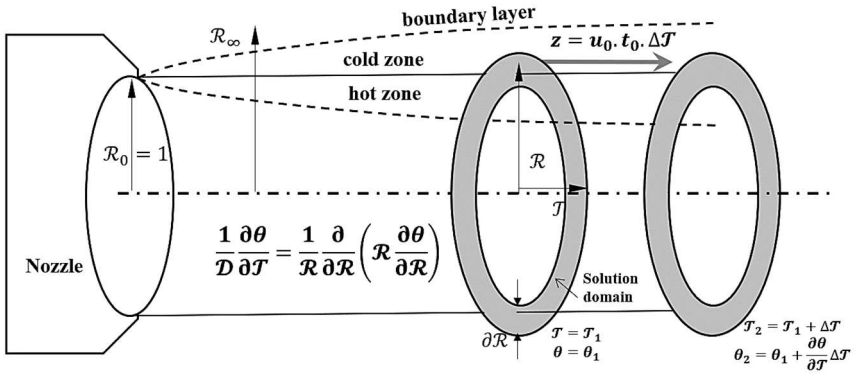

Figure 5-1: Schematic of the transient 1-D domain and corresponding representation of the axisymmetric starting jet.

Compressibility effects are neglected due to the high speed of sound within the hot jet relative to the jet velocity [11], and the slender shear layer justifies neglect of axial gradients relative to radial gradients. Negligibility of the transverse velocity has been verified by a scale study of the relevant terms in the equation for jet mixture fraction in the near-field, which showed that the advective term could be up to two orders of magnitude smaller than diffusive term. Figure 5-2 shows the result of the large eddy simulation of the starting jet, which will be described in section 5.3.3., to compare the magnitude of the convective and diffusive terms in Eq. 5-1.

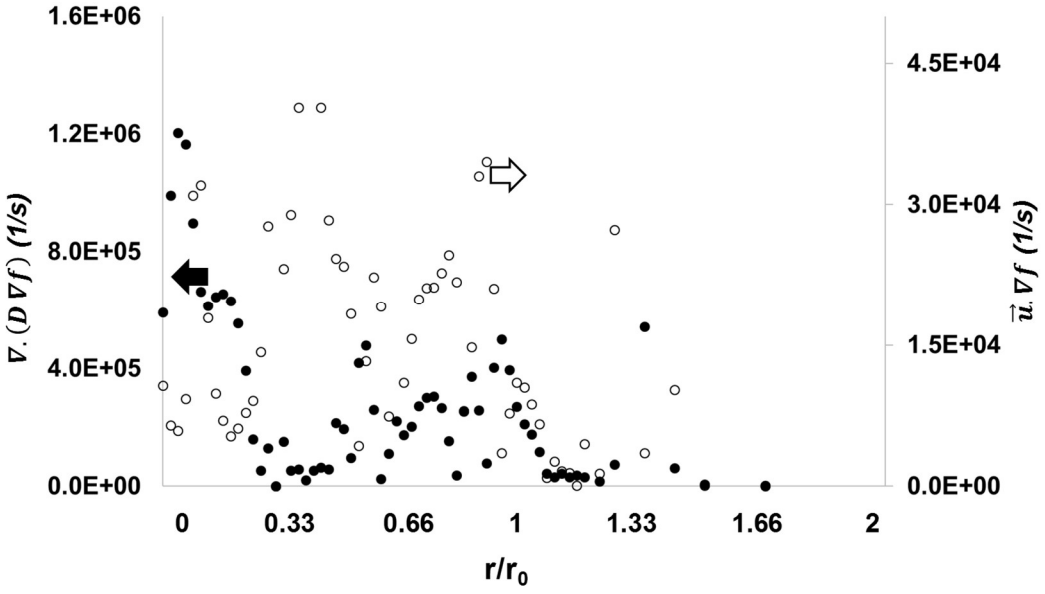

Figure 5-2: The radial distribution of the diffusion term (left axis, solid bullet) and the advective term (right axis, hollow bullet) with different axis scales to show the general

The assumptions yield to the reduced form of Eq. 5-1 in the cylindrical coordinate, which now has no dependence on the axial coordinate and velocity field:

$$\frac{1}{D}\frac{\partial \alpha}{\partial t} = \frac{1}{r}\frac{\partial}{\partial r}\left(r\frac{\partial \alpha}{\partial r}\right) \qquad \text{Eq. 5-2}$$

In order to generalize the solution, parameters of Eq. 5-2 are non-dimensionalized using arbitrary characteristic time and lengths scales, as follows,

$$\frac{1}{\mathcal{D}}\frac{\partial \alpha}{\partial \mathcal{T}} = \frac{1}{\mathcal{R}}\frac{\partial}{\partial \mathcal{R}}\left(\mathcal{R}\frac{\partial \alpha}{\partial \mathcal{R}}\right) \qquad \text{Eq. 5-3}$$

where $= D\frac{t_0}{{r_0}^2}$, $\mathcal{T} = t/t_0$, and $\mathcal{R} = r/r_0$. In the present study, the characteristic time (t_0) and length scale (r_0) are 10 ms and 1.5 mm, respectively. The characteristic scales for the solution parameters are opted based on the geometrical properties of the nozzle and integral structures of the flow. This governing equation will be solved with different simplifications in each of the two zones that are separated by the initial boundary discontinuity of the emerging jet at $\mathcal{R}$ = 1. To homogenize the initial condition of Eq. 5-3, we use the change of variable $\theta = \alpha - \alpha_0$, where α_0 is the initial generalized scalar in each zone. With the new variable, the transport equation then becomes,

$$\frac{1}{\mathcal{D}}\frac{\partial \theta}{\partial \mathcal{T}} = \frac{1}{\mathcal{R}}\frac{\partial}{\partial \mathcal{R}}\left(\mathcal{R}\frac{\partial \theta}{\partial \mathcal{R}}\right) \qquad \text{Eq. 5-4}$$

The solution of Eq. 5-4 describes the time-dependent one-dimensional radial diffusion between a circular domain $0 < \mathcal{R} < \mathcal{R}_0$ with uniform value of θ at $\mathcal{T}$ = 0 and a surrounding semi-infinite plane $\mathcal{R} > \mathcal{R}_0$ with a different initial value. As shown in Figure 5-1, the inner "hot zone" takes initial values from the nozzle fluid where $\alpha = 1$, while the "cold zone" takes initial values from the main chamber where $\alpha = 0$. As the solution advances in time, jet mixture fraction profiles are developed, and the scalars diffuse between the hot and cold zone in a circular plane.

Due to the initial discontinuity at the interface zones ($\mathcal{R} = \mathcal{R}_0$), the solution for each zone must be sought individually. The value at the interface as a for $\mathcal{T} > 0$ is specified to ensure the continuity of the scalar and conservation of the flux over the boundary. Inspired by the transient solution in lumped bodies, the general value of the boundary at $\mathcal{R} = \mathcal{R}_0$ is prescribed as:

$$\theta_I(\mathcal{T}) = C_1 exp(-C_2\mathcal{T})$$

where θ_I is the interface value, and C_1 and C_2 are empirical constants. One of the methods used to solve problems with varying boundary is to use Duhamel's superposition integral [144]. In this method, the solution of an auxiliary problem with a constant boundary condition is employed to

construct the solution to the same problem with a time-varying boundary condition. In the present case, the boundary value is described by $\theta_I(\mathcal{T})$. Thus, the contribution of this boundary to the main solution is

$$\theta(\mathcal{R},\mathcal{T}) = \theta_I(0)\bar{\theta}(\mathcal{R},\mathcal{T}) + \sum_{i=1}^{n} \Delta\theta_I(e_i)\bar{\theta}(\mathcal{R},\mathcal{T}-e_i) \qquad \text{Eq. 5-5}$$

where $\bar{\theta}(\mathcal{R},\mathcal{T})$ is the unique solution of a problem with constant boundary value and zero initial condition, and $\theta_I(0)$ is the initial value of the boundary. e_i indicates the time at which $\Delta\theta_I(e_i)$ occurred. In the present work, $\bar{\theta}(\mathcal{R},\mathcal{T})$ is obtained for the hot and cold regions with the constant interface value set to the average of initial values. Also $\theta_I(0)$ is assumed to be one. Now that the solution method for time-dependent interface boundary is established, we can develop the solution, $\bar{\theta}(\mathcal{R},\mathcal{T})$, of Eq. 5-4 for each zone assuming a constant interface value.

Hot zone: The solution for the hot zone is sought by the method of separation of variables (SOV) in cylindrical coordinates [145]. The initial and boundary conditions for the hot zone are

$$\left(\frac{\partial\bar{\theta}}{\partial\mathcal{R}}\right)_{\mathcal{R}=0} = 0, \qquad \bar{\theta}(\mathcal{R}_0,\mathcal{T}) = -0.5, \qquad \bar{\theta}(\mathcal{R},0) = 0$$

which yields to the final solution for Eq. 5-4 on the hot region as:

$$\bar{\theta}(\mathcal{R},\mathcal{T}) = \bar{\theta}(\mathcal{R}_0,\mathcal{T})\left[1 - \frac{2}{\mathcal{R}_0}\sum_{m=1}^{\infty} e^{-\mathcal{D}_H\beta_m^2\mathcal{T}}\frac{J_0(\beta_m\mathcal{R})}{\beta_m J_1(\beta_m\mathcal{R}_0)}\right] \qquad \text{Eq. 5-6}$$

where $\mathcal{D}_H$ is the effective diffusion coefficient in the hot zone, J_0 and J_1 are zeroth and first-order Bessel functions, and β_m are the roots of $J_0(\beta_m\mathcal{R}_0) = 0$. Numerical examination of Eq. 5-6 suggests that it is sufficient to sum the first twenty terms.

Cold zone: The domain for the cold region is a semi-infinite plane ($\mathcal{R}_0 < \mathcal{R} < \infty$) that initially exists at α=0. Since the method of SOV is not conveniently applicable to infinite domains, Eq. 5-4 can be solved using the method of similarity by which it is reduced to an ordinary differential equation. The similarity method is utilized to combine radial location and time into a new variable $\xi = \frac{\mathcal{R}}{\sqrt{4\mathcal{D}_C\mathcal{T}}}$ where $\mathcal{D}_C$ is the effective diffusion coefficient of the cold zone. The transport equation in ξ space and the corresponding boundary conditions are written as:

$$\frac{d^2\bar{\theta}}{d\xi^2} + \frac{1+2\xi^2}{\xi}\frac{d\bar{\theta}}{d\xi} = 0 \qquad \text{Eq. 5-7}$$
$$\bar{\theta}(\mathcal{R}_0,\mathcal{T}) = 0.5, \quad \mathcal{R}\to\infty : \bar{\theta} = 0, \qquad \bar{\theta}(\mathcal{R},0) = 0$$

By reducing the order of the derivatives, the solution of Eq. 5-7 is:

$$\bar{\theta}(\xi) = A\int_{\xi}^{\infty}\frac{e^{-\lambda^2}}{\lambda}d\lambda + B \qquad \text{Eq. 5-8}$$

where $A = \frac{\bar{\theta}(\mathcal{R}_0,\mathcal{T})}{\int_{\xi_I}^{\infty}\frac{e^{-\lambda^2}}{\lambda}d\lambda}$ and $B = 0$, obtained from the boundary conditions. The lower limit of the integral in the denominator represents ξ at $\mathcal{R}_0$ i.e. $\xi_I = \frac{\mathcal{R}_0}{\sqrt{4\mathcal{D}_C\mathcal{T}}}$.

When the Eq. 5-5, Eq. 5-6 and Eq. 5-8 are combined, they comprise a time-varying scalar profile that extends from the jet centerline to the jet far-field. This solution represents the diffusion process of a group of parcels that are ejected from the nozzle and move in the streamwise direction. Due to the absence of advective terms in the simplified transport equation (Eq. 5-4), the temporal velocity variation of parcels may not affect the transport process. The study of Law et al. [105] asserts the negligible dependence of ignition on the velocity distribution. This supports the use of the solution of Eq. 5-4 to describe the temporal state of a starting jet during the injection. In Figure 5-1, z is the displacement of parcels issued from the nozzle, which represents the jet advancement over certain elapsed time $\Delta\mathcal{T}$.

5.3.2 Ignition model coupling

The boundary solution proposed in section 5.3.1 assumes transient diffusion in non-reacting flow and lacks any source/sink terms. Ignition delay is estimated by applying the nodal temperature and species concentrations for the hot and cold zones obtained from Eq. 5-5 to an Arrhenius-type autoignition correlation to predict the evolution of chemical induction time. As a single jet parcel observed in a Lagrangian frame undergoes change of temperature and composition due to a diffusive process, it experiences chemical changes, including production of initiating radicals. Its temperature and composition at every time instant corresponds to an instantaneous ignition progress rate characterized by a certain 'instantaneous' induction time, if those properties were fixed. For the present study, the general form for the instantaneous chemical induction time of hydrogen-air is introduced as,

$$\tau_{ch} = A\,[H_2]^a[O_2]^b\exp(E/RT) \qquad \text{Eq. 5-9}$$

where τ_{ch} is the chemical induction time from adiabatic shock-tube experiments. For a wide range of H_2/O_2 ratios, White and Moore [146] as reported by Cheng and Oppenheim [147] proposed the following values for the parameters in the above correlation,

$A = 1.58 \times 10^{-11}\ (cm^3/mol)^{a+b}(\mu s), a = -0.33, b = -0.66, E = 17.19\ (kcal/mole)$

Chemical reactions are computed only above the lower flammability limit of hydrogen to be Y_{H2}=0.0038 (mass fraction) [148] for a mixture initially at standard room conditions.

This adiabatic chemical induction time must be corrected for heat dissipation in the shear layer, which will slow the progress to ignition. The instantaneous scalar dissipation rate (SDR) is a useful measure of quenching by heat loss. Physically, SDR (χ) can be interpreted as a diffusion characteristic or the inverse of heat dissipation time scale ($\tau_{di} = 1/\chi$).

A multiplier is used with Eq. 5-9 to reflect the corrected instantaneous induction time.

$$\tau_a = \tau_{ch}(1 + t_0\chi) \qquad \text{Eq. 5-10}$$

The functional dependence of χ on f is selected to be an error function profile which anchors on a known reference value of scalar dissipation (χ_{ref}) at an arbitrary jet mixture fraction (f_{ref}) [149]. The scalar dissipation rate is then described by the following expression:

$$\chi = \chi_{ref}\frac{exp\{-2[erfc^{-1}(2f)]^2\}}{exp\left\{-2\left[erfc^{-1}(2f_{ref})\right]^2\right\}}.$$

By scale analysis, it is known that at $f_{ref} = 0.5$, scalar dissipation is $\chi_{ref} = \frac{D}{4\,(r_0)^2}$, where D is the effective diffusion coefficient and r_0 is the nozzle radius.

In a transient hot jet injection, the corrected chemical induction time of Eq. 5-10 changes during the transient diffusion process. Ignition of the moving parcel is attained through cumulative progress towards ignition over some elapsed time after injection of the parcel. To account for the effect of changing conditions on the overall ignition delay time, the following integral relation is used as ignition criterion

$$\int_{t=0}^{\tau_{id}}(1/\tau_a)dt = 1 \qquad \text{Eq. 5-11}$$

where for each specific parcel of the jet, τ_{id} is the overall ignition delay time, τ_a is the instantaneous induction time, and t is the elapsed time after the injection of the parcel. Figure 5-3 depicts the dependence of the chemical and corrected induction time on the jet mixture fraction. As expected, the corrected induction time (τ_a) exhibits longer delay compared to the chemical induction time (τ_{ch}) due to the deterrent effect of scalar dissipation rate in prolonging the ignition. Figure 5-3 also shows the occurrence of minimum induction time in the rich zone of jet mixture fraction (f≈0.8) which corresponds to the hot zone of the jet. This observation is consistent with the findings of Law et al. [105] in which ignition is reported near the hot boundaries.

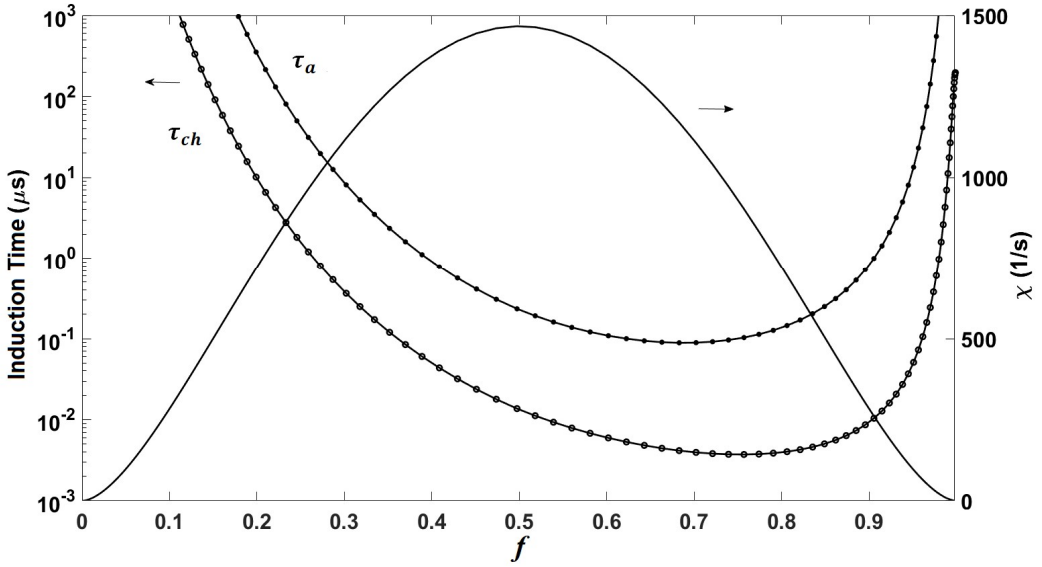

Figure 5-3: Distribution of instantaneous induction time and scalar dissipation rate in the jet mixture fraction space

5.3.3 Large-eddy simulation

Large-eddy simulation (LES) of the reacting flow is conducted aiming to calibrate the analytical ignition model and assess its performance within a certain spatial range. The simulation used the CONVERGE (v 2.4) code which is a multi-physics computational fluid dynamics solver [24]. The reacting fluid is described by the Favre-filtered formulation of continuity, momentum, species and energy equations in compressible form, details of which are reported in [3]. Closure of the momentum equation at the sub-grid scale (SGS) is obtained by using the dynamic structure model to approximate the stress tensor at the SGS level [63, 64]. The eddy viscosity approximation for diffusion at SGS is employed for the mass and energy transport equations [65]. Time integration is based on the "Crank-Nicolson" scheme with second-order accuracy combined with a dynamic timescale algorithm with varying time-steps in the range 10^{-7}-10^{-8} s. The spatial derivatives of Euler fluxes in the transport equations are computed with second-order accuracy.

The computational domain is a long rectangular box with a circular orifice with ⌀=3mm diameter attached to the left end-wall. The side and length ratios of the constant-volume chamber are W/⌀=10 and L/⌀=100, respectively, with equal width and height. The starting turbulent jet is assumed to emerge from the nozzle at time zero with a fixed velocity of 360 m/s at 1350K. The jet

chemical composition is set to the complete combustion products of stoichiometric H_2-air, without accounting for minor species and radicals in the jet. The adiabatic combustion chamber is initialized to quiescent stoichiometric H_2-air at 0.4 MPa and standard temperature. Stoichiometric hydrogen-air mixtures have short chemical time scales and tends to experience ignition in the near-field shear layer, which is the focus of this work. The mixture composition of the main chamber and the jet temperature are also specifically adopted for comparison from the work of Biswas et al [84] in which they investigated the pre-chamber ignition of H_2-air mixtures using high-speed Schlieren and OH chemiluminescence imaging.

The numerical grid incorporates a uniform base mesh size of 0.5 mm which is reduced by three embedding levels using the Adaptive Mesh Refinement (AMR) algorithm. The refinement is automatically applied to the regions in the flow where velocity and temperature gradients exceed a determined threshold. With the aid of AMR, minimum cell size of $\delta_x = 62\ \mu m$ is attained at the reaction zone, which is sufficiently fine to resolve the species and temperature gradients of the ignition kernels. The calculated Reynolds number at the jet temperature yields $Re_{U/2,D_{orif}} = 3025$. Thus, the estimated Kolmogorov scale approximately is $\eta \approx D_{orif} Re^{-\frac{3}{4}} \approx 7\ \mu m$ where the largest flow structure is considered to be the orifice diameter. This value implies the flow resolution to be $\frac{\delta_x}{\eta} \approx 9$ which is comparable with the grid resolution of the work of Karaca et al. regarding LES of supersonic H_2-air combustion acceptable [150]. Analysis of turbulent kinetic energy spectra by the authors for this case demonstrates the ability to resolve more than 85% of the turbulence kinetic energy with this mesh resolution. Grid refinement and validation for a very similar computational case are discussed in prior studies of the authors [2-4].

Detailed finite-rate chemistry calculations are performed with a partially-stirred reactor model (PaSR) to account for subgrid-scale turbulence-chemistry interaction. In this approach, a computational cell is assumed to comprise two zones; a perfectly-stirred reactor, and a chemically inert zone. The mass fraction of the reacting zone (σ) is represented as a function of chemical and mixing time scales [151],

$$\sigma = \frac{\tau_c}{\tau_c + \tau_{mix}} \qquad \text{Eq. 5-12}$$

where τ_c and τ_{mix} are the characteristic chemical and mixing time scales, respectively. Characteristic chemical time scales are derived from a detailed model for hydrogen oxidation kinetics by O'Connaire et al. [152] that had been verified over a wide range of temperature (298-

2700 K), pressure (0.05 to 87 atm), and equivalence ratio (0.2 to 6). The mixing time scale is estimated from the work of Forney & Nafia [153] as:

$$\tau_{mix} = C_{mix}\sqrt{\frac{\mu_{eff}}{\rho\varepsilon_d}}$$

where ρ is density, ε_d is eddy dissipation rate, μ_{eff} is effective dynamic viscosity, while C_{mix} is a constant equal to 0.001. The chemical reaction rates in each cell are adjusted by the following expression:

$$\dot{\omega} = \sigma\dot{\omega}_0 \qquad \text{Eq. 5-13}$$

where $\dot{\omega}_0$ is the reaction rate of a perfectly-stirred reactor with same the properties as the cell and all of its mass. Turbulence-chemistry interaction has been modeled using the partially-stirred reactor model in various LES studies of combustion [154-156]. Figure 5-4 shows a comparison between the heat release rate (HRR) field produced by the present LES with the chemiluminescence image of experimental OH^* radical mass fraction [84]. Two distinguished regions of heat release occur as the free jet evolves; shear layer and leading vortex ring. The near-field shear layer of the jet supports relatively lower heat-release intensity as the reaction sites are subject to strong shear dissipation. The significance of the reactions in the near-field of the nozzle is to facilitate further ignition in the jet vortex. As the vortex ring allows for higher residence time, the reaction in the activated fluid particles formed in shear layer can reach completion.

Assuming that HRR can be represented qualitatively by the emergence of OH^*, it is observed that the simulation results could capture the global ignition delay time close to the experimental measurements. This implies the ability of the simulation in modeling the effective mixing and chemical time scales. However, due to the differences in the enclosure size, and the velocity history at the inlet boundary, the spatial distribution of the reaction zone is not perfectly replicated by the current LES. In addition, a better agreement between simulated and experimental jet structure will be acquired if the velocity history at the nozzle is represented accurately in the model. Figure 5-4 also illustrates the grid refinement in the region that is prone to high shear and reaction rates. The thickness of reaction zone is resolved by at least 10 computational cells.

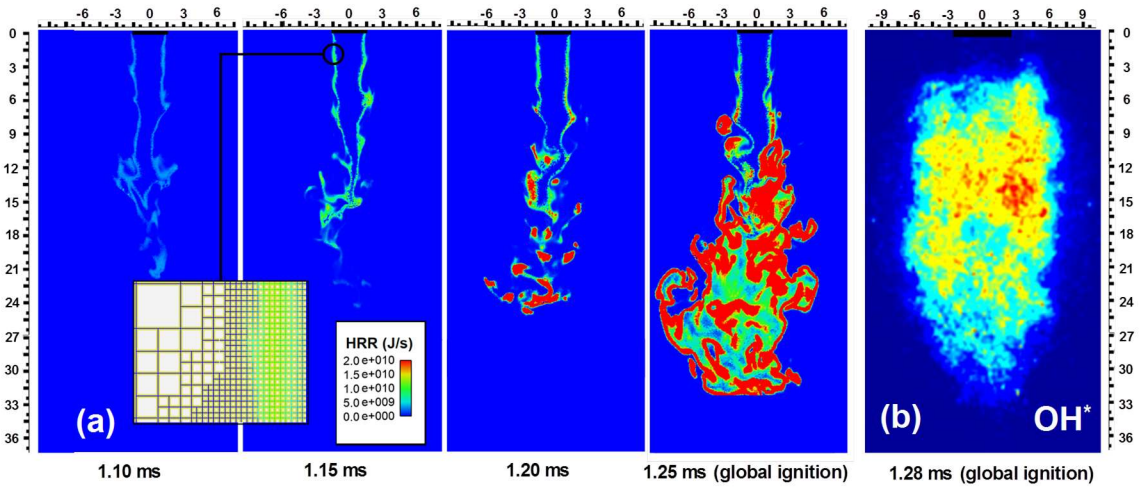

Figure 5-4: Comparison of distribution of heat release rate (a) obtained in present LES with experimental distribution of OH* measure by Biswas et al. (b). Units are in millimeters.

5.4 Model calibration and predictions

5.4.1 Model calibration

The solution obtained by Eqs. 6 and 8 address the hot and cold zones independently which allows the model to accommodate different turbulent diffusion coefficient ($\mathcal{D}$) for each region. The jet mixture fraction profiles provided by the combination of Eq. 5-5, Eq. 5-6 and Eq. 5-8 are compared against the spatially averaged LES results. Figure 5-5 shows the evolution of radial distribution of jet mixture fraction at different instants after the start of injection. Based on the argument made in Section 5.3.2. regarding the moving group of parcels, we may interpret the solution of transport equation as the evolution of flow properties in a circular plane that moves with jet velocity in the streamwise direction. As seen in Figure 5-5, the jet mixture fraction is initially at unity at the axis and asymptotically goes to zero in the jet far-field, preserving continuity at $\mathcal{R} = 1$.

Its prescribed value at the interface is $\theta_I(\mathcal{T}) = C_1 exp(-C_2\mathcal{T})$ where C_1 is 0.1 and C_2 is 108. These values are obtained in an iterative process to ensure the continuity of scalar gradient at the interface, assuming diffusivity coefficient at the vicinity of the interface is relatively uniform. For best fit of $\theta(\mathcal{R},\mathcal{T})$ to the radial distribution of jet mixture fraction obtained by LES, the non-

dimensional effective diffusion coefficients are set as different constants, $\mathcal{D}_H = 30$ and $\mathcal{D}_C = 293$ for all $\mathcal{T}$. The relatively large value of $\mathcal{D}_C$ is likely due to transport enhancement by vortices shed by the shear layer into the cold zone, as well as the presence of hydrogen with high molecular diffusivity. The jet mixture fraction profile remains everywhere within the bounds set by the jet source and far-field. As observed in Figure 5-5, the diffusion thickness stretches on each side of the shear interface in proportion to the designated turbulent diffusion coefficient $\mathcal{D}$. The values of diffusion coefficients mentioned in Figure 5-5 are the same for all cases in this study. The imbalance of scalar flux at the interface of the hot and cold zones is consistent with our initial simplifying assumption that neglects the axial advection and its role in export of the scalars from the studied control volume.

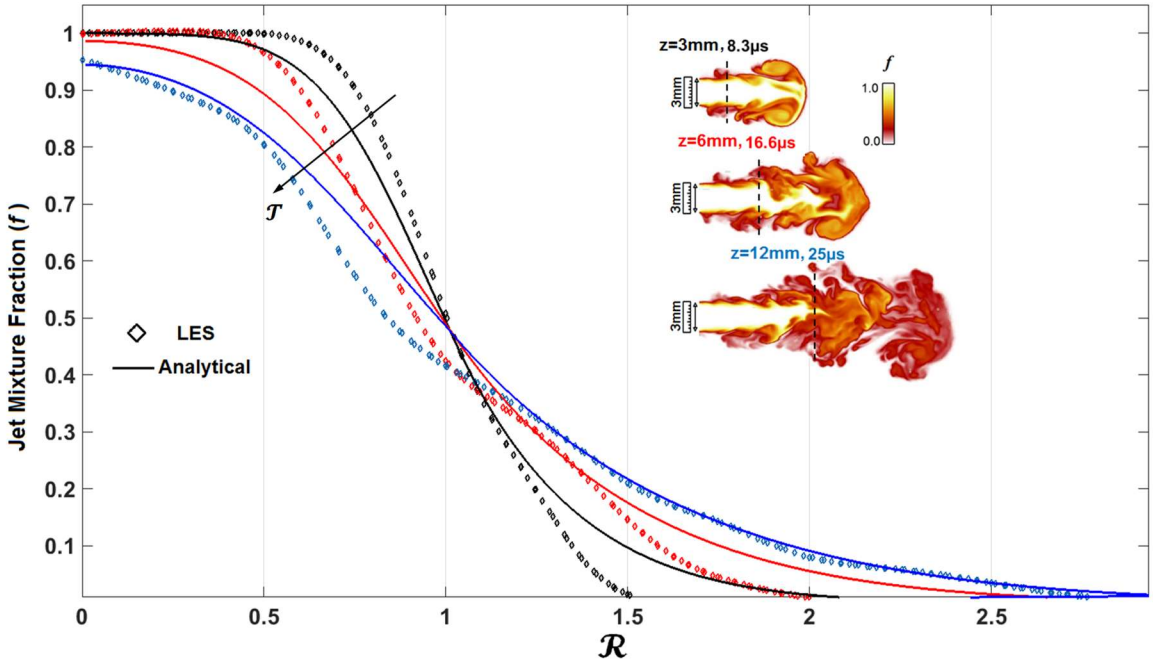

Figure 5-5: Comparison of modeled transient jet mixture fraction profiles (solid lines) with LES (◇) requires $\mathcal{D}_H = 30$, $\mathcal{D}_C = 293$. The profiles are shown for $\mathcal{T}_1 = 8.3 \times 10^{-4}$ (black), $\mathcal{T}_2 = 16.6 \times 10^{-4}$ (red), and $\mathcal{T}_3 = 25 \times 10^{-4}$ (blue)

With the fields of jet mixture fraction and temperature established, Eq. 5-10 allows for the calculation of the instantaneous chemical induction time of each parcel. Figure 5-6 illustrates the temporal variation of instantaneous induction time and SDR due to the transient diffusion of the jet mixture fraction. The chemical induction time is large near the centerline where reactants are absent and in the far-field where temperature is low. As reactants diffuse radially inward, the

chemical induction time decreases rapidly due to the exponential effect of temperature, as long as concentrations remain adequate. Thus, the chemical induction time is shortest in the vicinity of the jet interface ($\mathcal{R} = 1$). However, the countering effect of scalar dissipation rate on prolonging the ignition is also most accentuated at the vicinity of the jet interface, which is influential in determining the local induction time. It is also noted from Figure 5-6 that as time passes the lowest local induction time migrates away from the high-shear zone with maximum SDR.

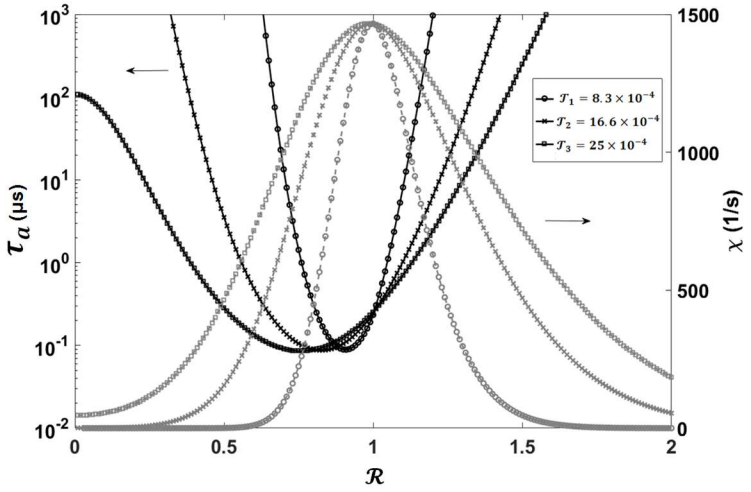

Figure 5-6: Radial distribution of the instantaneous induction time and SDR for various time instants after the injection

5.4.2 Ignition penetration

Upon the injection of the transient hot jet, the near-field shear layer undergoes transverse turbulent diffusion of species and temperature in opposite directions. As a typical jet parcel moves in the streamwise direction it experiences varying temperature and concentration history that induce varying rates of chemical reaction, possibly leading to ignition of the parcel. Our approach to deduce the overall ignition time from summation of instantaneous induction times has been elaborated in Section 5.3.2. When ignition is determined to have occurred at a given radius, that radial coordinate will be identified as the onset location of the reaction zone, and the elapsed time will be introduced as the ignition delay time of that parcel. The penetration of ignition onset in the shear layer as time proceeds, measured by the analytical and LES models, is shown in Figure 5-7. While the analytical model uses Eq. 5-13, for LES the advent of HO_2 radical is used to identify the ignition onset. It is seen from Figure 5-7 that the ignition onset exhibits a delay after injection

due to the inherent chemical induction time. This initial time delay is captured by LES and the analytical model of ignition. The prediction of the radial ignition location by the analytical model is in good agreement with the LES prediction for intermediate times until $\mathcal{T} = 5 \times 10^{-3}$. The non-linear physics of the turbulent structures that develop at later times are not represented by the present analytical model. The migration of the ignition onset towards the jet centerline is a substantial observation that agrees with the tendency of ignition progression shown by LES. Law et al. [105] discuss how the temperature sensitivity of reactions to the Arrhenius factor favors ignition near the hot boundary.

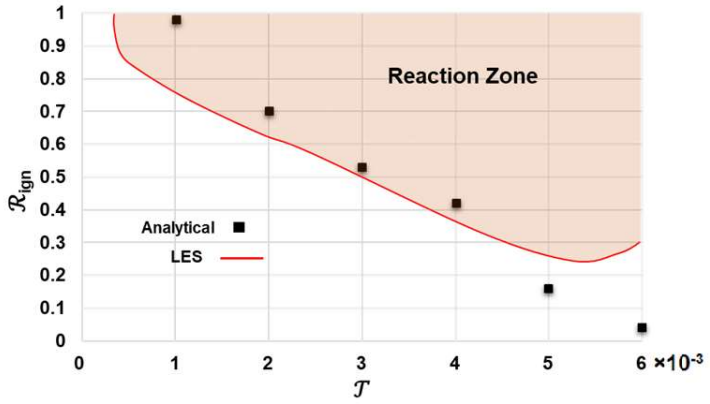

Figure 5-7: Radial coordinate of ignition onset versus elapsed time (stoichiometric)

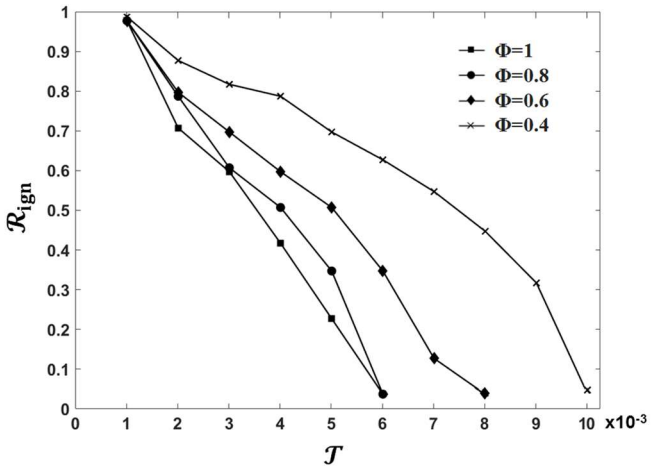

Figure 5-8: Location versus time of ignition onset as a function of the main chamber equivalence ratio

The effect of the main chamber equivalence ratio on the location of ignition frontier is presented in Figure 5-8. For leaner mixtures, the ignition radius has a slower migration rate, the instantaneous chemical induction time is longer and ignition is prolonged.

To assess the combined effect on the ignition process of operational parameters such as jet temperature and main chamber equivalence ratio (Φ), we define an ignition migration rate as the radial propagation rate of the ignition onset location towards the jet centerline. It is taken as the piece-wise averaged slope of the ignition boundary in the $\mathcal{R} - \mathcal{T}$ plane, $\frac{d\mathcal{R}_{ign}}{d\mathcal{T}}$, in which $\mathcal{R}_{ign}$ is the radial coordinate of the ignition onset. The values of $\frac{d\mathcal{R}_{ign}}{d\mathcal{T}}$ are shown in a color level plot in Figure 5-9. The ignition migration rate shown in the plot ranges from no-ignition ($\frac{d\mathcal{R}_{ign}}{d\mathcal{T}} = 0$) to high ignition migration rates. It is observed that at very lean mixtures and low injection temperatures, there is no ignition with the present model. It is also observed that as the mixture approaches the stoichiometric condition, ignition can be achieved with lower hot gas injection temperature. Beyond the substantial role of fuel-air ratio, the injection temperature does not appear to have a strong influence on ignition. Carpio et al. [11] introduced a "crossover" temperature as the threshold above which the chain-branching reactions can overcome the chain-terminating reactions to yield a net production rate. As soon as the temperature of the mixing layer with the right composition exceeds the critical ignition threshold, the ignition is established. Thus, increasing the injection temperature beyond the crossover value does not necessarily result in higher ignition migration rate.

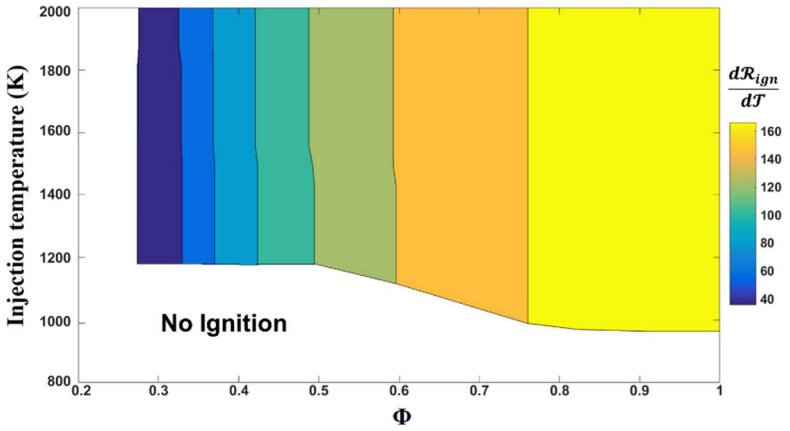

Figure 5-9: Joint effect of injection temperature and main chamber equivalence ratio on the ignition migration rate

5.4.3 Spatial limit of the model in the near field

In the present near-field ignition model, the ignition process is controlled by turbulent diffusion at small scales which drives the reactants to the hot shear layer and forms initiating reactions. To measure the applicable spatial extent of our model and to differentiate transport mechanisms, the regions in the mixing layer that exhibit high intensity of diffusive mixing are identified. A "diffusion index" is developed which is adapted from the flame index proposed by Yamashita et al. [157]. We define the diffusion index (κ) to be the negative square of jet mixture fraction gradient normalized by the maximum gradient over the flame thermal thickness:

$$\kappa = \frac{-(\nabla f)^2}{\left(1/\delta_f\right)^2} \qquad \text{Eq. 5-14}$$

where δ_f is flame thickness and is considered 0.7 mm for the present study [158]. The diffusion index is -1 for purely diffusive mixing and 0 for perfectly mixed regions in which non-diffusive mechanisms dominate, specifically large-scale entrainment.

The instantaneous distribution of the diffusion index is shown in Figure 5-10 overlaid by iso-curves of hydroperoxyl $Y_{HO2}=4\times10^{-4}$ which indicates the reaction initiation zones. It is observed that at the nozzle near-field where the shear forces are large, the diffusion index yields a value of -1. However, the diffusion index diminishes further downstream of the nozzle as the large-scale flow structures control the mixing process. It is seen in Figure 5-10 that the majority of ignition initiation in the trailing sheer layer for $0 < z < 12\ mm\ (4D)$ is induced by diffusive mixing, allowing the present analytical model. However, as the large mixing structure emerges further downstream of the nozzle ($4D < z$), the reaction zones tend to appear at regions with higher diffusion index. Therefore, due to the growing likelihood of autoignition, it is not recommended to utilize the present ignition model beyond the the identified distance limit of $4D$.

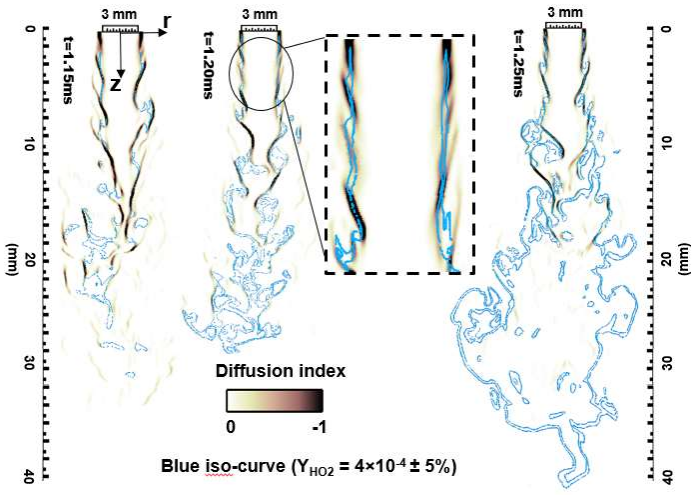

Figure 5-10: Distribution of diffusion index and Y_{HO2} iso-curve obtained in the present LES

5.5 Conclusion

In this work, an analytical solution of heat/mass transport equation for the near-field shear layer of a suddenly-starting jet is sought in order to illuminate the transport mechanism in TJI and facilitate the spatiotemporal identification of ignition. For sufficiently reactive fuels, the near field generates chemically active radicals, which either could immediately form ignition kernels, or could enable ignition formation in the jet downstream where sufficient residence time is available. The evolution of jet mixture fraction and temperature distribution in a slug of jet fluid advancing with the jet initial velocity is predicted in its Lagrangian frame of reference. Assuming two radially different constants for effective turbulent diffusivity in the interior and exterior regions of the jet, the time-varying radial distribution of the jet mixture fraction is obtained. To identify the moment of ignition, the solution for jet mixture fraction is then integrated with a global expression for the instantaneous chemical induction time. For calibration of the analytical solution, a well-resolved LES model of the starting turbulent jet is developed which incorporates the detailed kinetics and the sub-grid scale turbulence-chemistry interactions. The following observations are offered from this near-field modeling effort:

- The most rapid onset of ignition, corresponding to the lowest value of corrected induction time (τ_a), occurs in the rich region of jet mixture fraction space at $f \approx 0.8$. This value may correspond to the region of the jet where $0 < \mathcal{R} < 1$.

- The advance of the radial location of ignition shows the migration of the reaction zone towards the jet centerline, which is confirmed by LES characterization of hydroperoxyl distribution.
- The radial migration rate of ignition location has a strong dependence on the main chamber fuel-air ratio, while it preserves a weak dependence on the injection temperature of the jet above the crossover threshold.
- A useful parameter defined as the diffusion index (κ) is developed to identify the spatial range of applicability of the present model. The overlaid distribution of κ and HO_2 shows that the initiation reaction within four diameters downstream of the nozzle can occur at $\kappa = -1$, which infers the dominance of diffusion-controlled ignition in contrast with chemically controlled ignition under conditions where mixing is very fast.

6. SIMULATION OF IGNITION IN THE HEAD VORTEX OF A STARTING HOT JET

6.1 Abstract

The sudden imposition of a large velocity gradient by the starting jet generates the characteristic head vortex ring that is followed by the high velocity trailing jet. In all mixing regions of the transient jet, parcels of hot gas mix with premixed fuel and air giving rise to the possibility of local ignition. However, the mixing process in the head vortex has a significantly different nature than in the trailing jet. As depicted in Figure 6-1, the near-field shear layer that surrounds the trailing edge exchanges mass diffusively between the hot jet and cold fuel-air mixture. In contrast, the head vortex ring contributes to the mixing by large convective entrainment enhanced by local diffusive processes. When studying the ignition at the head vortex ring, the thermal and hydrodynamic behavior of the vortex must be considered as well as the instabilities and pinch-off that prompts the separation of the vortex ring from the trailing jet.

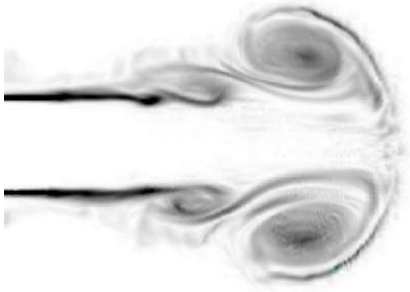

Figure 6-1: Vorticity field in a transient turbulent jet

6.2 Hydrodynamics of the head vortex

This section gathers the relevant literature that addresses various aspects of vortex dynamics.

6.2.1 Size and velocity variation of the vortex ring

The large body of literature that addresses the hydrodynamics of the head vortex ring have varying approaches with respect to modeling the characteristic size and velocity of the vortex. The main reason for the variation stems from different experimental approaches in generation of the

vortex; e.g. syringe versus orifice vortex generators [133, 159], low and high Reynolds numbers, and the "thin vortex core" assumption [133].

Due to the distribution of the jet tip momentum driving formation and growth of the vortex ring, the translational velocity of the ring is typically a fraction of the jet tip velocity that would exist later in time at the same point. According to Turner [121], the vortex moves almost at the half of speed of the jet when the jet tip reaches to the same spot at a later time. Quasi-steady analysis of turbulent transient jets by Abraham shows the inverse relation between the jet vortex velocity with position as $U_v \sim x_{tip}^{-1}$ and consequently, $U_v \sim t^{-1/2}$ [87, 119], where U_v is the vortex velocity. However, Maxworthy [133] claimed that the vortex ring translates with velocity $U_v \sim exp(-x)$ and thus $U_v \sim t^{-1}$. His statement was later corrected by a more comprehensive work on an isolated vortex by Dabiri [159] that proposed $U_v \sim t^{-0.34}$ which agrees better with Abraham's findings.

In terms of the vortex size change, Maxworthy conducted a simple dimensional analysis and deduced the relation between characteristic vortex dimension, a, and time as $a \sim t^{1/3}$ assuming the impulse of the head vortex ring is conserved (no body force or frictional dissipations) [133]. The impulse of the ring (I) is given as a function of the circulation Γ, by

$$I = \alpha a^2 \Gamma.$$

In the constant-impulse assumption of the head vortex ring it is required that as the vortex radius (r) is increasing in time, Γ must decrease.

Maxworthy developed a model to describe the volume growth of the leading vortex when only caused by entrainment from the ambient environment occurring through diffusion. As seen in the sketch of a vortex ring in its own frame of reference in Figure 6-2 obtained from Ref. [133], due to the relative motion between the vortex ring and the still ambient, mass is entrained into the vortex near the trailing jet due to the adverse pressure gradient.

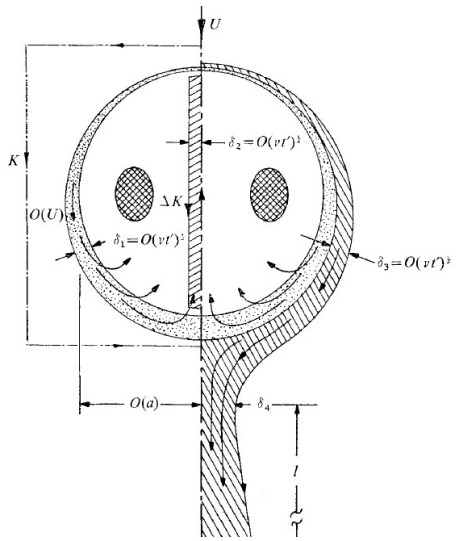

Figure 6-2: Entrainment model of a homogeneous vortex ring (Courtesy of Maxworthy, 1972)

The vortex growth model proposed by Maxworthy based on the entrainment and diffusion model relates vortex torus (ring) volume to time as [133]:

$$V(t) = A(\nu I)^{1/2} t + D \qquad \text{Eq. 6-1}$$

where V is the vortex volume, I is the jet impulse (constant) and ν is the kinematic viscosity. Also, A and D are evaluated by the initial conditions, requiring the volume of the vortex at the beginning of diffusion phase. It must be noted that Eq. 6-1 does not address the initial growing phase of the vortex due to the advection of large structures.

6.2.2 Vortex pinch-off

As the jet evolves spatially, regions with distributed vorticity form on the shear layer. The distribution of these vortices often is not uniform due to the perturbations caused by Kelvin-Helmholtz instabilities. These instabilities create a region with minimal vorticity that chokes off the delivery of the momentum flow to the vortex. As the result, the vortex ring detaches from the trailing jet in a "pinch-off" process (Figure 6-3). Of course, this process requires special attention since the mass entrainment in an isolated vortex is profoundly different than a vortex that is attached to the jet.

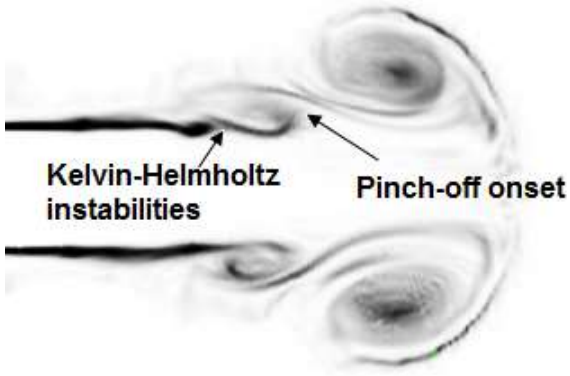

Figure 6-3: The vorticity magnitude is shown in a black and white color

The significance of the pinch-off for ignition lies within the fact that once the vortex departs the trailing jet, mixing with the cold environment continues while no more hot gas is supplied, which typically leads to dissolving the vortex in its surrounding. Therefore, the ignition probability might decline drastically after the pinch-off.

Several studies verify that after the vortex gained certain amount of circulation, it detaches from the trailing jet [103, 160]. Figure 6-4 shows a typical history of vorticity accumulation in a transient compressible jet. The solid line represents the total vorticity and dashed line represents the embedded vorticity in the main vortex ring. After certain elapsed time, the vortex maintains its circulation level and does not grow any further. Usually, this moment is when the pinch-off occurs. The recent study by Fernandez [103] suggests that for compressible turbulent jets with infinite discharge mass (jet that does not cease after starting), pinch-off occurs at the range of $1 < (\Gamma/U_j D_j)_{pinch-off} < 2$ where Γ is the circulation, and U_j and D_j are jet velocity and jet diameter at the nozzle, respectively.

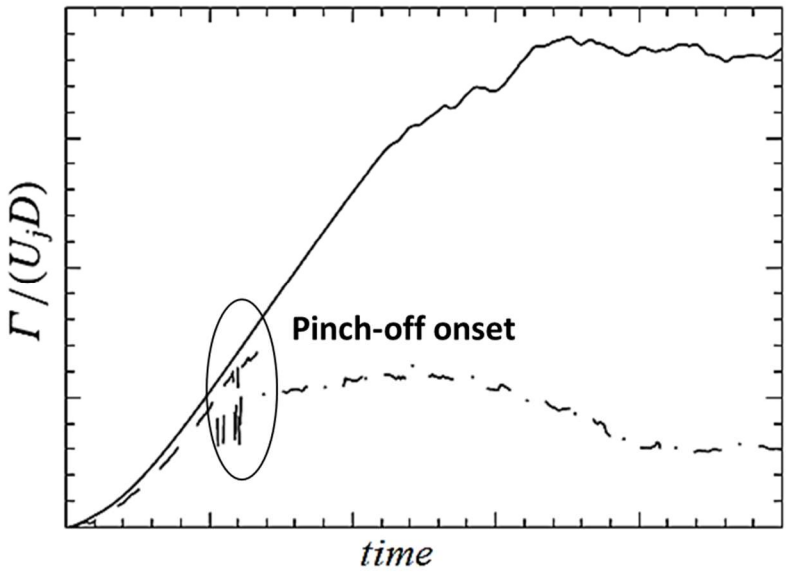

Figure 6-4: Total circulation contained in the transient jet (——) and the circulation contained in the vortex ring (— · —)

Through numerous experiments, Fernandez established a universal relationship between critical circulation and the dimensionless time, i.e. $t^*=t/(D_j/U_j)$, when pinch-off takes place as [103]:

$$(\Gamma/U_jD_j)_{pinch-off} = 5.0071 - 0.3467t^* \qquad \text{Eq. 6-2}$$

For the purpose of prediction ignition in the vortex ring, tracking the thermo-chemistry composition of the vortex is only worthwhile before pinch-off. It is expected that after the pinch-off moment, the vortex no longer can support ignition due to cooling effects and excessive mixing with the environment.

LES of a transient hot jet is performed until shortly after the pinch-off phase. As depicted by the history of circulation (Figure 6-5), the pinch-off onset occurs as the circulation at the head vortex reaches saturation and no further accumulation of the vorticity in the head vortex happens. The pinch-off moment in real time as predicted by LES is then compared with the predictions of the empirical model described in Eq. 6-2 and they agree within 80% accuracy.

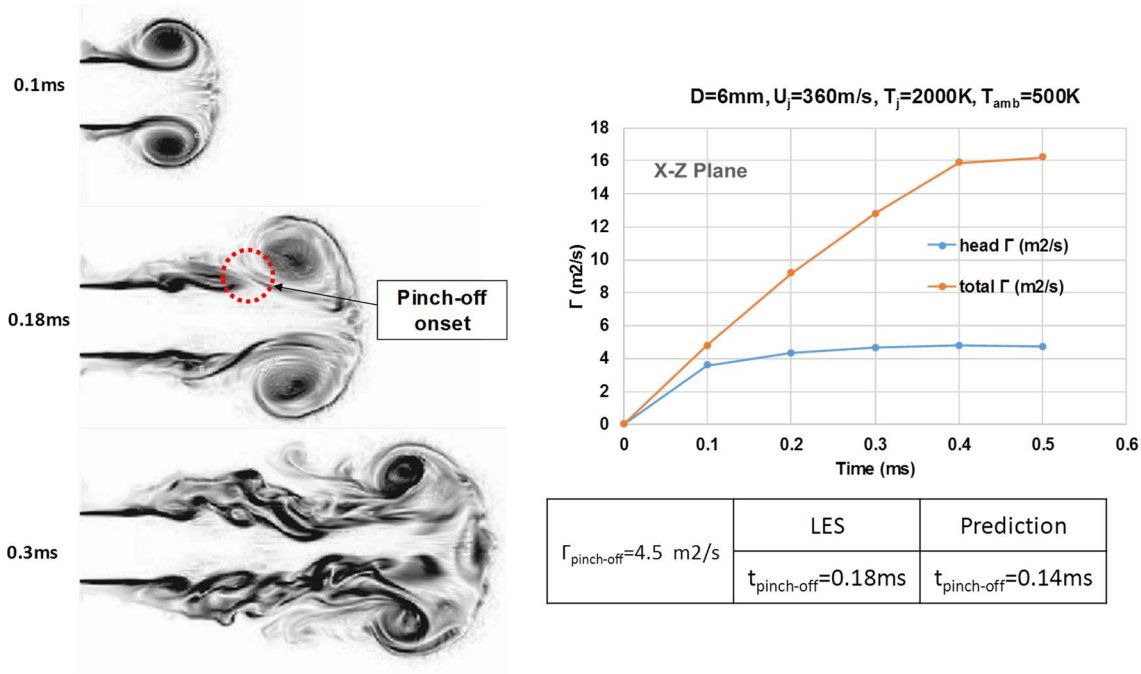

Figure 6-5: Large eddy simulation of vorticity and pinch-off onset for a reacting hot jet (U_j=360m/s, D_j=6mm)

6.2.3 Vortex composition

Data extracted from the LES model of a non-reacting starting jet, when the jet is issued at U_j = 360m/s from an nozzle with D_j = 6mm, indicate that vortex ring growth occurs through a rapid convective entrainment phase (0-0.1ms in Figure 6-6), followed by a slower diffusive mechanism that further entrains ambient fluid into the isolated vortex ring. A few studies have attempted to estimate the composition of the vortex ring by comparing the contributions of the ambient gas and the jet in delivering mass to the vortex ring. Turner [121] first addressed the evolution of a buoyant plume in uniform surrounding and claimed that half of the fluid mixed into the cap comes from the ambient fluid and the rest is supplied from the trailing jet. The study on the air vortex formation done by Syed and Sung [161] estimated the entrainment fraction from surrounding environment to be approximately 35-40% in their experiment. The isolated vortex ring investigated experimentally in the work of Dabiri et al. [159] shows that the entrained fluid from the ambient fluid typically constitutes 30-40% of the total vortex volume. In a direct numerical simulation of the vortex ring, Sau and Mahesh [162] computed entrainment fraction to be between 30-40%,

consistent with previous findings. Thus, under varying conditions of a vortex ring formation, studied by different approaches, the concentration of ambient gases in the vortex ring after the end of convective entrainment is found to be about 30-40%. Thus, the 60-70% of the vortex constitutes the trailing jet species.

The jet mixture fraction concentration in the vortex is obtained from the LES of the reacting jet of Figure 6-5 and is presented in Figure 6-6. The mixture fraction species constitutes a conserved scalar which has a concentration of unity at the nozzle exit and is diffused into an ambient which initially has zero concentration. The location where mixture fraction is sampled is shown in the vorticity plots of the jet by the yellow dashed line. As observed during time 0.3-0.4ms, the "eye" of the vortex ring shows the average mixture fraction of 0.6-0.7 which resembles the numbers suggested in the literature. However, it must be noted that the geometry of confinement into which the jet is issued affects the mass entrainment waves and thus the jet concentration. It is also evident that in the long-term (t=0.6ms), the vortex is highly diluted with ambient species which explains the sudden drop and asymmetry of the mass distribution across the vortex ring.

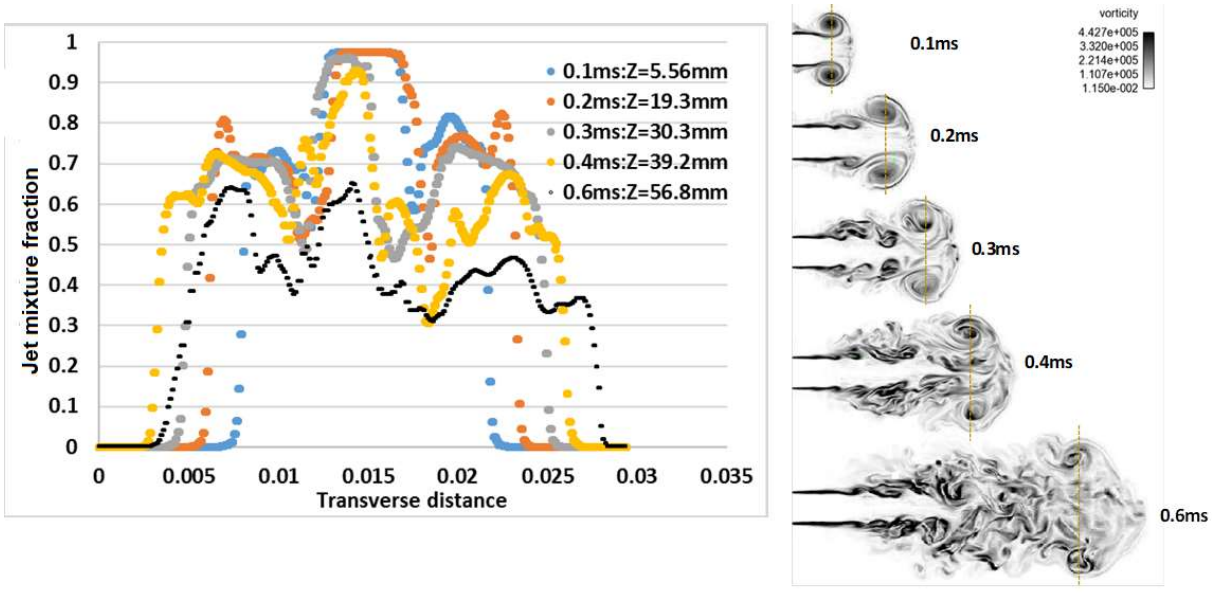

Figure 6-6: The vortex head jet mixture fraction measured at the central vortex cross section.

6.3 Ignition analysis at the head vortex

The strong large-scale mixing mechanisms in the leading vortex of a starting jet supports the assumption of uniform concentration and temperature within the vortex. This section presents a transient zero-dimensional simulation of the spontaneous ignition event in a batch-reactor that represents the chemistry of the head vortex. The constant-pressure batch reactor will reflect the contribution of pre-chamber and main chamber species in the formation of head vortex. Here we are interested in determining the ignition time within a homogenous batch reactor under a specified set of initial pressure, temperature and species concentration, assuming no heat exchange with the environment. Thus, we assume a prescribed mixture fraction at the vortex, which implies known initial thermochemical composition. Conservation of mass and energy helps us to determine the initial thermochemical composition of the vortex as,

$$Y_{i,V} = (1-f)Y_{i,m} + fY_{i,p} \qquad \text{Eq. 6-3}$$

$$(c_v T)_V = (1-f)(c_v T)_m + f(c_v T)_p \qquad \text{Eq. 6-4}$$

where Y_i is the mass fraction of *i*th species, and subscripts V, m and p refers to the initial states of vortex, main chamber and products of the pre-chamber.

Figure 6-7 depicts schematic of a batch reactor at constant pressure, undergoing the ignition process. The reaction within the volume occurs uniformly everywhere, thus there are no temperature of composition gradients within the mixture. The following system of first-order differential equations can describe the temporal evolution of species and temperature based on the initial values of the problem [32].

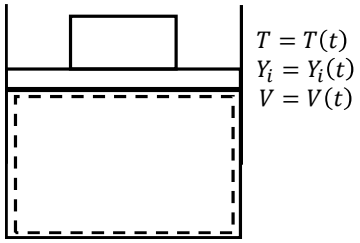

Figure 6-7: Constant-pressure fixed-mass reactor

$$\frac{dT}{dt} = \frac{\left(\dot{Q}/V\right) - \sum_i \left(\bar{h}_i \dot{\omega}_i\right)}{\sum_i \left([X_i]\bar{c}_{p,i}\right)}, \qquad i = 1, 2, \ldots., N \qquad \text{Eq. 6-5}$$

$$\bar{h}_i = \bar{h}^0_{f,i} + \int_{T_{ref}}^{T} \bar{c}_{p,i}\, dT \qquad \text{Eq. 6-6}$$

$$\frac{d[X_i]}{dt} = \dot{\omega}_i - [X_i]\left[\frac{\sum \dot{\omega}_i}{\sum_j [X_j]} + \frac{1}{T}\frac{dT}{dt}\right], \qquad i\ \&\ j = 1, 2, \ldots., N \qquad \text{Eq. 6-7}$$

with the initial conditions

$$T(t = 0) = T_0$$

and

$$[X_j](t = 0) = [X_j]_0$$

In the above equations, $\dot{Q}$ is the heat release rate, V is the reactor volume, and $\bar{h}_i$, $[X_i]$ and $\dot{\omega}_i$ are the total enthalpy, molar concentration, and formation/consumption rate of the ith specie, respectively. To predict the rate of reaction towards ignition, we use the GRI 3.0 mechanism [27]. A zero-dimensional chemical kinetic calculation is performed assuming atmospheric pressure and standard air composition, using CHEMKIN Pro [71] . CHEMKIN Pro is a software tool for solving complex chemical kinetics problems by computing multiple elementary reactions to model the variations of thermochemical properties within the reactor.

Table 6-1 presents the compositions of the pre-chamber and main chamber gases used in our kinetic simulation of the vortex ignition. The pre-chamber compositions are developed by equilibrium calculation of 50%CH_4-50%H_2 (volumetric) combusted with air at various equivalence ratios. The main chamber is also examined with stoichiometric methane-air and stoichiometric 50%CH_4-50%H_2 combustion with air. The initial thermochemical state of the vortex can be calculated by conservation Eq. 6-3 and Eq. 6-4 assuming that main chamber and pre-chamber gases constitute 40% and 60% of the volume of the vortex, respectively. This assumption is consistent with the experimental evidences from the literature which suggest the similar ratios [159, 161, 162].

The equivalence ratio of pre-chamber has an important effect on the ignition process at the head vortex, due to temperature of and presence of active compounds in the resulting jet. To obtain the effect of pre-chamber equivalence ratio on the ignition characteristics within the vortex, five equivalence ratios (0.4, 0.6, 0.8, 1.0, 1.1) are selected for the pre-chaamber with the initial standard pressure. As shown in Table 6-1, the equilibrium temperature of the jet reaches its maximum when stoichiometric mixture is combusted. Additionally, the concentration of active radical such as OH and H is maximized at slightly rich pre-chamber mixtures.

Table 6-1: Initial temperature, equivalence ratio and mass fraction

Thermodynamic properties	**Pre-chamber 50%-50% CH_4-H_2**					**Main chamber pure CH_4**	**Main chamber 50%-50% CH_4-H_2**
Equivalence ratio	0.4	0.6	0.8	1	1.1	1	1
Temperature(K)	1602	2069	2471	2812	2763	300	300
X_{N2}	0.74271	0.72333	0.70501	0.69008	0.6732	0.714829	0.676
X_{O2}	0.11867	0.07478	0.03333	0.00113	0.00001	0.190114	0.18
X_{H2}	0	0	0.00007	0.00176	0.01335	0	0.072
X_{CH4}	0	0	0	0	0	0.095057	0.072
X_{OH}	0.00002	0.00035	0.0014	0.0016	0.00049		
X_{O}	0	0	0.00003	0.00002	0		
X_{H2O}	0.09572	0.14005	0.18184	0.21995	0.22467		
X_{H}	0	0	0	0.00004	0.0001		
X_{CO2}	0.03222	0.04705	0.06105	0.07052	0.05661		
X_{CO}	0	0.00001	0.00013	0.00394	0.02312		
X_{NO}	0.00143	0.00527	0.00824	0.00257	0.00026		

In Figure 6-8 and Figure 6-9, the temperature and OH concentration in the batch reactor is plotted against time for when the main chamber and the pre-chamber with prescribed properties represent 40% and 60% of the vortex volume, respectively. The leading vortex can host ignition if the initial temperature and specie concentration in the vortex allow the initiating reactions. The moment of ignition is taken to be when the OH content of the batch reactor increases 15% above the initial value. It is seen from Figure 6-8 and Figure 6-9 that the minimum ignition delay at the vortex occurs when the pre-chamber is initially filled with stoichiometric mixture. This is due to the substantial dependence of the vortex reactions on the jet temperature. Since pure methane has lower reactivity compared to 50% methane-50% hydrogen mixture, it is observed in Figure 6-8

that the ignition does not take place when the jet is issued from a lean pre-chamber as Φ<1. However, 50% methane-50% hydrogen mixture is more prone to ignition even when the pre-chamber mixture is as lean as Φ=0.6.

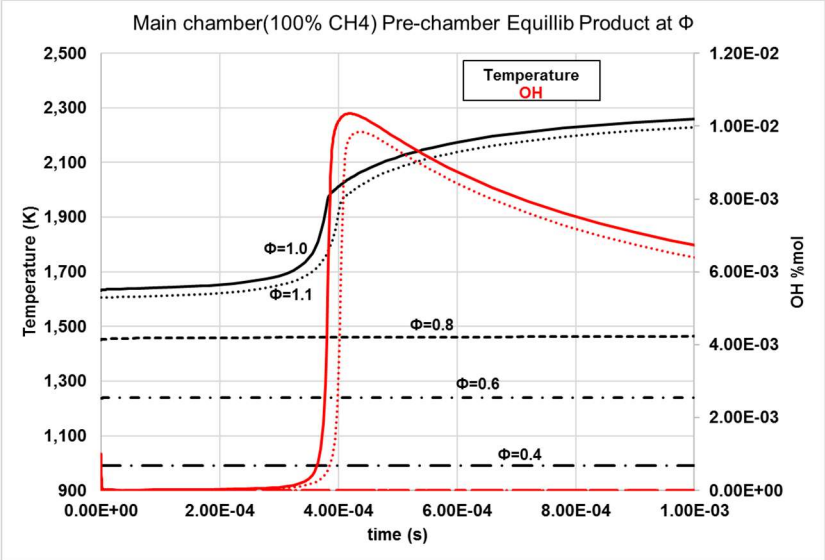

Figure 6-8: Temperature and OH mole fraction history of homogeneous batch reactor used to determine ignition delay time for stoichiometric ignition of 100% methane with air

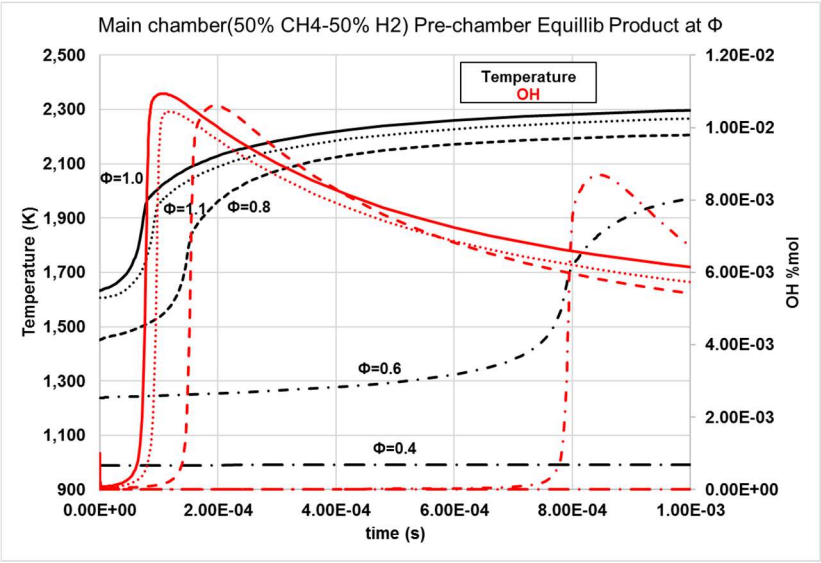

Figure 6-9: Temperature and OH mole fraction history of homogeneous batch reactor used to determine ignition delay time for stoichiometric ignition of 50% methane-50% hydrogen with air

Table 6-2 summarizes the vortex ignition delay based on the OH signal obtained from the reactor.

Table 6-2: Ignition delay summary for the tested fuels

Ignition delay (μs) / Pre-chamber Equivalence ratio, Φ	**Main chamber, stoichiometric air + CH_4**	**Main chamber, stoichiometric air + 50%-50% CH_4-H_2**
0.4	No ignition	No ignition
0.6	No ignition	80
0.8	No ignition	15
1	36	6
1.1	39	8

7. RECOMMENDATIONS FOR FUTURE WORKS

The potential of the hot jet ignition method in enabling the lean-burn combustion devices merits further studies to use this technology on low-calorific fuels and mixtures. Our understanding about the ignition evolution shows a meaningful difference between the ignition of low and high-reactivity fuels. Since the greater focus of this study was on the near-field ignition, the insights developed can better contribute to the ignition process of fuels with high reactivity that tend to begin ignition in the near field. With respect to the fuels with slower chemistry, it is necessary to consider the mixing and reaction process further away, both within the large-scale instabilities of the shear layer, and the leading vortex ring. However, this is assuming that the ignition delay time is still shorter than the time needed for a fully-developed steady jet formation.

The following suggestions may direct future research aimed at fuels with lower reactivity levels.

1. Ignition in the region of shear layer instabilities

The formation of instabilities in the shear layer can be accounted for by the near-field model developed in Chapter 5 with this caveat that the instabilities can temporally cause fluctuations in the diffusivity constant. Such fluctuations could be modeled to extend the near-field model to understand diffusion-like mixing in the jet region of shear-layer instabilities, and potentially to predict ignition in this region. For instance, the first-order gradient term in the Eq. 5-7 in the cold zone can be perturbed by a factor of ε as follows:

$$\frac{d^2\bar{\theta}}{d\xi^2} + \frac{1+2\xi^2}{\xi}\frac{d\bar{\theta}}{d\xi} + \varepsilon\frac{d\bar{\theta}}{d\xi} = 0$$

This equation has an explicit solution in the form of

$$\bar{\theta}(\xi) = A\int_{\xi}^{\infty}\frac{e^{-\varepsilon\lambda-\ ^2}}{\lambda}d\lambda + B$$

2. Ignition in the vortex ring

The mixing mechanism at the leading vortex ring has two major stages. In the first stage upon the formation of the vortex, the ambient gas is engulfed by the vortex in a rapid process. The amount of the engulfed gas appears to be a function of jet impulse and diameter [133]. The second stage of vortex growth and development is a mass entrainment process that appears to admit gases from the surrounding as well as from the jet source to the vortex. In Chapter 6 we proposed a constant

jet mixture fraction within the vortex ring, which is assumed to remain perfectly mixed, with the constant mixture fraction maintained by requiring any entrainment to match this constant. These assumptions can be modified for a more detailed analysis of the vortex mixing stages. The time-evolution and differential entrainment of gases, the inhomogeneity of the species in the vortex ring, and the lack of perfect mixedness, could be considered in future work.

3. Characterization of jet mixing for specific confined and impinging jets

Due to the small confinement of the combustion chamber, the hot gas jet is very likely to imping on chamber walls and have a curved trajectory during the ignition process. This effect has been empirically analyzed by some researchers [25, 42] but rarely addressed by models or fundamental studies. The curvature of the jet trajectory and its effect on the mixing process may have important effects in ignition.

4. Consideration of the wave-rotor ignition requirements

The initiation of combustion in each channel of a wave-rotor requires the hot jet to be issued from a hot gas nozzle at one end as the channel passes across nozzle. The nozzle may be supplied with hot gas from other combusted channels or by a separate torch igniter. The traversing motion of the nozzle relative to the channel and its particular confined shape results in evolution of a particular pattern of large-scale flow structures and vortices that precede ignition [163-165]. These include jet impingement and curvature, and the formation of counter-rotating vortices as the nozzle location shifts relative to the confined space. Characterization of the traversing jet ignition by analytical and numerical methods is important to predict ignition in wave-rotor combustors.

REFERENCES

1. Feyz, M.E., et al., *Three-Dimensional Simulation of Turbulent Hot-Jet Ignition for Air-CH4-H2 Deflagration in a Confined Volume.* Flow, Turbulence and Combustion, 2018. **101**(1): p. 123-137.
2. Feyz, M.E., et al., *Large eddy simulation of hot jet ignition in moderate and high-reactivity mixtures.* Computers & Fluids, 2019. **183**: p. 28-37.
3. Feyz, M.E., et al., *Scalar predictors of premixed gas ignition by a suddenly-starting hot jet.* International Journal of Hydrogen Energy, 2019. **44**(42): p. 23793-23806.
4. Feyz, M.E., et al., *Modeling and Analytical Solution of Near-Field Entrainment in Suddenly Started Turbulent Jets.* AIAA Journal, 2019. **57**(5): p. 1877-1884.
5. Akbari, P., R. Nalim, and N. Mueller, *A Review of Wave Rotor Technology and Its Applications.* Journal of Engineering for Gas Turbines and Power, 2006. **128**(4): p. 717-735.
6. Oppenheim, A.K., *Combustion in Piston Engines: Technology, Evolution, Diagnosis and Control*. 2004: Berlin: Springer.
7. Gussak, L.A., V.P. Karpov, and Y.V. Tikhonov, *The Application of Lag-Process in Prechamber Engines.* SAE Transactions, 1979. **88**: p. 2355-2380.
8. Wolanski, P., et al., *Study of Combustion Dynamics in the Research Engine*. 1997, SAE International.
9. Chinnathambi, P., *Experimental investigation on traversing hot jet ignition of lean hydrocarbon-air mixtures in a constant volume combustor*. 2014, Purdue University: Indianapolis, IN.
10. Fink, Z.J. and M. Vanpee, *Overall Kinetics of Hot Gas Ignition.* Combustion Science and Technology, 1975. **11**(5-6): p. 229-238.
11. Carpio, J., et al., *Critical radius for hot-jet ignition of hydrogen–air mixtures.* International Journal of Hydrogen Energy, 2013. **38**(7): p. 3105-3109.
12. Gentz, G., et al., *A study of the influence of orifice diameter on a turbulent jet ignition system through combustion visualization and performance characterization in a rapid compression machine.* Applied Thermal Engineering, 2015. **81**: p. 399-411.
13. Iglesias, I., et al., *Numerical analyses of deflagration initiation by a hot jet.* Combustion Theory and Modelling, 2012. **16**(6): p. 994-1010.
14. Ghorbani, A., et al., *Numerical Investigation of Ignition in a Transient Turbulent Jet by Means of a PDF Method.* Combustion Science and Technology, 2014. **186**(10-11): p. 1582-1596.
15. Ghorbani, A., et al., *A numerical approach to investigate the maximum permissible nozzle diameter in explosion by hot turbulent jets.* Journal of Loss Prevention in the Process Industries, 2015. **36**: p. 539-543.
16. Sadanandan, R., Markus, D., Schießl, R., Maas, U., Olofsson, J., Seyfried, H., Richter, M., Aldén, M., *Detailed investigation of ignition by hot gas jets.* Proceedings of the Combustion Institute, 2007. **31**(1): p. 719-726.
17. Brouillette, M., *THE RICHTMYER-MESHKOV INSTABILITY.* 2002. **34**(1): p. 445-468.
18. Paik, K.-Y., *Experimental investigation of hot-jet ignition of methane-hydrogen mixtures in a constant-volume combustor*. 2016, Purdue University.

19. Zhang, Y., et al., *Experimental and modeling study on ignition delays of lean mixtures of methane, hydrogen, oxygen, and argon at elevated pressures.* Combustion and Flame, 2012. **159**(3): p. 918-931.
20. Goodwin, D.G., *An open-source, extensible software suite for CVD process simulation.* Chemical Vapor Deposition XVI and EUROCVD, 2003. **40**(14): p. 2003-2008.
21. Khan, M.N., *Three-dimensional transient numerical study of hot-jet ignition of methane-hydrogen blends in a constant-volume combustor*. 2015, Purdue University: Indianapolis, IN.
22. Karimi, A., et al., *Hot Jet Re-ignition of Hydrocarbons and Hydrogen in Air: Effect of Jet Chemical Activity*, in *49th AIAA/ASME/SAE/ASEE Joint Propulsion Conference*.
23. Nalim, M.R., P.H. Snyder, and M. Kowalkowski, *Experimental Test, Model Validation, and Viability Assessment of a Wave-Rotor Constant-Volume Combustor.* Journal of Propulsion and Power, 2016. **33**(1): p. 163-175.
24. Richards, K.J., Senecal, P. K., and Pomraning, E., *CONVERGE 2.4, Convergent Science, Madison, WI* 2019.
25. Song, L. and J. Abraham, *Entrainment Characteristics of Transient Turbulent Round, Radial and Wall-Impinging Jets: Theoretical Deductions.* Journal of Fluids Engineering, 2003. **125**(4): p. 605-612.
26. Kazakov A, F.M., *Reduced reaction sets based on GRIMech 1.2* Available at http://combustion.berkeley.edu/drm/ 5/28/2019.
27. Gregory P. Smith, D.M.G., Michael Frenklach, Nigel W. Moriarty, Boris Eiteneer, Mikhail Goldenberg, C. Thomas Bowman, Ronald K. Hanson, Soonho Song, William C. Gardiner, Jr., Vitali V. Lissianski, and Zhiwei Qin, *GRI 3.0.*
28. Sung, C.J., C.K. Law, and J.Y. Chen, *Further Validation of an Augmented Reduced Mechanism for Methane Oxidation: Comparison of Global Parameters and Detailed Structure.* Combustion Science and Technology, 2000. **156**(1): p. 201-220.
29. Mansourian, M. and R. Kamali, *Computational fluid dynamics analysis of a synthesis gas turbulent combustion in a round jet burner.* Acta Astronautica, 2017. **134**: p. 133-140.
30. Steinhilber, G., V. Bykov, and U. Maas, *REDIM reduced modeling of flame-wall-interactions: Quenching of a premixed methane/air flame at a cold inert wall.* Proceedings of the Combustion Institute, 2017. **36**(1): p. 655-661.
31. Gholamisheeri, M., I.S. Wichman, and E. Toulson, *A study of the turbulent jet flow field in a methane fueled turbulent jet ignition (TJI) system.* Combustion and Flame, 2017. **183**: p. 194-206.
32. Turns, S.R., *An introduction to combustion* Vol. 287. 1996: New York: McGraw-Hill.
33. Issa, R.I., *Solution of the implicitly discretised fluid flow equations by operator-splitting.* Journal of Computational Physics, 1986. **62**(1): p. 40-65.
34. Sangras, R., O.C. Kwon, and G.M. Faeth, *Self-Preserving Properties of Unsteady Round Nonbuoyant Turbulent Starting Jets and Puffs in Still Fluids.* Journal of Heat Transfer, 2002. **124**(3): p. 460-469.
35. Mayinger, F., Jordan, M., Eder, A., Zaslonko, I.S., Karpov, V.P. and Frolov, S.M., , *Flame-jet ignition of fuel-air mixtures. Experimental findings and modeling*, in *17th International Colloquium on the Dynamics of Explosions and Reactive Systems (ICDERS)*. 1999: Heidelberg, Germany. p. 25-30.
36. Glassman, I., Yetter, R.A. and Glumac, N.G., , *Combustion*. 2014: Academic press.

37. Brower, M., et al., *Ignition Delay Time and Laminar Flame Speed Calculations for Natural Gas/Hydrogen Blends at Elevated Pressures.* Journal of Engineering for Gas Turbines and Power, 2013. **135**(2).
38. Akbari, P. and R. Nalim, *Review of Recent Developments in Wave Rotor Combustion Technology.* Journal of Propulsion and Power, 2009. **25**(4): p. 833-844.
39. Gussak, L.A., V.P. Karpov, and Y.V. Tikhonov, *The Application of Lag-Process in Prechamber Engines*. 1979, SAE International.
40. Yamaguchi, S., N. Ohiwa, and T. Hasegawa, *Ignition and burning process in a divided chamber bomb.* Combustion and Flame, 1985. **59**(2): p. 177-187.
41. Rajagopal, M.K., M.R. Nalim, and M.N. Khan, *Simulation of Hot-Jet Ignition in a Heated Constant-Volume Combustor Using Adadptive Mesh Refinement and Multi-Zone Reaction*, in *50th AIAA/ASME/SAE/ASEE Joint Propulsion Conference*. 2014, American Institute of Aeronautics and Astronautics.
42. Biswas, S., *Physics of Turbulent Jet Ignition: Mechanisms and Dynamics of Ultra-Lean Combustion*. 2018: Springer.
43. Gentz, G., M. Gholamisheeri, and E. Toulson, *A study of a turbulent jet ignition system fueled with iso-octane: Pressure trace analysis and combustion visualization.* Applied Energy, 2017. **189**: p. 385-394.
44. Attard, W.P., et al., *A Turbulent Jet Ignition Pre-Chamber Combustion System for Large Fuel Economy Improvements in a Modern Vehicle Powertrain*. 2010, SAE International.
45. Toulson, E., H.J. Schock, and W.P. Attard, *A Review of Pre-Chamber Initiated Jet Ignition Combustion Systems*. 2010, SAE International.
46. Shah, A., P. Tunestal, and B. Johansson, *Investigation of Performance and Emission Characteristics of a Heavy Duty Natural Gas Engine Operated with Pre-Chamber Spark Plug and Dilution with Excess Air and EGR*. 2012, SAE International.
47. Allison, P.M., et al., *Pre-chamber ignition mechanism: Experiments and simulations on turbulent jet flame structure.* Fuel, 2018. **230**: p. 274-281.
48. Ju, Y. and W. Sun, *Plasma assisted combustion: Dynamics and chemistry.* Progress in Energy and Combustion Science, 2015. **48**: p. 21-83.
49. Kopecek, H., et al., *Laser Ignition of Methane-Air Mixtures at High Pressures and Diagnostics*. Vol. 127. 2005. 213-219.
50. Kim, G., et al., *Experimental investigation on combustion and emission characteristics of a premixed flame in a gas-turbine combustor with a vortex generator.* Applied Thermal Engineering, 2015. **77**: p. 57-64.
51. Qin, F., et al., *Detailed numerical simulation of transient mixing and combustion of premixed methane/air mixtures in a pre-chamber/main-chamber system relevant to internal combustion engines.* Combustion and Flame, 2018. **188**: p. 357-366.
52. Validi, A. and F. Jaberi, *Numerical Study of Turbulent Jet Ignition in a Lean Premixed Configuration.* Flow, Turbulence and Combustion, 2018. **100**(1): p. 197-224.
53. Inanc, E., et al., *High-resolution LES of a starting jet.* Computers & Fluids, 2016. **140**: p. 435-449.
54. Ghorbani, A., et al., *Ignition by transient hot turbulent jets: An investigation of ignition mechanisms by means of a PDF/REDIM method.* Proceedings of the Combustion Institute, 2015. **35**(2): p. 2191-2198.
55. Wang, N., et al., *A numerical study on effects of pre-chamber syngas reactivity on hot jet ignition.* Fuel, 2018. **234**: p. 1-8.

56. Arndt, C.M., et al., *The role of temperature, mixture fraction, and scalar dissipation rate on transient methane injection and auto-ignition in a jet in hot coflow burner.* Combustion and Flame, 2016. **167**: p. 60-71.
57. Esclapez, L., E. Riber, and B. Cuenot, *Ignition probability of a partially premixed burner using LES.* Proceedings of the Combustion Institute, 2015. **35**(3): p. 3133-3141.
58. Soulopoulos, N., Y. Hardalupas, and A.M.K.P. Taylor, *Scalar dissipation rate measurements in a starting jet.* Experiments in Fluids, 2014. **55**(3): p. 1685.
59. Jouzdani, S., et al., *Methane and Methyl Propanoate High-Temperature Kinetics.* Energy & Fuels, 2018. **32**(11): p. 11864-11875.
60. Tarraf Kojok, A., *Hot Jet Ignition Delay Characterization of Methane and Hydrogen at Elevated Temperatures*. 2017, Purdue University: United States, North America.
61. Chowdhury, M., *Traversing hot jet ignition delay of hydrocarbon blends in a constant volume combustor*. 2018, Indiana University-Purdue University, Indianapolis: http://ulib.iupui.edu/cgi-bin/proxy.pl?url=http://search.proquest.com/docview/2113503694?accountid=7398.
62. Senecal, P.K., et al., *Modeling Fuel Spray Vapor Distribution With Large Eddy Simulation of Multiple Realizations*. 2014. p. V002T06A002.
63. Pomraning, E., *Development of large eddy simulation turbulence models.* 2000, University of Wisconsin--Madison.
64. Pomraning, E. and C.J. Rutland, *Dynamic One-Equation Nonviscosity Large-Eddy Simulation Model.* AIAA Journal, 2002. **40**(4): p. 689-701.
65. Senecal, P.K., et al., *An Investigation of Grid Convergence for Spray Simulations using an LES Turbulence Model*. 2013, SAE International.
66. Senecal, P.K., Richards, K. J., Pomraning, E., Yang, T., Dai, M. Z., McDavid, R. M., Patterson, M. A., Hou, S., Shethaji, T., *A New Parallel Cut-Cell Cartesian CFD Code for Rapid Grid Generation Applied to In-Cylinder Diesel Engine Simulations*. 2007, SAE International.
67. Hasti, V.R., et al., *Large Eddy Simulation of Pilot Stabilized Turbulent Premixed CH4+Air Jet Flames*, in *2018 AIAA Aerospace Sciences Meeting*. 2018, American Institute of Aeronautics and Astronautics.
68. Hasti, V.R., et al., *A Numerical Study of Flame Characteristics during Lean Blow-Out in a Gas Turbine Combustor*, in *2018 Joint Propulsion Conference*. 2018, American Institute of Aeronautics and Astronautics.
69. Hasti, V.R., et al., *Lean blow-out (LBO) computations in a gas turbine combustor*, in *2018 Joint Propulsion Conference*. 2018, American Institute of Aeronautics and Astronautics.
70. Zettervall, N., K. Nordin-Bates, and C. Fureby, *Understanding Scramjet Combustion using LES of the HyShot II Combustor*, in *20th AIAA International Space Planes and Hypersonic Systems and Technologies Conference*. 2015, American Institute of Aeronautics and Astronautics.
71. Design, R., *CHEMKIN-PRO 15131*. 2013: San Diego.
72. Sjöholm, J., et al., *Simultaneous visualization of OH, CH, CH2O and toluene PLIF in a methane jet flame with varying degrees of turbulence.* Proceedings of the Combustion Institute, 2013. **34**(1): p. 1475-1482.

73. Reddy, H. and J. Abraham, *Influence of turbulence–kernel interactions on flame development in lean methane/air mixtures under natural gas-fueled engine conditions.* Fuel, 2013. **103**: p. 1090-1105.
74. Kuo, K.K.-y., and Ragini Acharya, *Fundamentals of turbulent and multiphase combustion*. 2012: John Wiley & Sons.
75. Chaudhuri, S., et al., *Flame thickness and conditional scalar dissipation rate in a premixed temporal turbulent reacting jet.* Combustion and Flame, 2017. **184**: p. 273-285.
76. Bray, K., P. Domingo, and L. Vervisch, *Role of the progress variable in models for partially premixed turbulent combustion.* Combustion and Flame, 2005. **141**(4): p. 431-437.
77. Boretti, A.A. and H.C. Watson, *The lean burn direct injection jet ignition gas engine.* International Journal of Hydrogen Energy, 2009. **34**(18): p. 7835-7841.
78. Karimi, A., M. Rajagopal, and R. Nalim, *Traversing Hot-Jet Ignition in a Constant-Volume Combustor.* Journal of Engineering for Gas Turbines and Power, 2013. **136**(4): p. 041506-041506-8.
79. Andriani, R., A. Coghe, and G.E. Cossali, *Near-field entrainment in unsteady gas jets and diesel sprays: A comparative study.* Symposium (International) on Combustion, 1996. **26**(2): p. 2549-2556.
80. Kato, S.M., B.C. Groenewegen, and R.E. Breidenthal, *Turbulent mixing in nonsteady jets.* AIAA Journal, 1987. **25**(1): p. 165-168.
81. Shahsavan, M., M. Morovatiyan, and J.H. Mack, *A numerical investigation of hydrogen injection into noble gas working fluids.* International Journal of Hydrogen Energy, 2018. **43**(29): p. 13575-13582.
82. Ridley, J.D. and R.M. Clemilnts, *An Ignition System for Ultra Lean Mixtures AU - PITT, P. L.* Combustion Science and Technology, 1983. **35**(5-6): p. 277-285.
83. Perera, I., S. Wijeyakulasuriya, and R. Nalim, *Hot Combustion Torch Jet Ignition Delay Time for Ethylene-Air Mixtures*, in *49th AIAA Aerospace Sciences Meeting including the New Horizons Forum and Aerospace Exposition*. 2011, American Institute of Aeronautics and Astronautics.
84. Biswas, S., et al., *On ignition mechanisms of premixed CH4/air and H2/air using a hot turbulent jet generated by pre-chamber combustion.* Applied Thermal Engineering, 2016. **106**: p. 925-937.
85. Fischer, S., D. Markus, and U. Maas, *Numerical investigation of the ignition of diethyl ether/air and propane/air mixtures by hot jets.* Journal of Loss Prevention in the Process Industries, 2017. **49**: p. 832-838.
86. Wang, N., et al., *A numerical study of the combustion and jet characteristics of a hydrogen fueled turbulent hot-jet ignition (THJI) chamber.* International Journal of Hydrogen Energy, 2018. **43**(45): p. 21102-21113.
87. Witze, P.O.W., *Impulsively started incompressible turbulent jet.* Sandia Labs, 1980. **No. SAND-80-8617**.
88. Musculus, M.P.B., *Entrainment waves in decelerating transient turbulent jets.* Journal of Fluid Mechanics, 2009. **638**: p. 117-140.
89. Su, L.K. and N.T. Clemens, *The structure of fine-scale scalar mixing in gas-phase planar turbulent jets.* Journal of Fluid Mechanics, 2003. **488**: p. 1-29.

90. Sutton, J.A. and J.F. Driscoll, *Measurements and statistics of mixture fraction and scalar dissipation rates in turbulent non-premixed jet flames.* Combustion and Flame, 2013. **160**(9): p. 1767-1778.
91. Dunstan, T.D., et al., *Scalar dissipation rate modelling for Large Eddy Simulation of turbulent premixed flames.* Proceedings of the Combustion Institute, 2013. **34**(1): p. 1193-1201.
92. Ma, T., et al., *Validation and implementation of algebraic LES modelling of scalar dissipation rate for reaction rate closure in turbulent premixed combustion.* Combustion and Flame, 2014. **161**(12): p. 3134-3153.
93. Xu, G., et al., *Experimental and numerical investigations of the unscavenged prechamber combustion in a rapid compression and expansion machine under engine-like conditions.* Combustion and Flame, 2019. **204**: p. 68-84.
94. Zhang, Y., et al., *Experimental and modeling study on auto-ignition characteristics of methane/hydrogen blends under engine relevant pressure.* International Journal of Hydrogen Energy, 2012. **37**(24): p. 19168-19176.
95. M. E. Feyz, M.R.N., J. P. Gore, V. R. Hasti, *Modeling and analytical solution of the near-field entrainment in suddenly-started turbulent jets.* AIAA Journal, 2019(In Press).
96. Kilchyk, V., R. Nalim, and C. Merkle, *Laminar premixed flame fuel consumption rate modulation by shocks and expansion waves.* Combustion and Flame, 2011. **158**(6): p. 1140-1148.
97. Haiou Wang, E.R.H., Jacqueline H. Chen, *Turbulence-flame interactions in DNS of a laboratory high Karlovitz premixed turbulent jet flame.* Physics of Fluids, 2016. **28**(9): p. 095107.
98. Bouheraoua, L., P. Domingo, and G. Ribert, *Large-eddy simulation of a supersonic lifted jet flame: Analysis of the turbulent flame base.* Combustion and Flame, 2017. **179**: p. 199-218.
99. Duwig, C., et al., *Large Eddy Simulations of a piloted lean premix jet flame using finite-rate chemistry.* Combustion Theory and Modelling, 2011. **15**(4): p. 537-568.
100. Hafiz, N.M., M.R.A. Mansor, and W.M.F. Wan Mahmood, *Simulation of the combustion process for a CI hydrogen engine in an argon-oxygen atmosphere.* International Journal of Hydrogen Energy, 2018. **43**(24): p. 11286-11297.
101. Jain, S.K. and S.K. Aggarwal, *Compositional effects on the ignition and combustion of low octane fuels under diesel conditions.* Fuel, 2018. **220**: p. 654-670.
102. Selle, L., et al., *Compressible large eddy simulation of turbulent combustion in complex geometry on unstructured meshes.* Combustion and Flame, 2004. **137**(4): p. 489-505.
103. Peña Fernández, J.J. and J. Sesterhenn, *Compressible starting jet: pinch-off and vortex ring–trailing jet interaction.* Journal of Fluid Mechanics, 2017. **817**: p. 560-589.
104. Osborne, J.R., et al., *Relationship between local reaction rate and flame structure in turbulent premixed flames from simultaneous 10 kHz TPIV, OH PLIF, and CH2O PLIF.* Proceedings of the Combustion Institute, 2017. **36**(2): p. 1835-1841.
105. Law, C.K. and H.K. Law, *A Theoretical Study of Ignition in the Laminar Mixing Layer.* Journal of Heat Transfer, 1982. **104**(2): p. 329-337.
106. Wang, Z. and X. Gou, *Cool flame characteristics of methane/oxygen mixtures.* Journal of the Energy Institute, 2018.
107. Hajilou, M. and E. Belmont, *Characterization of ozone-enhanced propane cool flames at sub-atmospheric pressures.* Combustion and Flame, 2018. **196**: p. 416-423.

108. L.M. Pickett, G.B., Engine Combustion Network,(http://www.sandia.gov/ECN). 2011.
109. Pei, Y., Som, Sibendu, Pomraning, Eric, Senecal, Peter K., Skeen, Scott A., Manin, Julien, Pickett, Lyle M., *Large eddy simulation of a reacting spray flame with multiple realizations under compression ignition engine conditions.* Combustion and Flame, 2015. **162**(12): p. 4442-4455.
110. Ma, P.C., et al., *Large-eddy simulations of transcritical injection and auto-ignition using diffuse-interface method and finite-rate chemistry.* Proceedings of the Combustion Institute, 2019. **37**(3): p. 3303-3310.
111. Pawlak, G., et al., *Experimental characterization of starting jet dynamics.* Fluid Dynamics Research, 2007. **39**(11-12): p. 711-730.
112. Brookshear, D.W., J.A. Pihl, and J.P. Szybist, *Catalytic Steam and Partial Oxidation Reforming of Liquid Fuels for Application in Improving the Efficiency of Internal Combustion Engines.* Energy & Fuels, 2018. **32**(2): p. 2267-2281.
113. List, E.J., *Turbulent Jets and Plumes.* Annual Review of Fluid Mechanics, 1982. **14**(1): p. 189-212.
114. Gore, J.P., et al., *Structure and radiation properties of large□scale natural gas/air diffusion flames*, in *Fire and Materials*. 1986. p. 161-169.
115. Kleinstein, G., *Mixing in turbulent axially symmetric free jets.* Journal of Spacecraft and Rockets, 1964. **1**(4): p. 403-408.
116. Hill, P.G. and P. Ouellette, *Transient Turbulent Gaseous Fuel Jets for Diesel Engines.* Journal of Fluids Engineering, 1999. **121**(1): p. 93-101.
117. Joshi, A. and W. Schreiber, *An experimental examination of an impulsively started incompressible turbulent jet.* Experiments in Fluids, 2006. **40**(1): p. 156-160.
118. Hill, B.J., *Measurement of local entrainment rate in the initial region of axisymmetric turbulent air jets.* Journal of Fluid Mechanics, 1972. **51**(4): p. 773-779.
119. Abraham, J., *ENTRAPMENT CHARACTERISTICS OF TRANSIENT GAS JETS.* Numerical Heat Transfer, Part A: Applications, 1996. **30**(4): p. 347-364.
120. Breidenthal, R., *The turbulent exponential jet.* The Physics of Fluids, 1986. **29**(8): p. 2346-2347.
121. Turner, J.S., *The 'starting plume' in neutral surroundings.* Journal of Fluid Mechanics, 1968. **13**(3): p. 356-368.
122. Chitsaz, I., M.H. Saidi, and A.A. Mozafari, *Semi Analytical Solution to Transient Start of Weakly Underexpanded Turbulent Jet.* Journal of Fluids Engineering, 2011. **133**(9): p. 091204-091204-8.
123. Schlichting, H., *Boundary-layer theory*. 1968.
124. Kojok, A.T., *Hot Jet Ignition Delay Characterization of Methane and Hydrogen at Elevated Temperatures*. 2017, Purdue University.
125. Voorheis, T.S., and E. D. Howe, *The entrainment of air by a cylindrical jet.* Proceedings of the Pacific Coast Gas Associa tion, 1939(30): p. 198-201.
126. Polomiek. , E. 1948 University of Illinois.
127. Shin, D.-h., R.D. Sandberg, and E.S. Richardson, *Self-similarity of fluid residence time statistics in a turbulent round jet.* Journal of Fluid Mechanics, 2017. **823**: p. 1-25.
128. Obot, N.T., M.L. Graska, and T.A. Trabold, *The near field behavior of round jets at moderate reynolds numbers.* The Canadian Journal of Chemical Engineering, 1984. **62**(5): p. 587-593.

129. Bogey, C. and C. Bailly, *Turbulence and energy budget in a self-preserving round jet: direct evaluation using large eddy simulation.* Journal of Fluid Mechanics, 2009. **627**: p. 129-160.
130. Senecal, P.K., et al., *A New Parallel Cut-Cell Cartesian CFD Code for Rapid Grid Generation Applied to In-Cylinder Diesel Engine Simulations*. 2007, SAE International.
131. Hussein, H.J., S.P. Capp, and W.K. George, *Velocity measurements in a high-Reynolds-number, momentum-conserving, axisymmetric, turbulent jet.* Journal of Fluid Mechanics, 1994. **258**: p. 31-75.
132. Bremhorst, K. and P.G. Hollis, *Velocity field of an axisymmetric pulsed, subsonic air jet.* AIAA Journal, 1990. **28**(12): p. 2043-2049.
133. Maxworthy, T., *The structure and stability of vortex rings.* Journal of Fluid Mechanics, 1972. **51**(1): p. 15-32.
134. Pawlak, G., et al., *Experimental characterization of starting jet dynamics.* Fluid Dynamics Research, 2007. **39**(11): p. 711-730.
135. Astbury, G.R. and S.J. Hawksworth, *Spontaneous ignition of hydrogen leaks: A review of postulated mechanisms.* International Journal of Hydrogen Energy, 2007. **32**(13): p. 2178-2185.
136. Germane, G.J., C.G. Wood, and C.C. Hess, *Lean Combustion in Spark-Ignited Internal Combustion Engines - A Review*. 1983, SAE International.
137. !!! INVALID CITATION !!! [9, 10].
138. Rogers, M.M. and R.D. Moser, *The three-dimensional evolution of a plane mixing layer: the Kelvin–Helmholtz rollup.* Journal of Fluid Mechanics, 1992. **243**: p. 183-226.
139. Kessler, A., et al., *Ignition of hydrogen jet fires from high pressure storage.* International Journal of Hydrogen Energy, 2014. **39**(35): p. 20554-20559.
140. Qing-he, L., et al., *The effect of equivalence ratio, temperature and pressure on the combustion characteristics of hydrogen-air pre-mixture with turbulent jet induced by pre-chamber sparkplug.* International Journal of Hydrogen Energy, 2019. **44**(36): p. 20470-20481.
141. Wang, N., et al., *Ignition kinetics of a homogeneous hydrogen/air mixture using a transient hot jet.* International Journal of Hydrogen Energy, 2018. **43**(33): p. 16373-16385.
142. Biswas, S. and L. Qiao, *Ignition of ultra-lean premixed hydrogen/air by an impinging hot jet.* Applied Energy, 2018. **228**: p. 954-964.
143. Liñán Martínez, A., Crespo Martínez, Antonio, *An asymptotic analysis of undesteady diffusion flames for large activation energies*. 1972: Madrid.
144. Jiji, L.M., *Heat Conduction*, ed. T. Edition. 2009: Springer.
145. Ozisik, M.N., *Heat Conduction- Chapter 3*. 2 ed. 1993: John Wiley & Sons.
146. White, D.R. and G.E. Moore, *Structure of gaseous detonation. IV. Induction zone studies in H2-O2 and CO-O2 mixtures.* Symposium (International) on Combustion, 1965. **10**(1): p. 785-795.
147. Cheng, R.K. and A.K. Oppenheim, *Autoignition in methane □ hydrogen mixtures.* Combustion and Flame, 1984. **58**(2): p. 125-139.
148. Marshall, B.W., Jr., *Hydrogen:air:steam flammability limits and combustion characteristics in the FITS [Fully Instrumented Test Site] vessel*. 1986: United States. p. 146.

149. Mukhopadhyay, S. and J. Abraham, *Evaluation of an unsteady flamelet progress variable model for autoignition and flame development in compositionally stratified mixtures.* 2012. **24**(7): p. 075115.
150. Karaca, M., et al., *Implicit large eddy simulation of vitiation effects in supersonic air/H2 combustion.* Aerospace Science and Technology, 2019. **89**: p. 89-99.
151. Bartolucci, L., et al., *Natural Gas Partially Stratified Lean Combustion: Analysis of the Enhancing Mechanisms into a Constant Volume Combustion Chamber.* Fuel, 2018. **211**: p. 737-753.
152. Ó Conaire, M., et al., *A comprehensive modeling study of hydrogen oxidation.* 2004. **36**(11): p. 603-622.
153. Forney, L.J. and N. Nafia, *Turbulent Jet Reactors: Mixing Time Scales.* Chemical Engineering Research and Design, 1998. **76**(6): p. 728-736.
154. Bulat, G., et al., *Reacting flow in an industrial gas turbine combustor: LES and experimental analysis.* Proceedings of the Combustion Institute, 2015. **35**(3): p. 3175-3183.
155. Berglund, M., et al., *Finite Rate Chemistry Large-Eddy Simulation of Self-Ignition in Supersonic Combustion Ramjet.* 2010. **48**(3): p. 540-550.
156. Sabelnikov, V. and C. Fureby, *LES combustion modeling for high Re flames using a multi-phase analogy.* Combustion and Flame, 2013. **160**(1): p. 83-96.
157. Yamashita, H., M. Shimada, and T. Takeno, *A numerical study on flame stability at the transition point of jet diffusion flames.* Symposium (International) on Combustion, 1996. **26**(1): p. 27-34.
158. Aung, K.T., M.I. Hassan, and G.M. Faeth, *Flame stretch interactions of laminar premixed hydrogen/air flames at normal temperature and pressure.* Combustion and Flame, 1997. **109**(1): p. 1-24.
159. Dabiri, J.O. and M. Gharib, *Fluid entrainment by isolated vortex rings.* Journal of Fluid Mechanics, 2004. **511**: p. 311-331.
160. Gharib, M., E. Rambod, and K. Shariff, *A universal time scale for vortex ring formation.* Journal of Fluid Mechanics, 1998. **360**: p. 121-140.
161. Syed, A.u.H. and H.J. Sung, *Effect of an Exit-Wedge Angle on Pinch-off and Mass Entrainment of Vortex Rings in Air.* Flow, Turbulence and Combustion, 2008. **82**(3): p. 391.
162. Sau, R. and K. Mahesh, *Passive scalar mixing in vortex rings.* Journal of Fluid Mechanics, 2007. **582**: p. 449-461.
163. Wijeyakulasuriya, S.D., *Transient and translating gas jet modeling for pressure gain combustion applications*. 2011, Purdue University.
164. Karimi, A., M. Rajagopal, and R. Nalim, *Traversing Hot-Jet Ignition in a Constant-Volume Combustor.* Journal of Engineering for Gas Turbines and Power, 2013. **136**(4).
165. Wijeyakulasuriya, S.D., M. Rajagopal, and R. Nalim. *Shock-Flame Interaction Modeling in a Constant-Volume Combustion Channel Using Detailed Chemical Kinetics and Automatic Mesh Refinement*. in *ASME Turbo Expo 2013: Turbine Technical Conference and Exposition*. 2013.